SLAC-R-639
UMI-96-11987-mc
RX-1557

A Determination of the Neutron Spin Structure Function

David Michael Kawall

Stanford Linear Accelerator Center, Stanford University, Stanford, CA 94309

Work supported by Department of Energy contract DE–AC03–76SF00515.

A DETERMINATION OF THE NEUTRON SPIN STRUCTURE FUNCTION

A DISSERTATION
SUBMITTED TO THE DEPARTMENT OF PHYSICS
AND THE COMMITTEE ON GRADUATE STUDIES
OF STANFORD UNIVERSITY
IN PARTIAL FULFILLMENT OF THE REQUIREMENTS
FOR THE DEGREE OF
DOCTOR OF PHILOSOPHY

David Michael Kawall
September 1995

Abstract

We report the results of the experiment E142 which measured the spin dependent structure function of the neutron, $g_1^n(x, Q^2)$. The experiment was carried out at the Stanford Linear Accelerator Center by measuring an asymmetry in the deep inelastic scattering of polarized electrons from a polarized ^{3}He target, at electron energies from 19 to 26 GeV. The structure function was determined over the kinematic range 0.03 $<$ Bjorken x $<$ 0.6 and 1.0 $< Q^2 <$ 5.5 (GeV/c)^2. An evaluation of the integral $\int_0^1 g_1^n(x, Q^2)dx$ at fixed Q^2 = 2 (GeV/c)^2 yields our final result Γ_1^n = -0.032 ± 0.006 (stat.) $\pm$ 0.009 (syst.). This result, when combined with the integral of the proton spin structure function measured in other experiments, confirms the fundamental Bjorken sum rule with $O(\alpha_s^3)$ corrections to within one standard deviation. This is a major success for perturbative Quantum Chromodynamics.

Some ancillary results include our findings that the Ellis-Jaffe sum rule for the neutron is violated at the 2 σ level, and that the total contribution of the quarks to the helicity of the nucleon is 0.36 ± 0.10. The strange sea polarization is estimated to be small and negative, $\Delta s = -0.07 \pm 0.04$.

Acknowledgements

A project such as this one involves many people, directly and indirectly. To those with whom I've worked over these last years, I'd like to extend my sincerest gratitude for making this such a tremendous experience. The work described in these pages was made worthwhile in particular by the companionship of Makis, Roger, Yves, Michael, Jim, Hunter and James. Charlie is unforgettable and I will certainly miss his playing devil's advocate. It has been a privilege to work with Emlyn, whom I see as an example to aspire towards, and I certainly owe him a debt of thanks for taking the initiative and starting this whole adventure.

I'd like to acknowledge here my respect and thanks to Zein-Eddine for the time and support he has given me. I doubt a student could ever have a finer physicist as a mentor.

The time spent on E142 was time away from old friends and family. To Doug, Will, John and Les I'd like to apologize for being so consumed, and thank you for sticking with me through the years.

Of course, the time spend away from my brothers Nige and Jay was missed deeply, and even more so the time away from my dear mother and father, to whom this time and work is dedicated.

Contents

List of Tables

List of Figures

Chapter 1

Theoretical Introduction

1.1 Introduction

The work represented in this thesis is one of the first attempts to determine experimentally the spin structure function, g_1^n, of the neutron. The basis of the measurement is the scattering of longitudinally polarized high energy electrons from a longitudinally polarized ^{3}He target (which we may consider as a model for a polarized neutron). By measuring a difference in the scattering cross sections between the cases in which the beam and target spins are parallel and antiparallel, we reveal information about the underlying spin distributions of the quarks and gluons composing a neutron. This information is intrinsically interesting, and plays an important role in tests of our understanding of the theory of Quantum Chromodynamics (QCD).

This work was carried out by the E142 collaboration at the Stanford Linear Accelerator Center (SLAC).

1.2 Spin Dependent Deep Inelastic Scattering

The electromagnetic interaction of a charged lepton with a nucleon is described at lowest order the single virtual photon exchange Feynman diagram in Figure 1.1. In inclusive scattering experiments, like the one described in these pages, the final hadronic states are not detected, and the process is written as $l + N \rightarrow l + X$. The kinematic variables and Lorentz invariants used to describe the scattering of an

Variable	Description	Value in Lab Frame
s	Incident lepton spin four-vector	$\frac{1}{m}(\|\vec{k}\|, 0, 0, E)$
S	Target nucleon spin four-vector	$(0, \vec{S})$
k	Incident lepton four-momentum	$(E, \vec{k})$
k'	Scattered lepton four-momentum	$(E', \vec{k'})$
P	Target nucleon four-momentum	$(M, \vec{0})$
q	Virtual photon four-momentum transfer	$q = k - k' = (\nu, \vec{q})$
θ	Scattering angle of lepton	
Invariants	Description	Value in Lab Frame
$Q^2 = -q^2$	Four momentum transfer squared	$\approx 4EE'\sin^2(\theta/2)$
ν	Energy of virtual photon	$P \cdot q/M = E - E'$
x	Bjorken scaling variable	$-q \cdot q/2P \cdot q = Q^2/2M\nu$
W^2	Invariant mass of final hadronic state	$(P+q)^2 = M^2 + 2M\nu - Q^2$

Table 1.1: Kinematic variables and invariants in lepton-nucleon scattering.

incident lepton of mass m and energy E from a target nucleon of mass M are shown in Table 1.1. [1] With these definitions, we can write the double differential cross section for the process in Figure 1.1 as

$$\frac{d^2\sigma}{d\Omega dE'} = \frac{4\alpha^2}{Q^4}\frac{E'}{E}L_{\mu\nu}W^{\mu\nu} \tag{1.1}$$

where α is the fine structure constant[2] and the tensors $L_{\mu\nu}$ and $W^{\mu\nu}$ describe the leptonic and hadronic currents respectively. Experimentally this is measured by detecting the leptons of energy E' at an angle θ scattered from a nuclear target. The leptonic tensor can be calculated from the Feynman rules, and summed over final spins s', takes the form :

$$\begin{aligned} L_{\mu\nu} &= \sum_{s'} \bar{u}(k', s')\gamma_\mu u(k, s)\bar{u}(k, s)\gamma_\nu u(k', s') \\ &= \frac{1}{2}Tr[(\not{k} + m)\gamma_\mu(\not{k} + m)\tfrac{1}{2}(1 + \gamma_5 \not{s})\gamma_\nu] \end{aligned}$$

[1] The odd form of s is a consequence of the requirement that $s^2 = -1$ and $s \cdot k = 0$.

[2] The running of α is accounted for by performing radiative corrections to experimental cross sections.

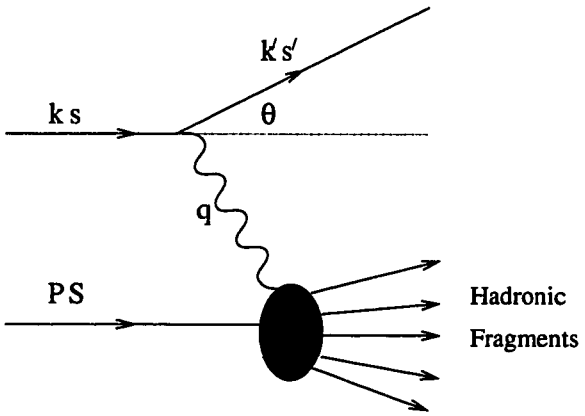

Figure 1.1: Feynman diagram for charged lepton-nucleon scattering in the approximation of a single virtual photon exchange.

$$\begin{aligned} &= k'_\mu k_\nu + k'_\nu k_\mu - g_{\mu\nu} k' \cdot k + im\epsilon_{\mu\nu\alpha\beta} s^\alpha q^\beta \\ &\equiv L^S_{\mu\nu} + iL^A_{\mu\nu} \end{aligned} \tag{1.2}$$

where g is the metric tensor and ϵ is the antisymmetric Levi-Civita tensor. Three observations should be made at this point. First, the tensor has a part, $L^S_{\mu\nu}$, symmetric under $\mu \leftrightarrow \nu$, and an antisymmetric part, $L^A_{\mu\nu}$, where only the latter part contains the spin of the lepton. Second, the antisymmetric part, $L^A_{\mu\nu} = m\epsilon_{\mu\nu\alpha\beta} s^\alpha q^\beta$ is not proportional to the lepton mass since $s^\alpha \propto 1/m$. Finally, the leptonic tensor is completely determined so the upper vertex in Figure 1.1 can be considered as understood. It is the lower, hadronic vertex which contains the unknown hadronic structure we wish to investigate. In NN scattering the upper vertex would also be complicated by nuclear structure, explaining the continuing appeal of lepton scattering for investigating nucleon structure.

The hadronic tensor we wish to investigate can be written in terms of the commutator of the hadronic electromagnetic current, j^{em}_μ, where we will drop the *em* henceforth. Similar to the lepton current, it is decomposed into a spin dependent and spin independent part [1, 4]:

$$\begin{aligned} W^{\mu\nu} &= \frac{1}{2\pi} \int d^4x e^{iq\cdot x} \langle P,S|[j_m u(x), j_\nu(0)]|P,S\rangle \\ &= W^{\mu\nu}_S + iW^{\mu\nu}_A \end{aligned} \tag{1.3}$$

The symmetric part has the decomposition in terms of two spin independent structure functions $W_1(\nu, Q^2)$ and $W_2(\nu, Q^2)$:

$$W_S^{\mu\nu} = -\Big(g^{\mu\nu} - \frac{q^\mu q^\nu}{q^2}\Big)W_1 + \frac{1}{M^2}\Big(P^\mu - \frac{P\cdot q}{q^2}q^\mu\Big)\Big(P^\nu - \frac{P\cdot q}{q^2}q^\nu\Big)W_2. \qquad (1.4)$$

Similarly, the antisymmetric part is written in terms of two spin dependent structure functions, $G_1(\nu, Q^2)$ and $G_2(\nu, Q^2)$ [2, 4]:

$$W_A^{\mu\nu} = M\epsilon^{\mu\nu\alpha\beta}q_\alpha s_\beta G_1(\nu, Q^2) + \frac{1}{M}\epsilon^{\mu\nu\alpha\beta}q_\alpha[(P\cdot q)S_\beta - (S\cdot q)P_\beta]G_2(\nu, Q^2). \qquad (1.5)$$

This term changes sign when the nucleon spin is reversed. Such a decomposition of the hadronic tensor into four unknown structure functions is possible because the form of the tensor is constrained to be invariant under parity and time reversal, as well as being hermitian; $W^{\mu\nu} = W^{\nu\mu *}$, and it must satisfy the current conservation constraint $q_\mu W^{\mu\nu} = q_\nu W^{\mu\nu} = 0$ [3].

In order to investigate the spin dependent structure functions, G_1 and G_2, it is necessary to use both a polarized beam and a polarized target since $L_{\mu\nu}^A W_S^{\mu\nu} = L_{\mu\nu}^S W_A^{\mu\nu} = 0$, and only the combinations $L_{\mu\nu}^S W_S^{\mu\nu}$, and $L_{\mu\nu}^A W_A^{\mu\nu}$ are nonvanishing.

We will now restrict ourselves to the case in which the lepton is polarized along its direction of motion and the nucleon spin lies in the plane defined by the incident and scattered lepton three-momentum vectors. Under these restrictions, we examine the difference in cross sections when a positive helicity lepton scatters from a nucleon polarized at an angle $\phi + \pi$ with respect to the incident lepton momentum compared to the cross section when the nucleon spin is at an angle ϕ. Summing over final lepton spin states and over all hadronic final states yields [4]

$$\frac{d^2\sigma^{\uparrow\phi+\pi}}{d\Omega dE'} - \frac{d^2\sigma^{\uparrow\phi}}{d\Omega dE'} = \frac{4\alpha^2}{Q^2}\frac{E'}{E}\Big[(E\cos\phi + E'\cos(\theta-\phi))MG_1 - 2EE'(\cos\phi - \cos(\theta-\phi))G_2\Big] \qquad (1.6)$$

where the $\uparrow$ symbolizes the positive helicity of the lepton. For the specific case where $\phi = 0$ in which the target is polarized along the beam direction, we find :

$$\frac{d^2\sigma^{\uparrow\Downarrow}}{d\Omega dE'} - \frac{d^2\sigma^{\uparrow\Uparrow}}{d\Omega dE'} = \frac{4\alpha^2}{Q^2}\frac{E'}{E}\Big[(E + E'\cos\theta)MG_1 - Q^2G_2\Big] \qquad (1.7)$$

where we have used $\Uparrow$ ($\Downarrow$) to indicate that the target spin is parallel(antiparallel) to the beam direction. We can also recover the unpolarized cross section via :

$$\frac{1}{2}\Big(\frac{d^2\sigma^{\uparrow\Downarrow}}{d\Omega dE'} + \frac{d^2\sigma^{\uparrow\Uparrow}}{d\Omega dE'}\Big) = \frac{4\alpha^2}{Q^4}E'^2\Big[2W_1\sin^2\tfrac{1}{2}\theta + W_2\cos^2\tfrac{1}{2}\theta\Big]. \qquad (1.8)$$

Another interesting case is the difference in cross sections when the target is polarized transversely at $\phi = \pi/2$ in equation (1.6)

$$\frac{d^2\sigma^{\uparrow\Leftarrow}}{d\Omega dE'} - \frac{d^2\sigma^{\uparrow\Rightarrow}}{d\Omega dE'} = \frac{4\alpha^2}{Q^2}\frac{E'^2}{E}\sin\theta[MG_1 + 2EG_2]. \tag{1.9}$$

We can gain some insight into the physical meaning of these cross sections by considering their relation to the cross sections for forward virtual Compton scattering, $\gamma^* + N \rightarrow \gamma^* + N$ [5, 6]. The absorptive part of the forward cross section is related by the optical theorem to the total photoabsorption cross section, which has the form :

$$\sigma_{\pm 1,0} = \frac{4\pi^2\alpha}{K}\epsilon^{\mu *}_{\pm 1,0} W_{\mu\nu}\epsilon^{\nu}_{\pm 1,0} \tag{1.10}$$

where K is the flux for virtual photons (which the Hand convention specifies as K=$\nu - Q^2/2M$). The ϵ are the polarization vectors of the virtual photons :

$$\epsilon_{\pm 1} = \frac{1}{\sqrt{2}}(0, 1, \pm i, 0) \tag{1.11}$$

$$\epsilon_0 = \frac{1}{\sqrt{Q^2}}(\sqrt{Q^2 + \nu^2}, 0, 0, \nu) \tag{1.12}$$

where the $\epsilon_{\pm 1}$ denotes transversely polarized photons, and ϵ_0 is for scalar photons. These can be combined with equations (1.4) and (1.5) in (1.10) to get expressions for the cross sections as follows. Denoting by $T_{[\alpha\beta\rightarrow\mu\nu]}$ the forward virtual Compton amplitude for scattering a photon with spin projection (along the direction of the photon) α from a nucleon with spin projection β, yielding final spin projections $\mu\nu$, we can then write all of the possible transitions [6, 7]:

$$\begin{aligned}
\text{Im } T_{[1\frac{1}{2}\rightarrow 1\frac{1}{2}]} \propto \sigma_{3/2} &= \frac{4\pi^2\alpha}{K}[W_1 + M\nu G_1 - Q^2 G_2] \\
\text{Im } T_{[1-\frac{1}{2}\rightarrow 1-\frac{1}{2}]} \propto \sigma_{1/2} &= \frac{4\pi^2\alpha}{K}[W_1 - M\nu G_1 + Q^2 G_2] \\
\text{Im } T_{[0\frac{1}{2}\rightarrow 0\frac{1}{2}]} \propto \sigma_L &= \frac{4\pi^2\alpha}{K}[W_2(1 + \nu^2/Q^2) - W_1] \\
\text{Im } T_{[0-\frac{1}{2}\rightarrow 1\frac{1}{2}]} \propto \sigma_{TL} &= \frac{4\pi^2\alpha}{K}\sqrt{Q^2}[MG_1 + \nu G_2]
\end{aligned} \tag{1.13}$$

where we have written $\sigma_{3/2}$ ($\sigma_{1/2}$) for the total cross section when the total spin projection along the virtual photon direction is 3/2 (1/2). The cross section for longitudinal

(scalar) photons is written σ_L, σ_{TL} is an helicity flip interference amplitude, and we define $\sigma_T = \frac{1}{2}(\sigma_{1/2} + \sigma_{3/2})$. Time reversal invariance relates $T_{[0-\frac{1}{2}\to 1\frac{1}{2}]}$ to $T_{[1\frac{1}{2}\to 0-\frac{1}{2}]}$, so we see that only four amplitudes are needed to describe polarized photon-nucleon scattering and hence four structure functions are required, W_1, W_2, G_1, and G_2 [6]. It is useful at this point to define the ratio of longitudinal to transverse cross sections :

$$R = \frac{\sigma_L}{\sigma_T} = \frac{W_2}{W_1}\left(1 + \frac{\nu}{2Mx}\right) - 1. \tag{1.14}$$

Now consider the virtual *photon*-nucleon asymmetries

$$A_1 = \frac{\sigma_{1/2} - \sigma_{3/2}}{\sigma_{1/2} + \sigma_{3/2}} = \frac{M\nu G_1 - Q^2 G_2}{W_1} \tag{1.15}$$

and

$$A_2 = \frac{\sigma_{TL}}{\sigma_T} = \sqrt{Q^2}\frac{[MG_1 + \nu G_2]}{W_1}. \tag{1.16}$$

These asymmetries satisfy the bounds $|A_1| \leq 1$ and $|A_2| \leq \sqrt{R}$ [8], and can be related to the *lepton*-nucleon asymmetries formed from equations (1.7), (1.8) and (1.9) by:

$$A_{\parallel} \equiv \frac{\sigma^{\uparrow\Downarrow} - \sigma^{\uparrow\Uparrow}}{\sigma^{\uparrow\Downarrow} + \sigma^{\uparrow\Uparrow}} \tag{1.17}$$

and

$$A_{\perp} \equiv \frac{\sigma^{\uparrow\Leftarrow} - \sigma^{\uparrow\Rightarrow}}{\sigma^{\uparrow\Leftarrow} + \sigma^{\uparrow\Rightarrow}} \tag{1.18}$$

through the relations

$$A_{\parallel} = D(A_1 + \eta A_2). \tag{1.19}$$

and

$$A_{\perp} = d(A_2 + \zeta A_1). \tag{1.20}$$

Here we have defined the factors

$$\begin{aligned} D &= \frac{1 - \frac{E'}{E}\epsilon}{1 + \epsilon R}, \\ d &= D\sqrt{\frac{2\epsilon}{1+\epsilon}}, \\ \eta &= \frac{\epsilon\sqrt{Q^2}}{E - E'\epsilon}, \text{ and} \\ \zeta &= \eta\left(\frac{1+\epsilon}{2\epsilon}\right) \end{aligned} \tag{1.21}$$

where

$$\epsilon = \left[1 + 2\left(1 + \nu^2/Q^2\right)\tan^2\left(\tfrac{1}{2}\theta\right)\right]^{-1} \tag{1.22}$$

is the ratio of longitudinal to transverse photon fluxes. The factors η and ζ are small, so that $A_{\parallel} \simeq DA_1$ and $A_{\perp} \simeq dA_2$. The factor D, which is < 1, has the interpretation of being the depolarization of the virtual photon, making the lepton-nucleon asymmetry, $A_{\parallel}$, less than the pure photon-nucleon asymmetry, A_1. One source of this effect is that the virtual photon interacts at an angle with respect to the spin of the nucleon, so the projection of its spin is diluted. Also, the virtual photon may be longitudinally polarized instead of transversely polarized, so its scattering will be insensitive to the spin of the nucleon and will dilute the measured lepton-nucleon asymmetry.

In experiments we measure the lepton-nucleon asymmetries, $A_{\parallel}$ and $A_{\perp}$, of equations (1.17) and (1.18), but it is the photon-nucleon asymmetries A_1 and A_2 (1.15) and (1.16) which are of physical significance. This is clear since the lepton-nucleon asymmetries measured depend directly on quantities such as spectrometer angle and beam energy. In contrast, we note that the virtual photon asymmetries are expressed in terms of invariants and structure functions, and thus are likely to yield a physical interpretation. In preparation for the analysis of the experiment, we write the photon asymmetries in terms of the lepton asymmetries actually measured. These equations will be drawn upon heavily in the analysis.

$$A_1 = \frac{A_{\parallel}}{D(1+\zeta\eta)} - \frac{\eta A_{\perp}}{d(1+\zeta\eta)} \tag{1.23}$$

$$A_2 = \frac{\zeta A_{\parallel}}{D(1+\zeta\eta)} + \frac{A_{\perp}}{d(1+\zeta\eta)} \tag{1.24}$$

1.3 Quark Parton Model

In the quark parton model of Bjorken, Feynman and Paschos [9, 10, 11] a nucleon of momentum P is considered to be composed of point-like constituents (partons), each carrying a fraction of momenta ξ_i of the total nucleon momentum, where $\sum \xi_i = 1$ and $0 \leq \xi \leq 1$ [12]. When viewed in a frame in which P is large, the interactions of the constituents are time dilated, and at very high momentum appear not to interact at all. In this limit we can ignore the transverse motion of the constituents. Now

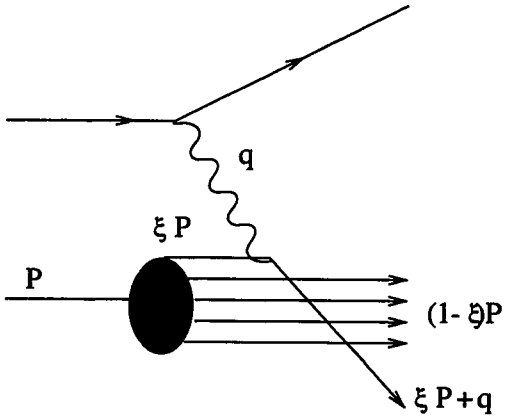

Figure 1.2: Deep inelastic scattering in the quark-parton model.

consider what happens when one of the partons with initial momentum ξP is struck by a virtual photon of four momentum q. For sufficiently large Q^2, during the short lifetime of the virtual photon $\sim 1/(Q^2)^{1/2}$ the partons appear to be quasi-free. The scattered parton has a large momentum compared to the other constituents and is also quasi-free. Then we can consider this deep inelastic scattering (DIS) as incoherent and elastic, so we can write

$$(\xi P + q)^2 = m^2 \tag{1.25}$$

where m is the mass of the parton. For large momentum transfer compared to the parton mass, we find

$$\xi = \frac{Q^2}{2M\nu} = x \tag{1.26}$$

so we associate the Bjorken scaling variable x with the fraction of the parent nucleon momentum carried by the parton before scattering The process is shown in Figure 1.2. In the parton model, the structure functions are predicted to scale, so that in the Bjorken limit, $Q^2 \to \infty$ and $\nu \to \infty$ with $x = Q^2/2M\nu$ constant, the structure functions were predicted to lose their dependence on Q^2 and become functions of x alone. This leads to the behavior [12]

$$\begin{aligned} MW_1(\nu, Q^2) &\to F_1(x) \\ \nu W_2(\nu, Q^2) &\to F_2(x) \\ M^2 \nu G_1(\nu, Q^2) &\to g_1(x) \end{aligned}$$

$$M\nu^2 G_2(\nu, Q^2) \to g_2(x). \tag{1.27}$$

In the scaling limit we can rewrite the structure functions as :

$$\begin{aligned} F_1 &= \frac{F_2\,(1+Q^2/\nu^2)}{2x\,[1+R]} \\ g_1 &= \frac{F_2}{2x\,[1+R]}\left[A_1 + \frac{\sqrt{Q^2}}{\nu}A_2\right] \\ g_2 &= \frac{F_2}{2x\,[1+R]}\left[A_2\frac{\nu}{\sqrt{Q^2}} - A_1\right]. \end{aligned} \tag{1.28}$$

If we consider deep inelastic scattering as the incoherent sum of elastic scattering from spin 1/2 constituents, we can interpret the structure functions as [12]

$$\begin{aligned} F_1(x) &= \tfrac{1}{2}\sum_i e_i^2[q_i^{\uparrow}(x) + q_i^{\downarrow}(x)] \\ F_2(x) &= x\sum_i e_i^2[q_i^{\uparrow}(x) + q_i^{\downarrow}(x)] \\ g_1(x) &= \tfrac{1}{2}\sum_i e_i^2[q_i^{\uparrow}(x) - q_i^{\downarrow}(x)] \\ g_1(x) + g_2(x) &= \frac{1}{2Mx}\sum_i e_i^2 m_i[q_i^{\uparrow T}(x) - q_i^{\downarrow T}(x)] \end{aligned} \tag{1.29}$$

where $q_i^{\uparrow}(x)$ ($q_i^{\downarrow}(x)$) is the probability of finding a quark or antiquark of flavor i with a fraction x of the total nucleon momentum with its spin parallel (antiparallel) to the spin of the parent nucleon. Transverse polarizations are indicated by T. Now we can rewrite the photon-nucleon asymmetries in the scaling limit :

$$\begin{aligned} \lim_{Bj} A_1 &\to \frac{2x(1+R)}{F_2(x)}g_1(x) \\ \lim_{Bj} A_2 &\to \frac{\sqrt{Q^2}}{1+\nu^2/Q^2}\frac{g_1(x)+g_2(x)}{2MxF_1(x)} \to 0 \end{aligned} \tag{1.30}$$

and

$$\lim_{Bj} R \to \frac{F_2(x)}{2xF_1(x)}(1+Q^2/\nu^2) - 1 \to \frac{F_2(x)}{2xF_1(x)} - 1 \to 0. \tag{1.31}$$

We can substitute this last equation into our expression for A_1, to yield

$$A_1(x) = \frac{\sum_i e_i^2[q_i^{\uparrow}(x) - q_i^{\downarrow}(x)]}{\sum_i e_i^2[q_i^{\uparrow}(x) + q_i^{\downarrow}(x)]} \tag{1.32}$$

$$\simeq \frac{g_1(x)}{F_1(x)} \tag{1.33}$$

This has the immediate interpretation as the sum of the polarizations of the quarks along the spin direction of the nucleon, weighted by their charge squared. Thus the photon-nucleon asymmetry, A_1, shows us how the spin is distributed within the nucleon.

As an example of what A_1 might look like, we consider the static SU(6) model of the proton composed of three constituent quarks [22]. The probabilities for finding an up quark with its spin parallel to the proton spin is 5/9, which we'll denote $u^{\uparrow} = 5/9$. Similarly, we can write

$$u^{\uparrow} = \frac{5}{9}, \quad u^{\downarrow} = \frac{1}{9}, \quad d^{\uparrow} = \frac{1}{9}, \quad d^{\downarrow} = \frac{2}{9}. \tag{1.34}$$

The spin for the neutron are related to those of the proton by isospin symmetry $u \leftrightarrow d$. Substituting these probabilities into (1.33) we find [22]

$$A_1^P = \frac{\frac{4}{9}(u^{\uparrow} - u^{\downarrow}) + \frac{1}{9}(d^{\uparrow} - d^{\downarrow})}{\frac{4}{9}(u^{\uparrow} + u^{\downarrow}) + \frac{1}{9}(d^{\uparrow} + d^{\downarrow})} = \frac{5}{9} \tag{1.35}$$

and for the neutron $A_1^n = 0$. Naively, we might expect these values to be observed at $x \sim 0.3$ where the struck quark behaves like it is 1/3 of a nucleon.

1.4 Sum Rules

1.4.1 Bjorken Sum Rule

One of the motivating factors to perform the experiment E142 was to test for the first time the Bjorken sum rule, derived in 1966 [13]. Based on current algebra, isospin symmetry and using the standard assignments for the quark charges, it is regarded as fundamental and on firm theoretical ground. This remarkable sum rule relates the difference of the integrals of the proton and neutron spin structure functions to the ratio of axial to vector couplings, g_A/g_V, observed in beta decay. This robust sum rule is an interesting coupling of seemingly disaparate high energy electromagnetic phenomena and low energy nuclear decay phenomena. In the Bjorken limit it is written

$$\int_0^1 [g_1^p(x) - g_1^n(x)]dx = \frac{1}{6}\left|\frac{g_A}{g_V}\right| = 0.210 \pm 0.002. \tag{1.36}$$

The sum rule has since been rederived[3] in the framework of the Operator Product Expansion [14] and perturbative QCD corrections have calculated to order α_s^3, so that the modern form of the sum rule for three quark flavors is [15]

$$\int_0^1 [g_1^p(x) - g_1^n(x)]dx = \frac{1}{6}\left|\frac{g_A}{g_V}\right|\left[1 - \frac{\alpha_s(Q^2)}{\pi} - 3.5833\left(\frac{\alpha(Q^2)}{\pi}\right)^2 - 20.2153\left(\frac{\alpha(Q^2)}{\pi}\right)^3 - O(130)\left(\frac{\alpha(Q^2)}{\pi}\right)^4\right]. \quad (1.37)$$

The corrections are critical for enabling the sum rule to be tested at the finite Q^2 accessible to experiments. The sum rule is not expected to fail.

1.4.2 Ellis-Jaffe Sum Rule

A less rigorous set of sum rules was derived for the proton and neutron separately, assuming an exact SU(3) symmetry in the baryon octet decays. Coupled with the further assumption that the polarization of the strange sea quarks is zero, yields the Ellis-Jaffe sum rules [17]

$$\int_0^1 g_1^p(x)dx = \frac{1}{12}\left|\frac{g_A}{g_V}\right|\left[+1 + \frac{5}{3}\frac{3F-D}{F+D}\right] \quad (1.38)$$

$$\int_0^1 g_1^n(x)dx = \frac{1}{12}\left|\frac{g_A}{g_V}\right|\left[-1 + \frac{5}{3}\frac{3F-D}{F+D}\right] \quad (1.39)$$

where F and D are the symmetric and antisymmetric constants describing the baryon octet decay, and have the values F=0.459 $\pm$ 0.008 and D=0.798 $\pm$ 0.008 [18]. The F and D constants can be expressed in terms of the quark spins :

$$\begin{aligned} \Delta u - \Delta d &= F + D \\ \Delta u + \Delta d - 2\Delta s &= 3F - D \\ \Delta u + \Delta d + \Delta s &\equiv \Delta\Sigma. \end{aligned} \quad (1.40)$$

Then we can rewrite the Ellis-Jaffe equations in terms of the individual quark contributiuons to the nucleon spin. Decomposing the spin structure function first moments into their individual quark contributions, we find :

$$\Gamma_1^n = \frac{1}{2}\left(\frac{1}{9}\Delta u + \frac{4}{9}\Delta d + \frac{1}{9}\Delta s\right)$$

[3] A derivation is presented in the Appendix

$$\begin{aligned}\Gamma_1^p &= \frac{1}{2}\left(\frac{4}{9}\Delta u + \frac{1}{9}\Delta d + \frac{1}{9}\Delta s\right) \\ \Gamma_1^d &= \frac{1}{2}\left(\frac{5}{18}\Delta u + \frac{5}{18}\Delta d + \frac{2}{18}\Delta s\right)\end{aligned} \tag{1.41}$$

where we have used the definitions :

$$\Gamma_1^N = \int_0^1 dx g_1^N(x, Q^2) \tag{1.42}$$

$$\Delta q = \int_0^1 dx \left[q_+(x) - q_-(x) + \bar{q}_+(x) - \bar{q}_-(x)\right]. \tag{1.43}$$

Further decomposing into singlet ($\Delta u + \Delta d + \Delta s$) and non-singlet components ($\Delta u - \Delta d$, $\Delta u + \Delta d - 2\Delta s$), and including perturbative QCD corrections yields :

$$\begin{aligned}\Gamma_1^n &= -\frac{1}{12}(\Delta u - \Delta d)C_{ns} + \frac{1}{36}(\Delta u + \Delta d - 2\Delta s)C_{ns} + \frac{1}{9}(\Delta u + \Delta d + \Delta s)C_s \\ \Gamma_1^p &= +\frac{1}{12}(\Delta u - \Delta d)C_{ns} + \frac{1}{36}(\Delta u + \Delta d - 2\Delta s)C_{ns} + \frac{1}{9}(\Delta u + \Delta d + \Delta s)C_s \\ \Gamma_1^d &= \frac{1}{36}(\Delta u + \Delta d - 2\Delta s)C_{ns} + \frac{1}{9}(\Delta u + \Delta d + \Delta s)C_s\end{aligned} \tag{1.44}$$

where the perturbative QCD singlet C_s and non-singlet corrections C_{ns} take the form [16] :

$$C_{ns} = 1 - \left(\frac{\alpha_s(Q^2)}{\pi}\right) - 3.5833\left(\frac{\alpha(Q^2)}{\pi}\right)^2 - 20.2153\left(\frac{\alpha(Q^2)}{\pi}\right)^3 - O(130)\left(\frac{\alpha(Q^2)}{\pi}\right)^4 \tag{1.45}$$

$$C_s = 1 - \left(\frac{1}{3}\frac{\alpha_s(Q^2)}{\pi}\right) - 0.5495\left(\frac{\alpha(Q^2)}{\pi}\right)^2. \tag{1.46}$$

These perturbative corrections allow us to make a meaningful test of the Ellis-Jaffe sum rules with experimental data taken at finite Q^2.

We know turn our attention to expected behavior of the asymmetries and structure functions at high and low x.

1.5 High x

The behavior of the structure functions at large Bjorken x has been predicted using perturbative QCD arguments. Essentially, as $x \to 1$ one parton is seen to be carrying

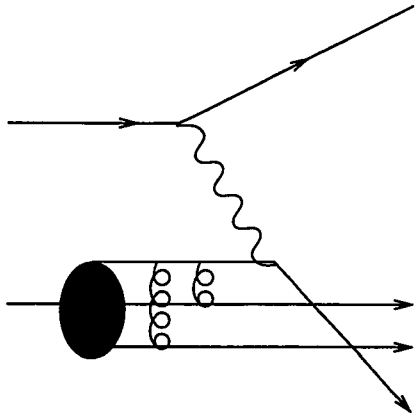

Figure 1.3: The exchange of two hard gluons can lead to one quark carrying a large fraction, x, of the nucleon momentum.

all of the momentum of the nucleon. Such highly off-shell partons are observed primarily when the three valence quarks exchange two hard gluons such that two of the valence quarks are stopped, and the third receives all of the momentum. One diagram contributing to this process is shown in Figure 1.3. The gluons exchanged have a large invariant mass, $k^2 \approx m^2/(1-x)$, where m^2 is the invariant mass of the stopped quarks, implying that the relevant strong coupling for the gluon emission, $\alpha_s(k^2)$, is small. This suggests that the quark and gluon distributions at large x can be extracted perturbatively. From these considerations, the quark distributions take the form [19]

$$q(x) \sim (1-x)^{2n-1+2\Delta S_z} \tag{1.47}$$

where n is the number of spectator quarks and ΔS_z is the absolute difference between the quark and hadron helicities; ΔS_z=0 for parallel quark and hadron helicities, ΔS_z=1 for antiparallel helicities. We expect that $n = 2$ in baryons : states with more quarks will be suppressed as $x \rightarrow 1$ because more hard gluons would have to be exchanged in order to stop the additional constituents. Thus the QCD counting rules suggest the high x behavior $q_+(x) \sim (1-x)^3$ and $q_-(x) \sim (1-x)^5$ for quark and baryon helicities parallel and antiparallel respectively. The fact that the antiparallel distribution is suppressed by $(1-x)^2$ is reasonable since the helicity dependent splitting functions have the approximate form $P_{d-\leftarrow p+}(z) \sim P_{d+\leftarrow p+}(z)(1-z)^2$, where p

is the parent, d is the daughter parton, and z is the fraction of the parent momentum transferred to the daughter. The implication is that the sign of the helicity of the parent parton is preferentially transferred to the daughter parton having the larger momentum fraction [20, 19], so at high x we can expect the quarks to carry the helicity of the baryon.

Some insight into the high x behavior is given by Farrar and Jackson [21] who considered the behavior of the two stopped quarks. In order to exchange a hard transverse gluon requires that the two quarks have opposite spin to conserve angular momentum. The exchange of a longitudinal gluon does not entail a spin flip, but this process is kinematically suppressed. Since the two quarks can form either a spin singlet S=0, or S=1, the argument suggests that in either case S_z=0 is preferred, and the energetic quark carries the spin of the nucleon. Close further suggests that the S=1 pairing may be suppressed since spin-spin forces prefer the spin singlet state [22].

Additional contributions to the structure functions at high x can come from the strange quarks and gluons. The leading contribution to the gluon distribution and strange quark distributions are expected to be $(1-x)^4$ and $(1-x)^5$ respectively [19], so the dominant behavior as $x \to 1$ will come from the valence quarks. This suggests that the asymmetry

$$\lim_{x\to 1} A_1 \sim \frac{\Delta q(x)}{q(x)} \to 1. \tag{1.48}$$

From these considerations, it is also expected that

$$\lim_{x\to 1} g_1 \sim (1-x)^3. \tag{1.49}$$

That the leading valence quark behavior varies as $(1-x)^3$ is a consequence of the Drell-Yan-West relation [22, 23, 24], which is another application of counting the number of spectator constituents. The relation correlates the high Q^2 behavior of the elastic form factor, F, with the $x \to 1$ behavior of the structure function F_2 :

$$\lim_{Q^2\to\infty} F(Q^2) \sim (Q^2)^{-N} \iff \lim_{x\to 1} F_2(x) \sim (1-x)^{2N-1}. \tag{1.50}$$

For the proton and neutron, the elastic form factors drop as Q^{-4}, so we extract the value N=2 and find $F_2(x \to 1) \sim (1-x)^3$.

1.6 Low x

From our discussions of the high x behavior of the parton distributions, we observed that in QCD processes such as $q \rightarrow qg$ when a quark radiates a gluon, and $g \rightarrow \bar{q}q$ in which a gluon splits into two quarks, the helicity information of the original parton is preferentially retained by the more energetic of the two partons found after splitting. This suggests that the low momentum partons, corresponding to small values of Bjorken x, will have helicities which are mostly uncorrelated with the nucleon as a whole, and the asymmetry measured at low x should tend to zero; $A_1 \rightarrow 0$ as $x \rightarrow 0$.

The behavior of the spin structure functions and asymmetries are important at low x since the integrals of g_1 over the full x range $x \in (0,1)$ are needed to test the sum rules. Since the experiments measure g_1 over a limited range in x, theoretical guidance is needed to perform the integral extrapolations at low and high x.

The detailed low x behavior of the asymmetries and spin structure functions has usually been extracted using Regge theory [25, 26]. In the Regge limit the center of mass energy is taken to be much greater than the momentum transfers and masses involved, $s \gg Q^2$ where s is the center of mass energy squared. Since s is related to the invariant mass of the hadronic system, $s = W^2 = M^2 + 2m\nu - Q^2$, the Regge limit is equivalent to $2M\nu \gg Q^2$. To ensure the process is deep inelastic, we have the additional requirements of large ν and $Q^2 \gg \Lambda_{\rm QCD}$. In this case, the Regge limit corresponds to the small x region $x = Q^2/2M\nu \approx Q^2/s \approx 1/s$ [26].

Regge theory suggests that the scattering amplitudes at high energies in DIS can be written as :

$$A(s,t) \sim s^{\alpha(t)} \tag{1.51}$$

where t is the momentum transfer. The optical theorem relates the forward, $t = 0$, part of the amplitude to the total cross section via :

$$\mathrm{Im}A(s,0) = s\,\sigma_{\rm tot} \;\Rightarrow\; \sigma_{\rm tot} \approx x^{1-\alpha(0)} \tag{1.52}$$

suggesting that the high energy behavior of the cross section at low x depends on x like a power law, controlled by the Regge intercept $\alpha(0)$ [26]. For the specific case of g_1, the low x behavior is expected to behave as the sum of a few Regge terms [28]:

$$g_1^N(x) \simeq \sum_i \beta_i x^{-\alpha_i(0)} \tag{1.53}$$

where the sum is over the intercepts of the $a_1(1270)$, $f_1(1285)$, and $f_1(1420)$ trajectories. Not much is known about the intercepts, but they are expected to be close in value so the leading behavior is expected to be described by a single power law [25, 28]:

$$g_1^N(x \to 0) \simeq \beta x^{-\alpha} \tag{1.54}$$

where Heimann [25] suggests for the leading intercept value $\alpha_{a_1}(0) = -0.14$, which lies inside the range $\alpha_{a_1}(0) \in (-0.5, 0.0)$, suggested by Ellis and Karliner based on results from πP scattering [28].

The low x behavior of both the spin dependent and spin independent structure functions has undergone a great deal of study recently, especially in light of the new data from HERA suggesting a dramatic increase in the magnitude of F_2 [29]. Several new forms for g_1 have been suggested, including $g_1(x \to 0) \sim (1 + 2\log x)$ [30], $g_1(x \to 0) \sim a\log(1/x)$, and $g_1(x \to 0) \sim [F_2(x)]^{\sqrt{2}}$ [27] which imply larger contributions to the low x extrapolation than those based on Regge theory. More precise data on g_1 are clearly needed to constrain the models and reduce the large theoretical uncertainties involved with the low x extrapolation.

1.7 Modeling the Neutron

We can combine our discussions of the previous sections and make a simple prediction for the form of A_1^n. Our SU(6) model suggested that for $x \sim 0.3$ we expect $A_1^n \sim 0$. The asymmetry at low x is supposed to go to 0, and at high x it's expected to go to 1. A model which manifests this basic behavior by Schäfer is shown in Figure 1.4 [31].

1.8 Polarized ^{3}He as a Polarized Neutron

In the experiment E142 we extracted the spin structure function of the neutron from that measured with a polarized ^{3}He target. The use of polarized ^{3}He as a polarized neutron has its origin in a few observations. In the crudest model of ^{3}He, the nucleons are in a spatially symmetric S state. The Pauli principle constrains the overall wavefunction to be antisymmetric, so the spin-isospin wavefunction must then be antisymmetric. Exchanging the two protons must yield a symmetric isospin wavefunction,

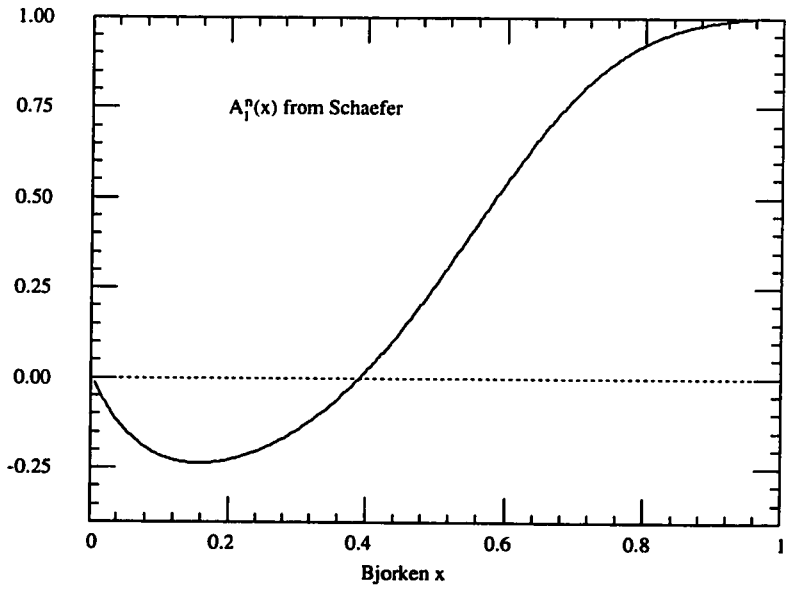

Figure 1.4: A model of Schäfer for $A_1^n(x)$ showing $A_1^n(x \to 0) = 0$, $A_1^n(x \to 1) = 1$ and $A_1^n(x \to 0.3) \approx 0$.

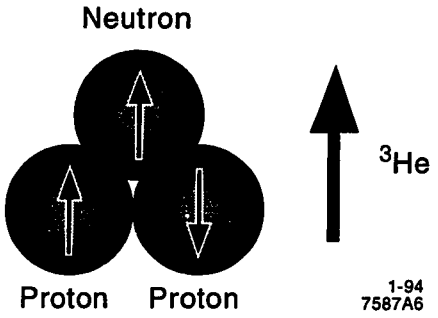

Figure 1.5: Pure S wave model of ^{3}He in which the proton spins cancel and the neutron is 100% polarized.

implying that the protons' spins are paired antisymmetrically in a spin singlet. In this picture, the protons have no net contribution to the spin of ^{3}He, which is carried exclusively by the neutron. Some support to prove that this is not drastically wrong comes from noting that the magnetic moment of ^{3}He is -2.12 nuclear magnetons, which is close to that of a free neutron, μ_n=-1.91 [32]. In such a model we would picture a ^{3}He nucleus as in Figure 1.5. A more realistic approach will include other components of the wavefunction. As an example, Blankleider and Woloshyn [35] used the wavefunctions computed by Afnan and Birrell, who had solved the Faddeev equation with a Reid soft-core potential [33]. Using an L-S coupling scheme of Derrick and Blatt [34] they decomposed the solution into components with the neutron and proton spins in particular directions [35]. The dominant partial wave components from [35] are given in Table 1.2. Here $P_n^{+(-)}$ is the number of neutrons aligned (antialigned) with the ^{3}He spin. The $P_p^{+(-)}$ refer to the protons, where $P_p^+ + P_p^- = 2$. The last column gives the percentage of each partial wave component, P(S), P(S′), and the average of the D state components, P(D), in the ^{3}He wavefunction. The S′ component has its origin in the small difference between the tensor T=0 and T=1 forces distorting the primary S wave configuration [32]. P wave components are suppressed in the ^{3}He wavefunction since they are of opposite (positive) parity.

In this model the net neutron polarization, $p_n = (P_n^+ - P_n^-)/(P_n^+ + P_n^-)$ is 86.3%, and each proton is 2.3% antialigned with the ^{3}He spin. Thus in a realistic model, the neutron is slightly depolarized, and the proton has a small negative contribution.

Partial Wave	L	S	P_n^+	P_n^-	P_p^+	P_p^-	%
S	0	1/2	1	0	1	1	88.6
S'	0	1/2	2/3	1/3	4/3	2/3	1.54
D	2	3/2	1/3	2/3	2/3	4/3	8.37

Table 1.2: The dominant partial wave components of ^{3}He are listed.

A general scheme was devised by Friar *et al.* to allow the relative neutron and proton polarizations to be extracted from other models [32]. Denoting

$$\begin{aligned} P_n^+ &= 1-\Delta \\ P_n^- &= \Delta, \text{ where } \Delta = [P(S')+2P(D)]/3 \end{aligned} \tag{1.55}$$

and

$$\begin{aligned} P_p^+ &= \frac{1}{2}-\Delta' \\ P_p^- &= \frac{1}{2}+\Delta', \text{ where } \Delta' = [P(D)-P(S')]/6 \end{aligned} \tag{1.56}$$

allows us to write $p_n = 1-2\Delta$ and $p_p = -2\Delta'$, where the effects of realistic wavefunctions are included in Δ and Δ'. We now discuss increasingly sophisticated models for ^{3}He.

In the simplest model, a pure S wave, $\Delta = \Delta' = 0$, so the neutron is 100% polarized. This implies

$$A_1^{^3\mathrm{He}}(x) = \frac{F_2^n(x)}{[F_2^n(x)+2F_2^p(x)]} A_1^n(x) \quad \text{and} \quad g_1^{^3\mathrm{He}}(x) = g_1^n(x). \tag{1.57}$$

To incorporate more realistic wavefunctions, the quantities Δ and Δ' were extracted from many models, and a fit yielded the averages $\Delta = 0.07 \pm 0.01$ and $\Delta' = 0.014 \pm 0.002$ where the errors are a subjective estimate of the spread of the model results [32]. The best fit average nucleon polarizations were calculated by Friar *et al.* to be $p_n = 0.86 \pm 0.02$ and $p_p = -0.027 \pm 0.004$. Ignoring other nuclear effects such as Fermi motion and binding effects, we can write the asymmetry and spin structure function as [36]

$$A_1^{^3\mathrm{He}}(x) = \frac{F_2^n(x)}{[F_2^n(x)+2F_2^p(x)]} p_n A_1^n(x) + \frac{2F_2^p(x)}{[F_2^n(x)+2F_2^p(x)]} p_p A_1^p(x) \tag{1.58}$$

and

$$g_1^{^3\mathrm{He}}(x) = p_n g_1^n(x) + 2p_p g_1^p(x). \tag{1.59}$$

This model incorporates the effective nuclear polarizations and suggests that the largest effect on $A_1^{^3\mathrm{He}}$ from the protons comes at high x where the proton asymmetry is large.

Another level of sophistication was added in order to investigate the effects of Fermi motion and binding. In the Bjorken limit we can write g_1^A for a nucleus in terms of its constituent nucleons as [36]

$$g_1^A(x) \approx \sum_N \int_x^1 dz \frac{1}{z} g_1^N(x/z) \int dE \int d\mathbf{p} \Big[P_N^+(\mathbf{p},E) - P_N^-(\mathbf{p},E)\Big] \delta(z - p^+/M) \tag{1.60}$$

where z is the nucleon light cone momentum fraction, p^+ is the light cone momentum component, and the $P_N^{+(-)}$ are the spectral functions describing the probability of finding a nucleon, N, with energy E and momentum $\mathbf{p}$ with helicity parallel (antiparallel) to the nucleus. The spectral functions are normalized such that

$$\int dE \int d\mathbf{p} \Big[P_N^+(\mathbf{p},E) - P_N^-(\mathbf{p},E)\Big] = p_N \tag{1.61}$$

is the net nucleon polarization,

The equations (1.58) and (1.59) correspond to setting $z = 1$ above. After the complete calculation in (1.60), for x<0.9 the results were within 5% of those in equation (1.59), suggesting that Fermi motion and binding effects have only a limited effect [36]. The individual contributions of the proton and neutron to $g_1^{^3\mathrm{He}}$ can be seen in Figure 1.6 taken from Woloshyn [37]. The dominance of the neutron contribution is clearly seen. Other nuclear effects such as meson exchange currents have not been investigated, but as these make only a modest contribution to the magnetic moment of ^{3}He [32], it would be surprising if they had a large effect in spin dependent DIS. The repercussions of final state interactions have not been investigated.

The results above suggest that the dominant nuclear effects (modulo the unknown effects of final state interactions and meson exchange currents) come from the small S′ and D wave components which change the effective nucleon polarizations inside the nucleus. This effect is small and independent of the shape of the constituent nucleon spin structure, g_1^N. Thus a reasonably accurate picture of polarized ^{3}He sees it as

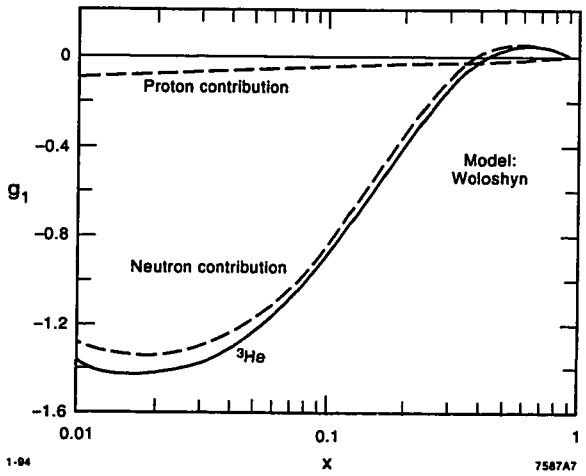

Figure 1.6: The neutron and proton contributions to $g_1^{^3He}$ are shown in this plot from Woloshyn.

an 86% polarized neutron with two protons polarized 2.7% in the opposite direction to the ^{3}He spin. We conclude that g_1^n can be extracted reliably from the measured $g_1^{^3He}$ using equation (1.59), if we include a 5% systematic error to account for Fermi motion and binding effects [36]. Thus polarized ^{3}He serves us very well as a polarized neutron.

1.8.1 The Axial Anomaly and other Complications

The expectation is that the nucleon spin can be decomposed into components :

$$\frac{1}{2} = \frac{1}{2}\Sigma + \Delta g(Q^2) + L_z(Q^2) \tag{1.62}$$

where L_z is the orbital angular momenta, and Δg is the gluon contribution to the spin. The latter quantity may be substantial since gluons are known to carry roughly 50% of the momentum. The SU(3) considerations suggest that Σ is 0.6, which contrasted sharply with the shocking result of EMC that Σ was consistent with zero. A part of the resolution of this puzzle was the recognition of a gluon component which mixed in with the quark spin. Naively one expects the gluon contribution to vanish as α_s, but the anomalous dimension was found to be -1, so that Δg varied as $log(Q^2)$ [38].

This axial anomaly gave rise to a new interpretation of the spin measured in deep inelastic scattering :

$$\tilde{\Delta}q = \Delta q - \frac{\alpha_s(Q^2)}{2\pi}\Delta g(Q^2). \tag{1.63}$$

The product of α and Δg is non-vanishing to leading order as Q^2 evolves, leading to a finite reduction seen in the measured spin of the quarks. An interesting observation is that since α_s decreases rapidly with increasing Q^2, then the gluon contribution must grow. In equation (1.62) this implies that the orbital angular momentum must grow large and negative to compensate [39].

Higher twist terms in the integral, of the form $C_n/(Q^2)^n$ can also make contributions to the spin structure function integrals, especially at the low Q^2 at SLAC. Estimates of these terms are difficult to make, and controversial, but the most recent results suggest that they are small [40].

Chapter 2

Experiment Apparatus

2.1 Experiment Overview

The experiment E142 took data for six weeks starting in November of 1992 at the Stanford Linear Accelerator Center (SLAC). The essence of the experiment was to accelerate polarized electrons in the two mile long linear accelerator to energies of 22.66 GeV, and then divert them to End Station A (ESA) which contained the polarized ^{3}He target. A fraction of the electrons scattered from the target were detected in two independent magnetic spectrometers located at 4.5° and 7.0° away from the incident beam direction in ESA. The experiment ran predominantly in two configurations, one in which the spins of the electron beam and ^{3}He were parallel, the second in which they were antiparallel. By measuring the difference in scattering rates from the two cases, the asymmetry, $A_1^n(x,Q^2)$, and spin dependent structure function, $g_1^n(x,Q^2)$ were extracted. A schematic of the experimental setup is shown in Figure 2.1. In

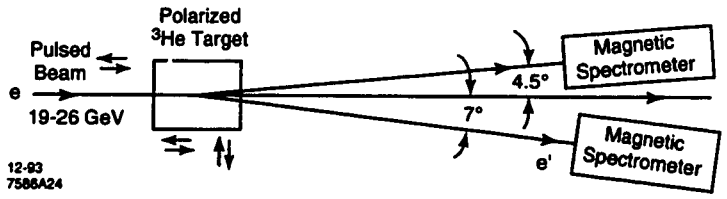

Figure 2.1: The layout of the experiment E142 is shown.

this chapter we will describe the hardware used to perform the measurement, starting from the polarized electron source, and ending in the counting house (CHA) where the data acquisition computers were located.

2.2 Polarized Electron Source

The polarized electrons were produced by photoemission from an AlGaAs photocathode, in a manner fully described by Woods *et al.* [41, 42]. Initiating the process was a Candela Ti:sapphire flash lamp pumped dye laser. This laser used Oxazine 720 dye to produce 0.9-1.4 μs long pulses of light at 715 nm. The width of the pulses was controlled with SLC's Laser Pulse Chopper (LPC) and the peak intensity was kept uniform with the Top Hat Pulse Shaper (TOPS). From here, a Beam Intensity Control (BIC) system regulated the overall intensity of the light on the photocathode as a means of controlling the current. A schematic of the polarized source is presented in Figure 2.2.

After passing through BIC, the initially linearly polarized light was converted to 99% circularly polarized light by a Pockels cell. By applying a positive or negative voltage to the cell we could produce either left or right hand circularly polarized light on a pulse-to-pulse basis. This circularly polarized light illuminated a photocathode consisting of a 0.3 μm thick active layer of $Al_{0.12}Ga_{0.88}As$ doped with Be at 6×10^{18} cm^{-3}. The photocathode was placed in Diode Gun 1 and operated at 0°C and 60 kV. The addition of 12% Al served to increase the bandgap of GaAs from 1.43 eV to 1.63 eV, which has the advantage that the peak polarization was achieved using light at $\sim$ 710 nm which is readily available. Laser light at 760 nm required by pure GaAs photocathodes [43] is more difficult to produce. In Figure 2.3 we show the band structure of pure GaAs. Positive helicity light (left hand circularly polarized) around 1.43 eV excites the transitions from the valence band to the conduction band with the probability for a $|3/2,-3/2> \rightarrow |1/2,-1/2>$ transition favored by a factor of 3 over $|3/2,-1/2> \rightarrow |1/2,1/2>$ [44]. This implies that positive helicity photons will preferentially photoemit electrons with spin opposite to the incident photons. However, since the electrons are emitted in a direction opposite to that of the photons, we see that positive helicity photons will produce, theoretically, a 50% polarized

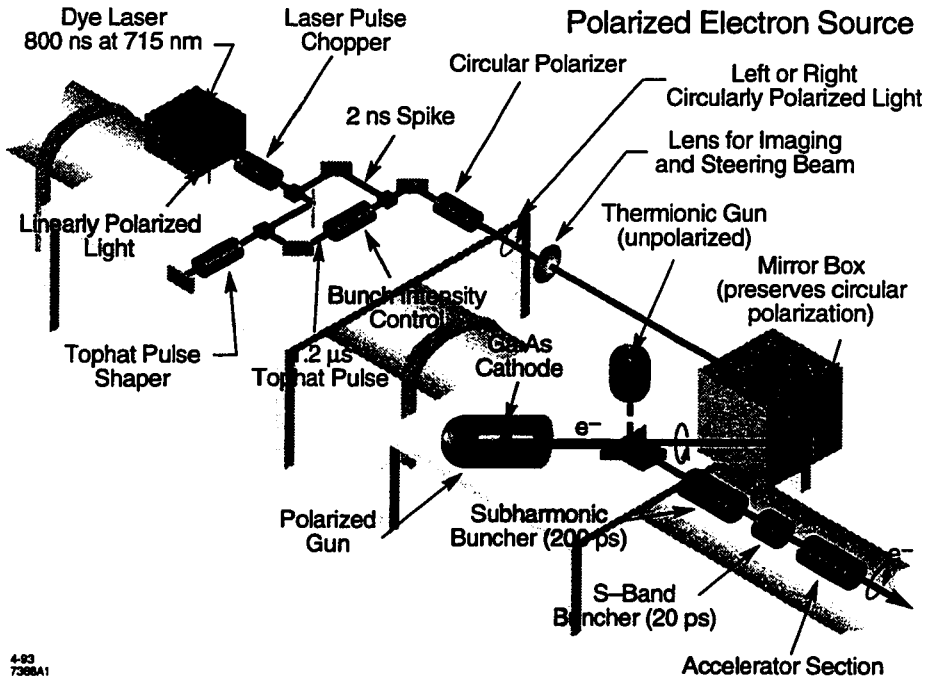

Figure 2.2: Schematic of the polarized electron source used by E142.

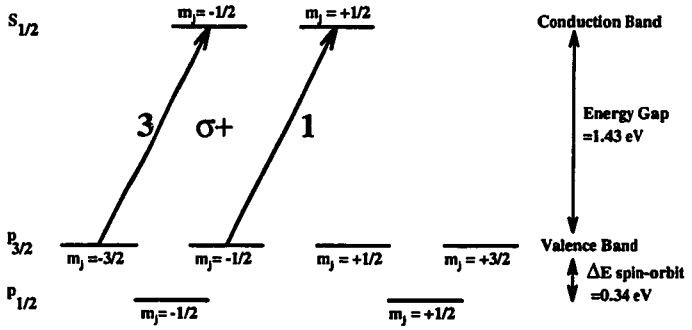

Figure 2.3: Here we show the band structure of pure, unstrained GaAs. The arrows denote the transitions occurring when illuminated with positive helicity 1.43 eV photons. The numbers reflect the relative transition probabilities.

sample of positive helicity electrons [45][1].

After photoemission the electrons were accelerated across the 60 kV potential of the gun, creating a 0.9-1.4 μs pulse of $\sim$ 0.5-2.5$\times 10^{11}$ electrons which were captured by the pre-buncher, after which they were bunched and accelerated down the linac. We note that although the source operated at 120 Hz, E142 only used the first 119 pulses. The 120th pulse was a short, 2 ns pulse used for accelerator diagnostics and tuning.

Throughout the six week run, the quantum efficiency of the system remained stable between 0.7% and 0.9%, and the gun was not re-cesiated.

2.2.1 Beam Acceleration and Transport

The electrons created at the source were bunched and then entered the 3.2 km linear accelerator. The accelerator structure consists of 30 sectors, each containing eight klystrons, steering dipoles, a quadrupole, and additional elements for monitoring the beam position and current. Each of the 240 klystrons feed microwave radiation at 2856 MHz into copper cavities, in which the crests of the RF field accelerate the electrons for an average energy gain of 6 MeV/m over the length of the linac [49].

[1]Since E142, the introduction of strained lattice GaAs photocathodes has removed the j=3/2 valence band degeneracy to make 100% polarization possible. In fact, >85% polarizations have already been achieved [46].

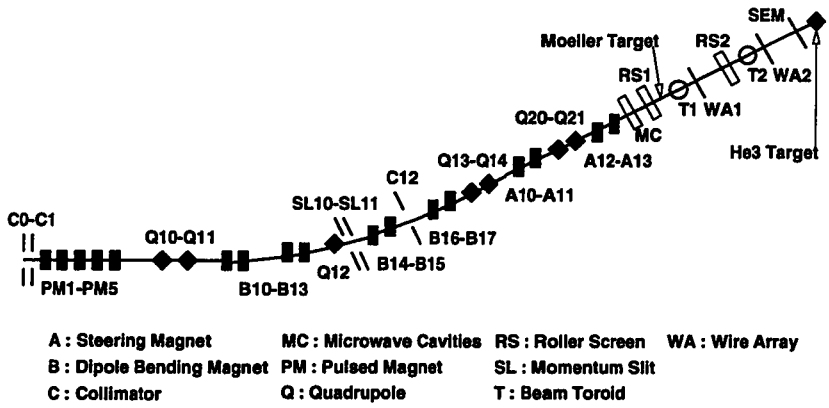

Figure 2.4: The main elements of the A-line beam transport system are shown.

At the end of the linac, the beam is diverted by pulsed magnets located in the Beam Switch Yard (BSY) into the A-line, which transports the beam to the target and detectors located in End Station A (ESA). The A-line consists of eight identical 3 m long dipole magnets (B10-B17) operated in series, each of which bent the beam by 3.0° from the linac towards ESA. Interspersed were seven quadrupoles (Q10-14 and Q20-21) used to control the beam divergence and spot size at the target.

2.2.2 Beam Monitoring

Beam Energy

The energy of the beam was monitored continuously and recorded every five minutes using a flip-coil located in one of the dipoles. The current induced in this rotating coil is proportional to the magnetic field strength of the dipoles. In turn, the magnetic field strength determines the momentum of the electrons passing through the A-line to about 0.1%. The energy spread of the beam, $\Delta E/E$, entering ESA was restricted to 0.7% full width by using three adjustable slits SL10F, SL10R and SL11 located in the A-line. A schematic of the A-line is presented in Figure 2.4.

Beam Current

On a pulse-to-pulse basis the beam charge was measured with two independent ferromagnetic toroids, with one located about 38 m upstream of the target, and the

second a few meters upstream. As the beam passed through the ferrite core of the toroid, a signal was induced in a loop of wire wrapped around the toroid, which in turn was connected to a resonant LC circuit. The current induced was amplified and integrated, with the total charge being proportional to the beam current [50]. Each toroid was calibrated by dumping the charge from a precisely charged capacitor through the toroid and measuring the induced charge. From this, calibration coefficients were extracted daily for each toroid, enabling the total beam charge of each spill to be measured to about 0.5%.

Beam Position and Steering

The beam position and width were monitored with a set of $\hat{x} - \hat{y}$ wire arrays placed 2.5 m upstream and 7.5 downstream of the target. Each of the 24 wires in $\hat{x}$ and $\hat{y}$ were made of 0.127 mm diameter CuBe, with a spacing of 0.635 mm in the upstream wire array, and 1.0 mm in the downstream array. The wire arrays were read out on a pulse-to-pulse basis by our Beam Control System (BCS) and this information was used to perform minor steering corrections to the beam. The fine adjustments were made by controlling the current of four vernier steering magnets, A10 (horizontal corrector) A11 (vertical corrector) located 168 m upstream of the target, and A12-A13 located 120 m upstream. The steering corrections were the only part of the beam controlled by the experimenters in ESA.

Two mylar roller screens, coated with fluorescent ZnS and observed with television monitors, were rotated into the beam and allowed a coarse centering and focusing of the beam. This was of use primarily after we changed targets, or when the beam was being reintroduced to ESA after a stoppage. These were removed before taking data. Additional information, used by the Main Control Center (MCC) to adjust the beam, came from two paddles of scintillator. The first piece was located upstream of the target beside the beampipe and was sensitive to beam halo and scraping. The second piece was downstream of the target, several meters away from the beampipe. Since it was sensitive to debris created at the target, it served as a good indicator of the time structure of the beam. Other monitors of the beam included two microwave cavities located $\approx$ 50 m upstream of the target. One cavity produced an RF signal proportional to the deviation of the beam from the horizontal center of the cavity,

the second was sensitive to vertical displacements. A final system used for beam monitoring and target protection was a secondary emission monitor (SEM) made of an aluminum foil with a circular aperture for the beam, placed immediately upstream of the target. Large signals from the SEM indicated dangerous excursions of the beam and would trigger a shutdown without operator intervention. This prevented the beam from hitting the thick side walls of the target.

2.2.3 Spin Precession

The helicity of the electrons entering the linac is the same as that of the photons hitting the photocathode (to the extent that the beam is polarized). Acceleration in the linac did not alter the helicity of the electrons, which remained constant up to the end of the linac. Here, pulsed bending magnets deflected the beam 0.5° north into the A-Line, and the set of eight dipole bending magnets each bent the beam another 3.0° north into ESA. In the course of being deflected into ESA, the electrons' spin precessed by an amount

$$\Delta\theta_{\text{precession}} = \gamma\Delta\theta_{\text{bend}}\left[\frac{g-2}{2}\right] \tag{2.1}$$

where $\Delta\theta_{\text{bend}}$=24.5°, and g=2.002319304 is the gyromagnetic ratio of the electron [51]. For beam energies which are an even multiple of 3.23742 GeV, the electron helicity at the target in ESA will be the same as it was at the source. This was the case for the E142 runs using E_{beam} of 19.42 and 25.90 GeV. For the majority of the data which were taken at 22.66 GeV, which is an odd multiple, the helicity of the electron as it entered ESA was opposite to that at the source.

2.2.4 Electron Beam Helicity Reversal

The ability to reverse the beam polarization on a pulse-to-pulse basis with the Pockels cell was very important for reducing systematic errors. Possible false asymmetries due to slow changes in spectrometer acceptance were averaged out by the rapid beam helicity reversals. Also, by changing the target polarization direction, we could further average over asymmetries induced by possible helicity-dependent differences in the beam properties. During E142, a positive voltage applied to the Pockels cell

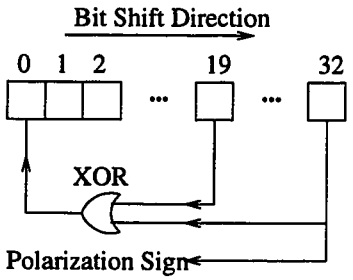

Figure 2.5: The polarization of the beam was set pulse-to-pulse by a pseudo-random number generator, using a simple feedback scheme illustrated here.

would produce positive helicity photons, while a negative voltage yielded negative helicity light [48]. The absolute helicity of the light was determined using a technique involving total internal reflection in a prism [47], and the helicity of the electrons was verified by Møller scattering [48].

On a pulse-to-pulse basis, the beam helicity was chosen using a pseudo-random bit generator. The sequence began when a 32 bit random number was chosen, with the last (32nd) bit determining the helicity of the beam. For the next pulse, the 19th and 32nd bits were XORed with the result being put in the place for the 1st bit, after the remaining bits had been shifted up. The new 32nd bit determined the helicity of this pulse, and the cycle was repeated. A schematic of this operation is shown in Figure 2.5. The polarization state of the beam was sent to the Counting House computers via three physically distinct pathways, termed the Mach line, Pockels Cell High Voltage Line, and the Veto Bits. Each pathway consisted of a pair of cables each carrying either a high or low level, where the combination '01' referred to positive helicity photons (hence positive helicity electrons *at the source*), and '10' meant that the photons incident on the photocathode were of negative helicity. Any other combination of bits signaled an error. The integrity of this system is discussed in Chapter Three.

2.3 Møller Polarimeter

2.3.1 Apparatus

A single arm Møller polarimeter was constructed to measure the electron beam polarization in ESA. The target consisted of a foil holder which could move any of three thin ferromagnetic foils into the beamline. The foils were 20 μm, 30 μm, and 50 μm thick, and composed of Permendur (49% Fe, 49% Co, 2% Va). Magnetizing a thin foil mounted at 90° to the beam requires impractically large fields, so the foils were inclined at 20° with respect to the beam and magnetized along the beam direction by a 100 G field from a set of Helmholtz coils. This target assembly was placed in the alcove of ESA upstream of the ^{3}He target. To restrict the rates in the Møller detector, a 20 radiation length tungsten mask was placed 7.11 m downstream of the target. This septum had a 31.75 mm diameter hole for the electron beam to pass through, and a 48 mm $\times$ 10.2 mm aperture for the Møller electrons, defining an angular scattering range in θ of 4.35 to 11.15 mrad. Momentum selection was accomplished with a dipole magnet, 18D72, whose magnetic center was 8.70 m from the target. The dipole operated at 91 kG with an $\int \mathbf{B} \cdot d\mathbf{l}$ of 14.5 kG·m to select electrons with momenta 10.0 GeV/c $\pm$ 2.9%, which were bent vertically downwards by 53 mrad. These Møller scattered electrons were detected in an instrumented lead brick 22.4 m from the target foils. The detector had an active area of 108 mm $\times$ 36 mm and consisted of 35 2.38 mm thick brass proportional tubes of 4 mm diameter arranged in two staggered rows, yielding a final θ acceptance from 5.0 to 10.5 mrad. To reduce the soft γ background and to amplify the response, a 6 radiation length lead plate was positioned in front of the tubes. Each tube subtended 4 mm/22.4 m = 0.18 mrad to image a Møller peak whose width was $\sigma \approx 0.26$ mrad. A schematic of the apparatus is shown in Figure 2.6.

2.3.2 Møller Asymmetry

The cross section for polarized e^-e^- scattering is fully calculable in QED, and in the CM frame takes the form [52]

$$\frac{d\sigma}{d\Omega} = \frac{\alpha^2}{s}\frac{(3+\cos^2\theta)^2}{\sin^4\theta}[1 - P_z^B P_z^T A_z(\theta)], \text{ where } A_z(\theta) = \frac{(7+\cos^2\theta)\sin^2\theta}{(3+\cos^2\theta)^2}. \quad (2.2)$$

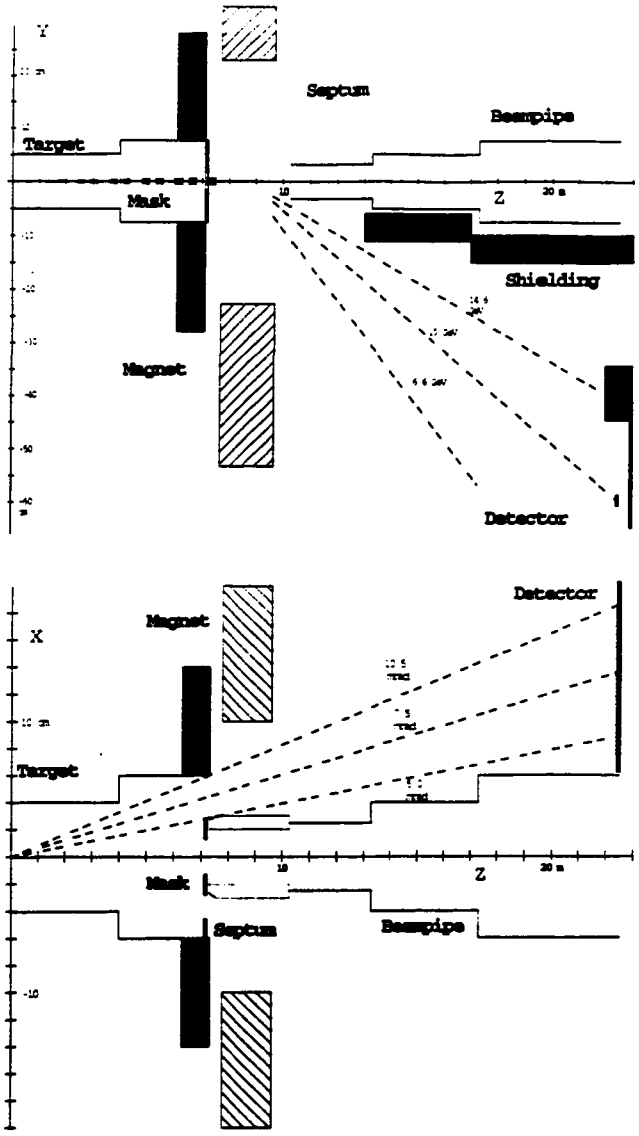

Figure 2.6: Side view and top view of the Møller polarimeter apparatus

Here θ is the CM scattering angle, $P_z^B(P_z^T)$ is the beam (target foil) longitudinal polarization. By measuring the Møller scattering rate for the electron beam and target spins aligned, $\sigma^{\uparrow\uparrow}$, and antialigned, $\sigma^{\uparrow\downarrow}$, we can form the asymmetry [54]

$$A = \frac{\sigma^{\uparrow\uparrow} - \sigma^{\uparrow\downarrow}}{\sigma^{\uparrow\uparrow} + \sigma^{\uparrow\downarrow}} = P_z^B P_z^T A_z(\theta). \tag{2.3}$$

The target polarization at saturation can be estimated from the approximation that 2 of the 3d (M shell) electrons in Fe are aligned with the external field and the remaining 24 are unpolarized, yielding 2/26=7.7% polarization. The E142 polarimeter operated at a CM angle of 97° (backgrounds were too large at 90°), corresponding to $A_z(\theta)$=0.76. Using a beam polarization of $\approx$ 35% we can estimate the Møller asymmetry as roughly 2%. The laboratory frame scattering angle, θ_L, is given by

$$\tan\theta_L = \sqrt{\frac{2m_e}{E_{\text{beam}}}\frac{\sin\theta}{1+\cos\theta}} \Rightarrow \theta_L = 7.6 \text{ mrad}. \tag{2.4}$$

2.3.3 Foil Polarization

In practice the foil polarization is determined by measuring its magnetization, **M**. Ramping the external field, **H**, will induce a voltage in a pickup coil wound around the foil due to the changes in magnetic flux, $\int V dt = \phi_f - \phi_i$. The flux has contributions from the foil and air :

$$\phi = N_{\text{turns}} \times [\mathbf{B}_{\text{foil}} \cdot \mathbf{A}_{\text{foil}} + \mathbf{H} \cdot (\mathbf{A}_{\text{coil}} - \mathbf{A}_{\text{foil}})]. \tag{2.5}$$

By integrating the induced voltage with and without the foil, and noting that $\mathbf{B}_{\text{foil}} = \mathbf{H} + 4\pi\mathbf{M}$, we find [53]

$$4\pi|\mathbf{M}| = \frac{1}{N_{\text{turns}}|\mathbf{A}_{\text{foil}}|}\left[\int_{\text{foil in}} V dt - \int_{\text{foil out}} V dt\right]. \tag{2.6}$$

The magnetization is related to the foil polarization by

$$P_z^T = \left[\frac{g_e}{(g_e-1)}\frac{g_{\text{eff}}-1}{g_{\text{eff}}}\right]\frac{|\mathbf{M}|}{n\mu_B} \tag{2.7}$$

where the gyromagnetic ratio of the electron, g_e = 2.002319304, the gyromagnetic ratio of Permendur, $g_{\text{eff}} = 1.885 \pm 0.005$, n is the number density of electrons, and μ_B is the Bohr magneton [55].

Source of Uncertainty	Contribution
Gyromagnetic ratio of Permendur, g_{eff}	0.3%
Air flux measurement reproducibility	2%
Foil thickness uncertainty	2%
Background subtraction	2%
Difference in results from 20 and 30 μm foils	1%
Levchuk effect	2%
Total Systematic Error	4.1%

Table 2.1: Sources of systematic error in determining the beam polarization.

2.3.4 Systematic Errors

The systematic errors on the polarization measurement are estimated as follows. Uncertainty in g_{eff} contributes a 0.3% error to $4\pi|\mathbf{M}|$. The $\int_{\text{foil out}} V dt$ air flux measurements taken before and after E142 showed a 2% variation. Foil thickness uncertainty contributes another 2%. Subtraction of the radiative Møller and other backgrounds adds 2%. The 20μm and 30μm foils yielded results for the beam polarization that differed by 1% which we also add in quadrature with the other factors. Finally, the motion of bound electrons in the target foils smears the lab frame scattering angle (the Levchuk effect [56]) by a maximum amount $\tan\theta_{\text{smeared}} \approx \tan\theta_{\text{unsmeared}}\sqrt{1-|\mathbf{P}|/m_e}$, where $|\mathbf{P}|$ is the momentum of the struck electron $\approx \sqrt{2m_e|E_b|}$ where E_b is the binding energy. For the K-shell of Fe, $|E_b| \approx 7.13$ keV, so the scattered K-shell electrons are smeared out by 9%. The lineshapes of the different shells and hence the unpolarized and polarized electrons in the foil are affected differently. Experimentally, the consequences of this effect depend on how much of the Møller peak is detected. As the fraction of the peak which is detected gets smaller, the measured asymmetry will get larger since the relative contribution of events from the unpolarized, inner shell electrons will decrease. Modeling this effect contributes a further 2% uncertainty. Finally we quote a total relative systematic error of 4.1% on the beam polarization.

2.3.5 Beam Polarization Results of the Møller Runs

Møller data were taken daily, for a total of 200 runs. Each run consisted of roughly 15000 spills (with the polarization reversed randomly on a pulse-to-pulse basis). The proportional tubes were attached to ADCs, and the total charge accumulated in a channel per spill was proportional to the number of electrons hitting the tube. Non-linear behavior of the ADCs at low charges was observed and appropriate corrections were made. About 100 electrons were detected per spill. To determine the scattering asymmetry, the average signal in each detector channel was calculated for each helicity of the beam. Unpolarized background and the radiative Møller tail were subtracted and then an asymmetry was formed channel by channel, as in Figure 2.7. After correcting the observed asymmetry for the Levchuk effect, the beam polarization was inferred from equation (2.2). The Møller data suggest there was no variation of the beam polarization during the 22.66 and 19.42 GeV runs (see Figure 2.8), which is to be expected since the electron gun was not re-cesiated during the experiment so the gun quantum efficiency and polarization were expected to be stable. For the 22.66 and 19.42 GeV runs, we quote a final beam polarization of $35.8 \pm 0.3(\text{stat}) \pm 1.5(\text{sys})$. The 25.51 GeV runs had a slightly lower, but still stable polarization of 32.5%, since we were forced by problems with the A-line magnets to run below the energy of 25.896 GeV which is optimal for integral spin precession in the arcs. This had been the highest energy ever run into ESA.

2.4 Polarized ^{3}He Target

This experiment was made possible by recent developments in constructing high density polarized ^{3}He targets. Whereas techniques for polarizing ^{3}He by metastability exchange [57] and spin exchange with optically pumped alkali vapor [58] have been known since the early 1960s, elucidation and control of the relevant experimental factors to produce sufficient density and polarization have taken 30 years [59, 60, 61, 62, 63, 64, 65].

The E142 target target was a two-chambered 30 cm long glass cell holding ^{3}He at densities of 2.3×10^{20} atoms/cm^3. The cell sat in a 30 G holding field and $\approx$ 33% polarization was achieved by spin exchange with optically pumped Rb vapor. The

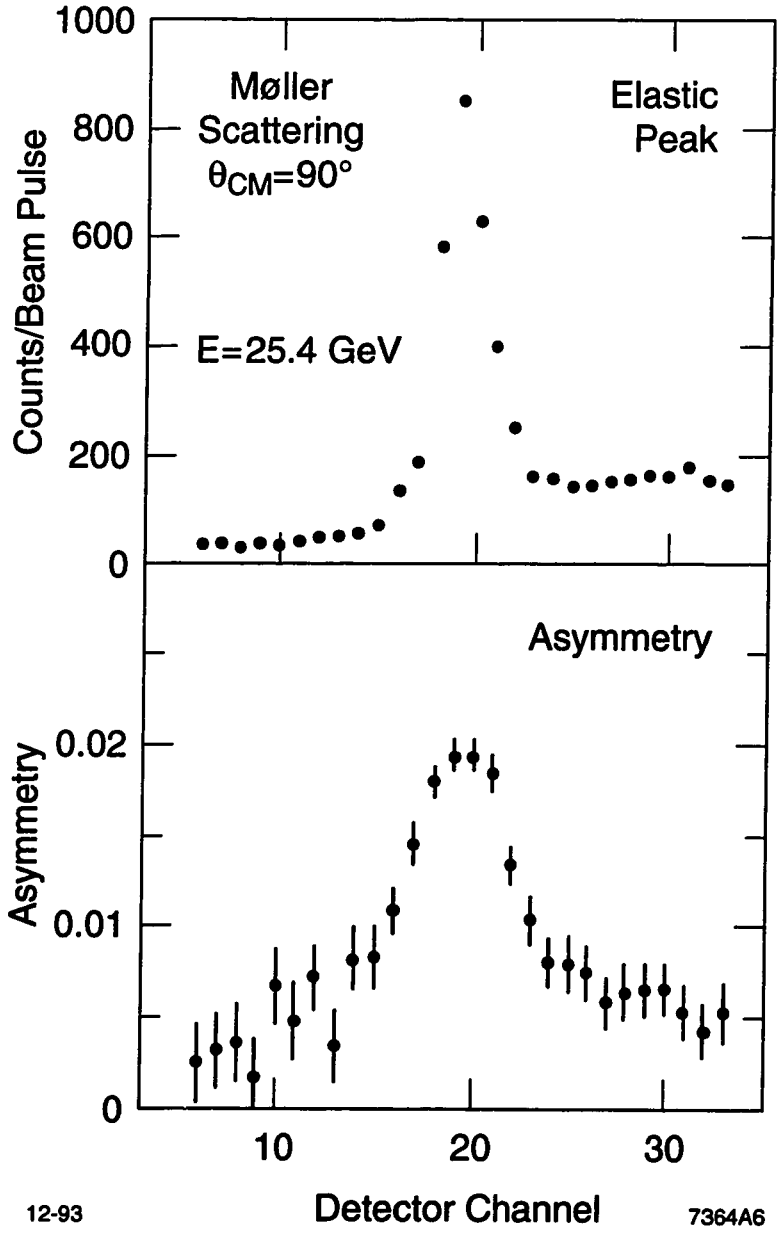

Figure 2.7: Møller scattering asymmetry

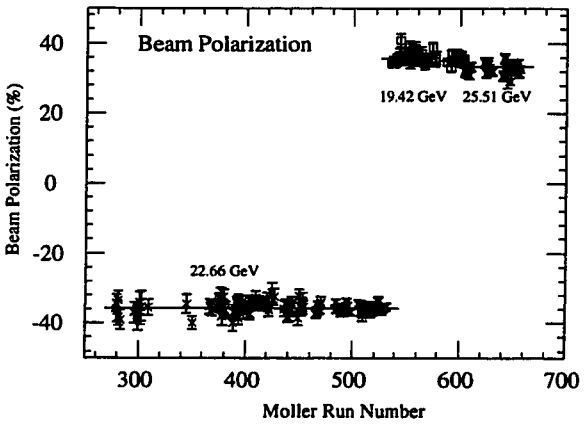

Figure 2.8: The beam polarization measured from the Møller runs is shown here for the three beam energies used during E142. The negative sign of the polarization for the E_{beam}=22.66 GeV/c runs indicates the helicity of the beam at the Møller target is opposite to that at the source due to spin precession in the arcs.

target is fully described by Middleton [66] so only a few details are presented here for completeness.

2.4.1 Optical Pumping and Spin Exchange

High density targets can be achieved most easily using the technique of optical pumping. In our case, positive helicity (for example) circularly polarized laser light at 794.7 nm excites the $5S_{1/2}$ ($m_s = -1/2$) ground state to the $5P_{1/2}$ ($m_s = +1/2$) in rubidium vapor (the D1 line). Radiative decays to the ground state favor the $5S_{1/2}$ ($m_s = -1/2$) state over $5S_{1/2}$ ($m_s = +1/2$) state by a factor of two. Then, for every three photons absorbed, we would increase the population of the $5S_{1/2}$ ($m_s = +1/2$) by one. By adding 65 torr of N_2, as in our target cells, the $5P_{1/2}$ ($m_s = \pm 1/2$) are collisionally mixed at a rate exceeding the radiative decay. The relaxation into the $5S_{1/2}$ ground states now occurs equally into the two magnetic substates, and only two photons are required to increase the $5S_{1/2}$ ($m_s = +1/2$) population by one [67]. The pumping scheme is shown in Figure 2.9. The polarization of the valence electrons of Rb com-

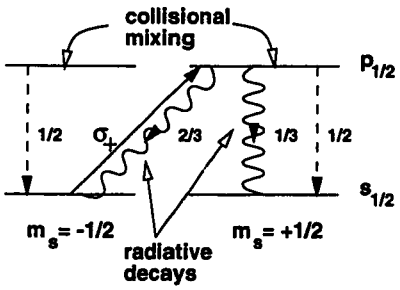

Figure 2.9: The optical pumping scheme is illustrated for positive helicity circularly polarized light. For every two photons absorbed, the $m_s = +1/2$ population increases by one.

petes with several depolarizing mechanisms, the most important of which are spin destruction from Rb-Rb and Rb-^{3}He collisions (the latter is dominant at high pressures), as well as Rb-target cell wall interactions. However, with an optically thick Rb vapor (10^{14} atoms/cm^3) and sufficient laser power, the optical pumping rate of $1/\Gamma_{\rm opt} \approx 10^{-6}$ s dwarfs the competing $1/\Gamma_{\rm sd} \approx 10^{-3}$ s rate of spin destruction, so Rb polarizations of $\approx 100\%$ can be achieved.

The Hamiltonian for spin exchange between the electrons of Rb and the nucleus of ^{3}He has the form of a dipole-dipole interaction between the ith Rb electron's magnetic moment, $\mu_B \mathbf{S}_i$, and the ^{3}He nuclear magnetic moment, $\gamma_{^3He}\mu_N \mathbf{I}$;

$$H_{\rm SE} = -2\gamma_{\rm ^3He}\mu_N\mu_B \sum_{\rm Rb\ electron\ i} \left[\frac{\mathbf{I}\cdot\mathbf{S}_i - 3(\mathbf{I}\cdot\hat{\mathbf{r}}_i)(\mathbf{S}_i\cdot\hat{\mathbf{r}}_i)}{r_i^3} - \frac{8\pi}{3}\delta(i)\mathbf{I}\cdot\mathbf{S}_i\right]. \qquad (2.8)$$

Here r_i is the distance between the ith Rb electron and ^{3}He nucleus, μ_B and μ_N are the Bohr and nuclear magnetons, and $\gamma_{\rm ^3He} = 3.243$ kHz/G is the gyromagnetic ratio of ^{3}He. The Fermi contact term in the hyperfine Hamiltonian corresponds to the overlap of the Rb electron with the ^{3}He nucleus. This hyperfine interaction which transfers angular momentum from the valence electron to the ^{3}He nucleus, is enhanced in noble gases [68, 69] and dominates the spin exchange cross section which is $\approx 10^{-24}$ cm^2 [59] [2]. The spin exchange rate, $\Gamma_{\rm SE}$, will be proportional to the relative velocity

[2]It is clear now why alkali metals are used, and interesting to note that in muonic ^{3}He this cross section goes up by 10 orders of magnitude. Rubidium is a suitable alkali to use because lasers to pump the D1 line are readily available.

between the ^{3}He and Rb, v, and to the number density of Rb, [Rb];

$$\Gamma_{SE} \equiv < \sigma_{SE} v > [\mathrm{Rb}] \tag{2.9}$$

where the velocity averaged cross section is $\approx 1.2 \times 10^{-19}$ cm^2/s [70]. With [Rb] $\approx 10^{14}$ cm^{-3}, polarization times for ^{3}He are of the order of hours, $1/\Gamma_{SE} \approx 25 - 40$ hours. There are diminishing returns on increasing the spin exchange rate by increasing the rubidium density, since for fixed laser intensity, the volume of Rb which can be polarized eventually decreases. As before, various processes will act to depolarize the ^{3}He atoms. Collisions between ^{3}He atoms can cause the exchange of nuclear spin and orbital angular momentum. This bulk relaxation rate, $\Gamma_{bulk} \equiv 1/\tau_{bulk} \approx 1/1000$ hours. Paramagnetic impurities, both gaseous and embedded in the cell walls contribute further to the overall relation of the cell,

$$\frac{1}{\tau_{cell}} = \frac{1}{\tau_{bulk}} + \frac{1}{\tau_{gas}} + \frac{1}{\tau_{wall}}. \tag{2.10}$$

Factors external to the cell also play a role. Polarized ^{3}He diffusing through regions in which the holding field is inhomogeneous will precess about the local field and the spin direction will be randomized. By keeping the gradients perpendicular to the alignment field small, <20 mG/cm, this relaxation effect became insignificant for us, $\tau_{\nabla B} > 500$ hours.

A final contribution results from the effects of ion production in the cell by the electron beam [71, 72]. The beam will produce ^{3}He$^+$ and 3He$_2^+$ ions at a rate

$$\Gamma_{ion} \approx \frac{\Delta E_{ionization}}{\text{ionization energy}} \frac{\text{electrons}}{\text{second}} \approx 7 \times 10^{-20} \frac{\text{electrons}}{\text{second}} \tag{2.11}$$

in our cells, where ΔE is the energy lost by ionization of an electron traversing the target, and the ionization energy has been taken as 42 eV [73]. Each ion will depolarize an average of n ^{3}He atoms, before being neutralized, by coupling the nuclear to the unpaired electron spin, or to the rotational angular momentum in the case of the molecular ion, yielding $\Gamma_{beam} = n\Gamma_{ion}$. At the high densities in our target n is < 1 [71, 74, 72], and for our highest beam currents of 2×10^{11} electrons/spill at 120 Hz, $\tau_{beam} = 1/\Gamma_{beam} > 170$ hours. Magnetic field gradients created by the beam will contribute even less than this to the depolarization of the cell [72]. The

cumulative effect of these relaxation processes can be characterized by

$$\Gamma_R = \frac{1}{\tau_{\text{cell}}} + \frac{1}{\tau_{\nabla \mathbf{B}}} + \frac{1}{\tau_{\text{beam}}} \approx \frac{1}{58 \pm 5\text{hours}}. \tag{2.12}$$

We note that since the diffusion time in these cells is of the order of seconds, if there were large unforeseen relaxation effects due to the beam, the cells would have depolarized quickly, which was not observed.

A simple model of the spin exchange and relaxation processes yields a time dependent polarization of ^{3}He given by

$$P_{^3\text{He}}(t) = \frac{\gamma_{\text{SE}}}{\gamma_{\text{SE}} + \Gamma_R} P_{\text{Rb}}(1 - \exp(-(\gamma_{\text{SE}} + \Gamma_R)t)) \tag{2.13}$$

where $P_{^3\text{He}}(0) = 0$ and P_{Rb} is the steady state polarization of Rb $\approx 100\%$. Given our Γ_R and γ_{SE} estimates, $P_{^3\text{He}}(t \rightarrow \infty) \approx 35\%$ which is close to the observed average polarization of 33% over the entire experiment.

2.4.2 Target Apparatus

The target was made of Corning 1720 aluminosilicate glass, which has low ^{3}He permeability. It used an innovative two chamber design where the upper, pumping cell was a 70 cm^3 volume containing ^{3}He and a few tens of mg of Rb. This chamber was enclosed in a plastic oven and heated to 160-165 C to create a Rb vapor density of about 2×10^{14} atoms/cm^3. A laser hut was constructed adjacent to the target to contain Five Spectra Physics Model 240 Beam Loc argon ion lasers each pumping one of five Spectra Physics Model 3900S Ti:Sapphire lasers. The lasers pumped the target continuously, resulting in a total of 20 watts of power at 795 nm on the pumping cell. The light from each laser passed through various optical components including a $\lambda/4$ plate to produce circularly polarized light, before reaching the pumping cell which was about 3 m away. The system was quite stable and required retuning only after several days. A schematic of the target is shown in Figure 2.10. Our discussion before suggests that high polarized Rb densities will yield large γ_{SE} and hence high $P_{^3\text{He}}$. With 20 watts of power we could have operated the pumping cell at 180 C but the Nylotron plastic oven began to leak at these temperatures (we had three oven failures) so we ran suboptimally at the lower Rb density found at 160-165 C. Due to

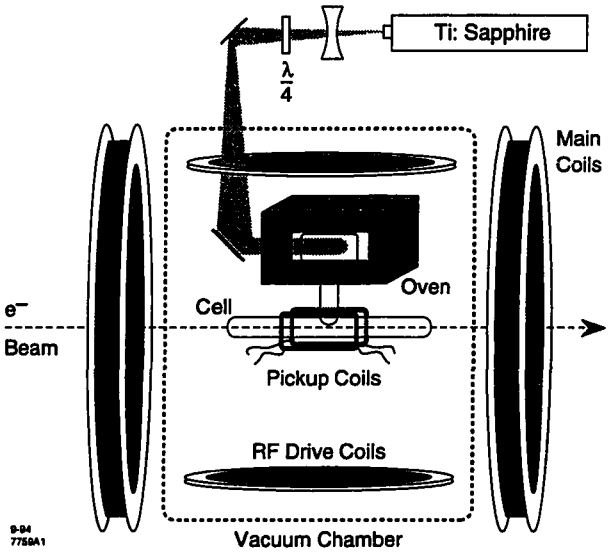

Figure 2.10: Schematic of the E142 ^{3}He target

the problems with the ovens, three separate target cells were used, known affectionately as Minnehaha, Hiawatha and Gore. The characteristics of these cells were very similar (Exact dimensions are given in the Dilution Factor section 3.6.6).

The polarized ^{3}He polarized in the upper cell diffused through a 60 mm long by 9 mm inner diameter transfer tube to the lower, target cell, with a time constant of about 10 minutes. This cell was a cylinder 30 cm long, 1 cm in radius, with 0.1 mm thick endcaps which were roughly spherical. Jets of ^{4}He were directed at these endcaps to ease the thermal stress caused by the beam. Endcap temperatures were monitored with a pyrometer, and the rest of the target cell with 6 Resistive Thermal Devices (RTDs). The target cell remained at 65±7 C and had a residual Rb density of the order 10^{11} atoms/cm^3, which is insignificant in comparison to the 2.3×10^{20} atoms/cm^3 of ^{3}He and the 1.8×10^{18} molecules/cm^3 of N_2 which were the primary components of the target cell. A large scattering chamber enclosed the oven and two chamber cell assembly, and was evacuated to a few mtorr.

Outside of the scattering chamber was a set of 1.4 m diameter Helmholtz coils which produced a 29 G field to align the ^{3}He nuclear spins. Smaller secondary coils were added to allow polarizations transverse to the beam, and to facilitate the reversal

of the target spin along the beam direction.

Another feature of the apparatus was the stepper which moved the target. By moving the cell through the beamline and leaving it where the event rate was a minimum, we maximized the fraction the events coming from ^{3}He. The target could be removed and reinserted to the same position with submillimeter accuracy. The stepper was also used to move an empty reference cell into the beamline which we filled with known pressures of ^{3}He for systematic studies (see the section on the Dilution Factor 3.6.6).

2.4.3 Target Polarimetry and Polarization Results

The ^{3}He polarization was determined by adiabatic fast passage NMR [66]. A set of 45.72 cm diameter Helmholtz drive coils above and below the target (distinct from the longitudinal and transverse holding field coils) provided a 100 mG RF field at 92 kHz, while the main holding field was swept from 19 G to 39 G, through the Larmor resonance at 29 G. The field sweep rate of 1.27 G/s arose from the conditions that the sweep rate be slow enough for the nuclear spins to follow the changing field, but fast enough to avoid the spins dephasing while passing through the resonance. The resulting nuclear spin flip induced a signal in a set of 200 turn copper pickup coils, wound on a 76.2 mm by 25.4 mm teflon form and centered around the target cell. These coils had their long axis parallel to the target, and were separated from each other by 25.4 mm. Using a 100 pF capacitor, an LC resonant circuit was formed, with the resonance at 100 kHz. From here a Stanford Research Systems SRS560 preamplifier, located close to the target, amplified the signal and sent it to the Counting House. In Figure 2.11 we show the layout of the target electronics. A Stanford Research Systems SRS530 lock-in amplifier subtracted the 92 kHz modulation, and the resulting NMR signal was proportional to the ^{3}He polarization. The proportionality constant is determined from the thermal equilibrium Boltzmann polarization of protons in a water sample. This polarization is calculated from

$$P_p = \tanh\left(\frac{\mu_p \cdot \mathbf{B}}{k_B T}\right) \tag{2.14}$$

where $|\mathbf{B}|$ is 21.61 G for a proton resonance at 92 kHz. The proton signals were small compared to the ^{3}He signals (few μV versus 200 mV), but large enough that there

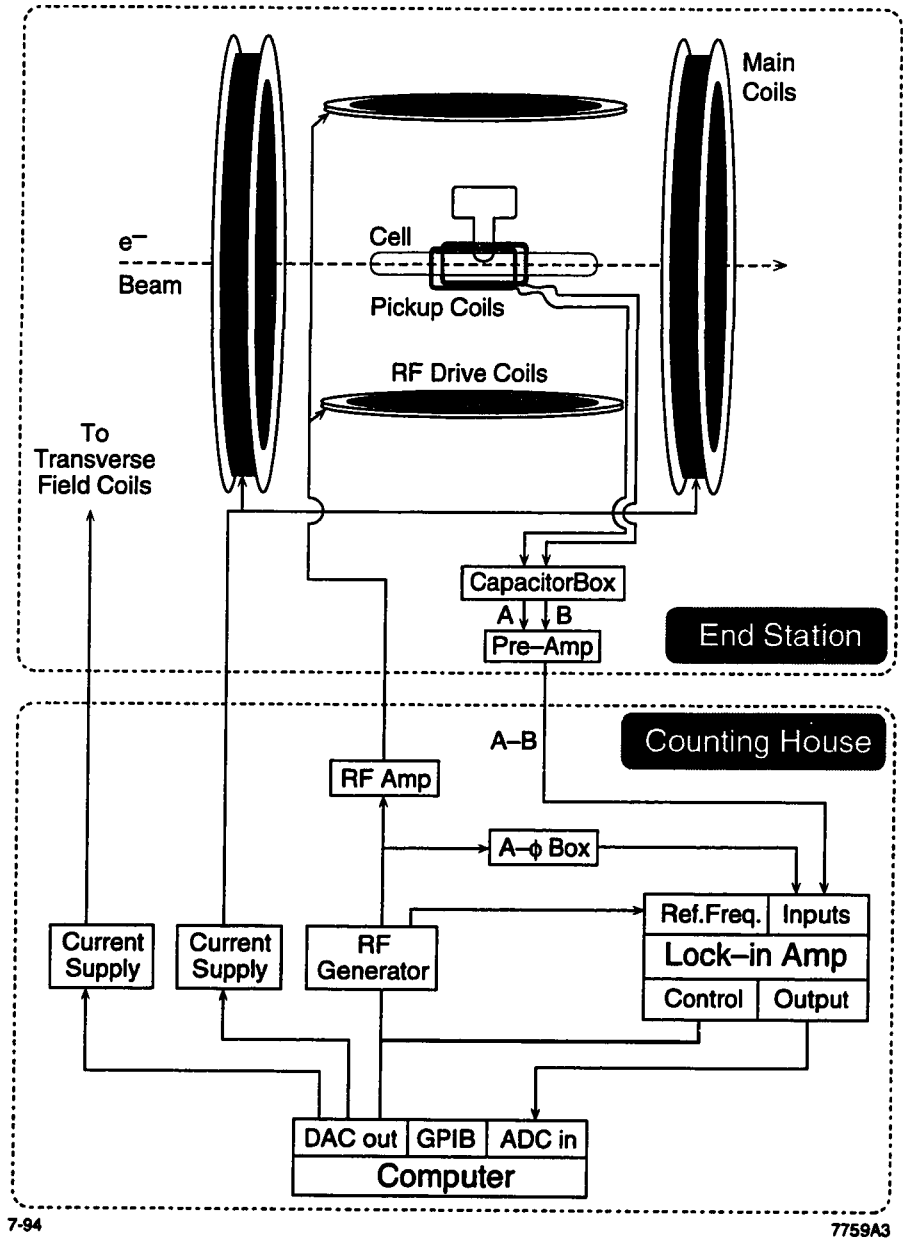

Figure 2.11: Schematic of the NMR electronics used to determine ^{3}He polariation in the E142 target.

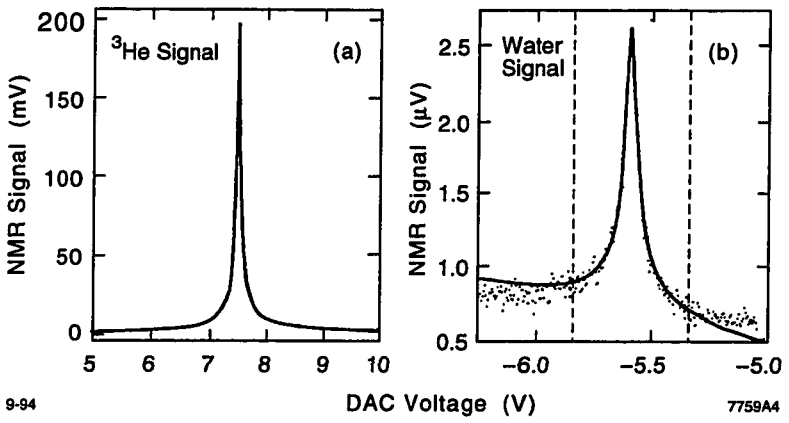

Figure 2.12: In the plot on the right we show the average of 25 proton NMR-AFP signals, which are used to calibrate the polarization of the much larger ^{3}He signals seen on the left.

was no need to incur the greater costs of higher fields and frequencies needed for a larger proton signal. These signals can be related to ^{3}He polarization if the number densities and cell radii, R, of the water cell and ^{3}He cell are known, via

$$\frac{P_{^3\mathrm{He}}}{S_{^3\mathrm{He}}} = \frac{P_p \mu_p}{S_p \mu_{\mathrm{He}}} \frac{[p]}{[^3\mathrm{He}]} \left(\frac{R_p}{R_{\mathrm{He}}} \right)^2 \tag{2.15}$$

where S is the signal size. The proton signal was determined by averaging and fitting about 200 sweeps taken before E142, and 100 taken afterwards. From this data, the calibration factor for the ^{3}He signal was determined to be 15.07±1.07% polarization per 100 mV signal. Examples of a proton and ^{3}He NMR signal are shown in Figure 2.12. The dominant errors contributing to this 7.1% uncertainty in ^{3}He polarization are from a 5.6% uncertainty in the proton signal size (resulting from uncertainty in the background noise under the resonance signal), a 1.5% error in our knowledge of the thermal equilibrium polarization of the protons, a 2.6% error from uncertainty in the target cell radius[2], and a 2.5% error in the number density of ^{3}He. Since the proton and ^{3}He measurements were taken at different temperatures, the resonance circuitry behaves differently (since the resistance of the coils will change, so the Q of the circuit will change). The error from correcting for these effects, and due the uncertainty in the water cell radius and proton number density adds another

Source of Uncertainty	Contribution
Proton signal size	5.6%
Proton thermal equilibrium polarization	1.5%
Cell radii[2]	2.6%
Number density of ^{3}He	2.5%
Temperature effects on NMR circuitry	1.9%
Total Systematic Error	7.1%

Table 2.2: Sources of systematic error in determining the target polarization.

1.9%. In fact, individual calibration constants were used for each of the three targets employed during the experiment. These constants were different primarily because the ^{3}He number density varied by a few percent between the cells.

We note that since the diffusion times are of the order of seconds, measuring the polarization at the center of the cell is a measure of the polarization throughout the entire cell.

Over the course of the experiment the target performed very well, with an average polarization of about 33%. The plot in Figure 2.13 shows both the polarization and helicity of the target for the data runs used to extract the spin structure function.

2.4.4 ^{3}He Polarization Direction

The ^{3}He polarization direction was determined in two ways [66]. Liquid crystal circular polarizers determined the laser helicity, which determines the angular momentum transferred to the ^{3}He nuclei, and hence the polarization direction. A second method uses the sign of the NMR signals. Protons and ^{3}He have magnetic moments of opposite sign, so if their spins are in the same direction initially and are swept through a resonance with $d|\mathbf{B}|/dt$ of the same sign, the NMR resonance signals will be of opposite sign. This determines the ^{3}He's polarization direction with respect to the proton's, which statistical mechanics suggests is preferentially aligned parallel to the external field. So, by measuring the magnetic field direction with a gaussmeter, fluxgate magnetometer and finally from knowledge of the current direction in the Helmholtz coils (all three results were consistent) we determined the polarization

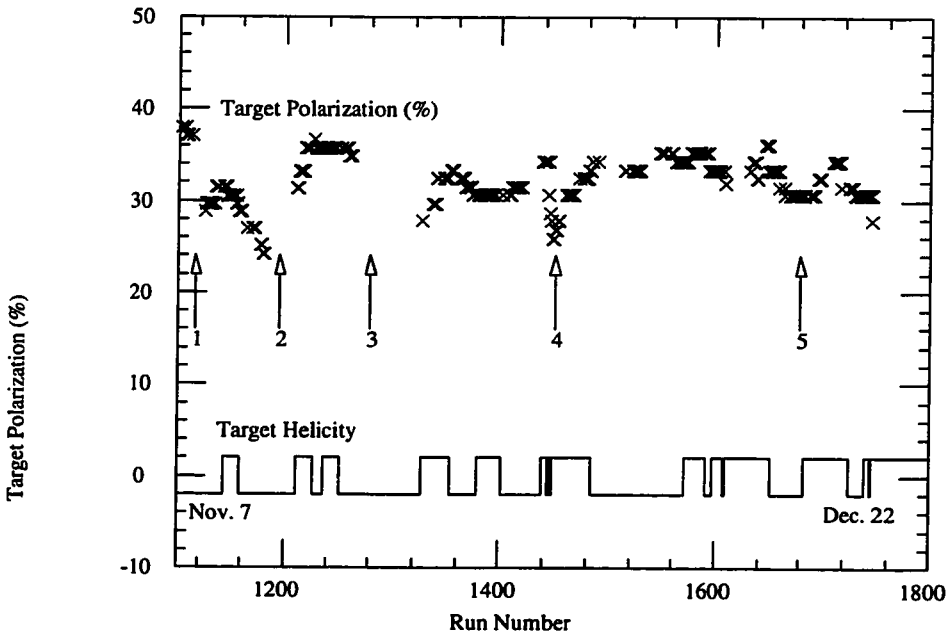

Figure 2.13: The target polarization and helicity are plotted for the data runs used in the asymmetry analysis. The first arrow indicates the occurrence of a leak in the target oven, the second of a migration of the rubidium into the transfer tube, both necessitating changes of the target cell. The third arrow indicates the onset of a leak in one of the cells. The fourth arrow points to the drop in polarization which occurred when we ran the target with transverse polarization - a configuration in which the cell could not be pumped. Finally, there was a small decrease in polarization observable in the final set of runs at beam energies of 25.5 GeV due to the increased ionization in the target caused by the higher beam currents used.

direction of the protons and of ^{3}He.

2.5 Magnetic Spectrometers and Detectors

E142 used two independent magnetic spectrometers at 4.5° and 7.0° to detect the electrons scattered from the target. Two spectrometers were used simply to increase the statistical precision of our measurement; they were not used in coincidence.

The magnets directed charged particles with a restricted range of momenta into our detector huts. Inside the detector huts were three types of detectors which were used to detect the electrons and determine their energy. The detector layout in each spectrometer arm was identical, and consisted of a 2.2 m long gas threshold Čerenkov detector operating at a pion threshold of 9 GeV/c, followed by three planes of scintillator hodoscopes. Downstream from the hodoscopes was a second, 4.2 m Čerenkov detector operating at a pion threshold of 13.0 GeV/c, followed by another three planes of hodoscopes. Two planes of lucite each equipped with two phototubes and covering the entire acceptance followed the hodoscopes. The last element in the detector package was a total absorbing lead glass calorimeter. A schematic of the spectrometer and detector package is shown in Figure 2.14

The philosophy behind the detector set up is straightforward. Electrons passing through the magnets and entering the detector huts will produce signals in both Cerenkov detectors, and fire some of the fingers of the hodoscopes. When the electron hits the lead glass counter it produces an electromagnetic shower and is totally absorbed. Thus whenever there is a triple coincidence of activity in the two Čerenkovs and shower counter it is a good sign that an electron is present. This triple coincidence, called the Main Trigger, is used to gate the rest of the electronics so we can record the energy of the electron from the shower counter, and its momenta from the track left in the hodoscopes.

The principle background in the experiment were pions. These would not cause a Main Trigger triple coincidence since their momenta was usually below the 13 GeV/c threshold of the second Čerenkov, and so would never fire this detector.

Before giving a more detailed description of the spectrometer elements, we describe the coordinate system used. Each spectrometer has it own right hand coordinate

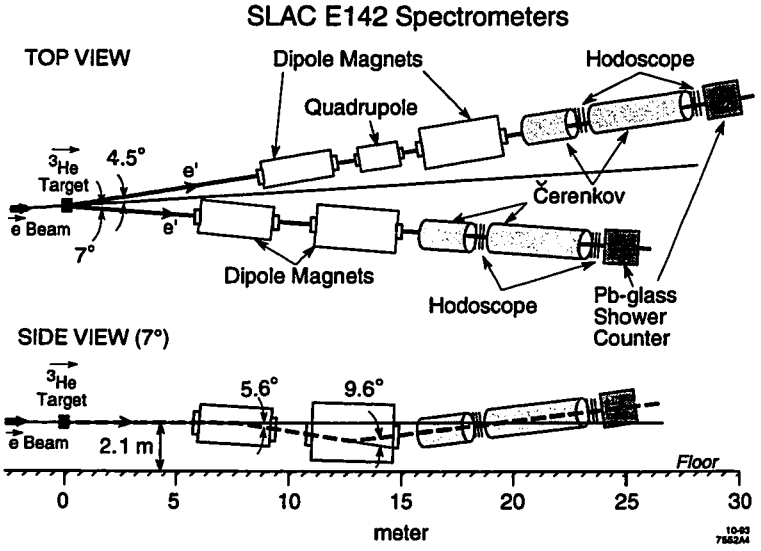

Figure 2.14: The layout of the magnets and detectors used in E142 is shown in this plot (the lucite counters are not shown).

system, with the origin being the center of the ^{3}He target. The line along 4.5° (or 7.0°) is taken to be the $\hat{z}$ direction. The horizontal line perpendicular to the $\hat{z}$ direction defines the $\hat{x}$ direction, and $\hat{y}$ is in the vertical direction. The spectrometer dipoles bend the particles in the vertical direction, defining the bend plane. Angles in the bend plane are denoted by ϕ. The non-bend plane is parallel to the ground, and angles in this plane are denoted by θ. The coordinates are illustrated in Figure 2.15.

To cover a range in Bjorken x from 0.03 to 0.6, our momentum acceptance had to extend from 6 to 18 GeV/c with a large solid angle to ensure a reasonable event rate. A second design consideration was to have enough bends in the system to prevent the large photon background from bremsstrahlung, radiative Møller and π^0 decay from entering our detectors. Finally, we required the system to have sufficient momentum resolution to determine x to $\sim$ 10%. The spectrometer system developed to achieve these aims has been described by Petratos *et al.* [97].

The solution adopted to the constraints listed above involved a novel reverse bend design in which two dipoles bent the scattered electrons first downwards and then

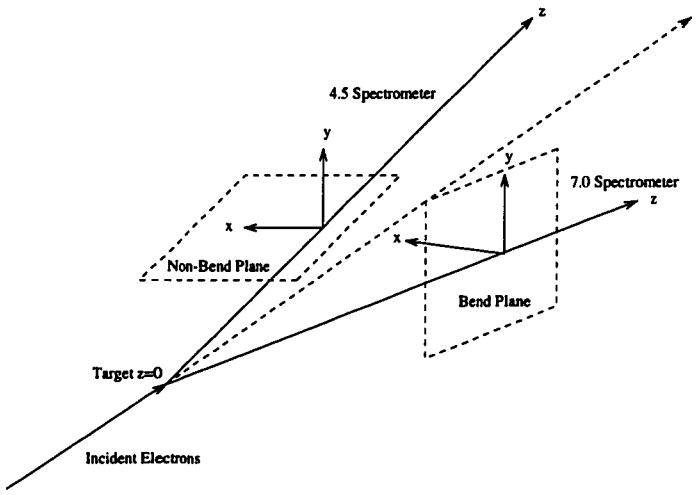

Figure 2.15: The coordinate system used to describe the spectrometer elements is shown.

upwards. This configuration increased the solid angle compared to more conventional designs, and ensured that photons could only reach the detectors after having bounced twice in the magnets' interiors[3]. The 4.5° was further equipped with a quadrupole between the two large dipoles. This served the dual purposes of increasing the spread of particles (reducing the possibility of overlapping events) in the nominally non-bend plane (particles were defocussed in $\hat{x}$) while introducing a momentum dependent correlation between position and divergence (focusing in $\hat{y}$) which improved the momentum resolution. A third advantage afforded by this system came about because the increased separation of the dipoles almost created a three bounce system [97].

The final momentum bite, $d=(p-p_c)/p_c$ for momentum p and central momentum p_c, ranged from d_{min}=-0.45 to $d_{max} \sim 0.55$. The large range of particle momenta accepted allowed us to collect data over a large range in Bjorken x. The angular range at the target of particles making it through the magnets is given in Table 2.3, as well as the peak solid angle. In Figures 2.16 & 2.17 we show the solid angles of the two spectrometers versus momentum, with the acceptance from a few other experiments for comparison. The magnet parameters and settings used for the majority of the

[3]In fact this was not fully achieved in the 7.0° spectrometer where part of our detectors were illuminated by photons which had bounced only once in the magnets.

Acceptance (mrads)	$\theta_{\min}$	$\theta_{\max}$	$\phi_{\min}$	$\phi_{\max}$	$d\Omega_{\max}(sr)$
4.5° Spectrometer	-7.6	+7.6	-20	20	0.097
7.0° Spectrometer	-14	+14	-20	15	0.435

Table 2.3: Spectrometer acceptance limits

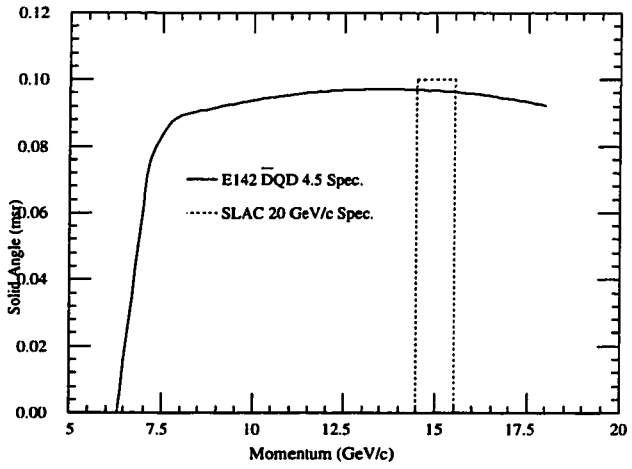

Figure 2.16: The acceptance of the 4.5° spectrometer system is shown, along with that of the SLAC 20 GeV spectrometer for comparison. The large gain in momentum acceptance compared to previous designs allowed us to detect events with a large range in Bjorken x.

22.66 GeV/c runs are given in Table 2.4. The stability of the magnetic fields was monitored throughout the experiment with a set of NMR probes in the dipoles, and a Hall probe in the quadrupole. By regulating the current, the magnetic fields were kept stable to about 0.1%. The specifics of the magnetic field measurements have been described by Dunne [76].

The trajectories of the electrons in the bend plane as they pass through the spectrometer magnets are shown in Figures 2.18 & 2.19. In the 7.0° we see that at the shower counter the divergence of the particles is strongly related to their momentum, but that their position is only weakly coupled. Conversely, in the 4.5°, position is

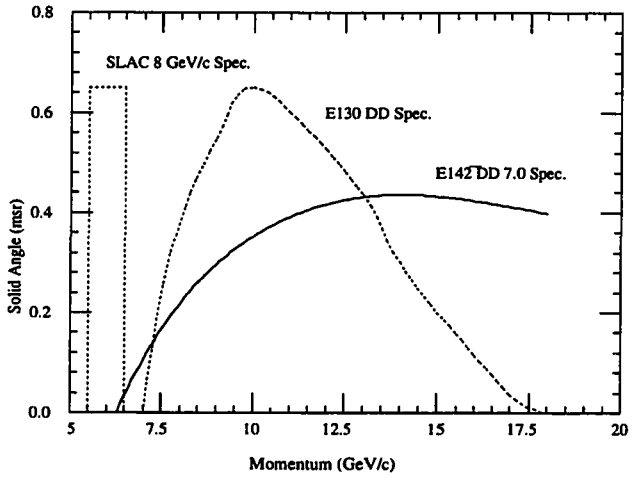

Figure 2.17: The acceptance of the E142 7.0° is shown to cover a large momentum range in comparison with previous spectrometer configurations.

	4.5° Spectrometer			7.0° Spectrometer	
Parameter	B 204	Q 203	B82	B 202	B 81
Length (m)	2.997	1.3385	3.454	2.997	3.454
Gap (m) ($\hat{x}$)	0.1803	0.1937	0.3505	0.3759	0.3505
Width (m) ($\hat{y}$)	0.3150	0.1937	0.5588	0.3150	0.5588
Bend Angle (degrees)	-5.6	—	+9.6	-5.6	+9.6
Radius of curvature (m)	30.678	—	20.643	30.678	20.643
$\int \mathbf{B} \cdot d\mathbf{l}$ (kGauss · m)	37.477	43.1	64.190	40.735	69.968
Current (amps)	1334.4	1335.8	1942.5	1424.3	2152.1

Table 2.4: Magnet operating parameters for a central momentum of 11.5 GeV/c in the 4.5° spectrometer and 12.5 GeV/c in the 7.0° spectrometer.

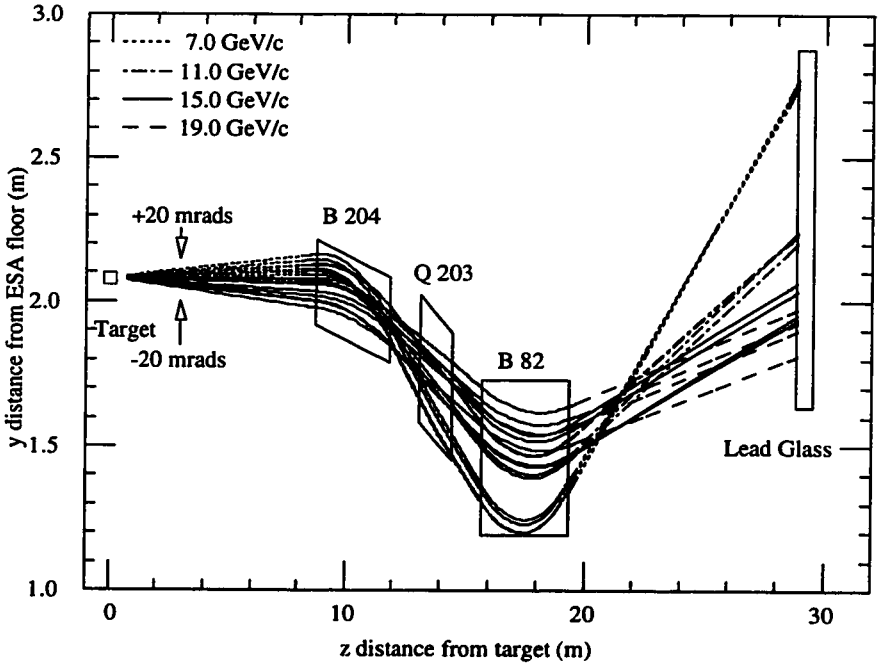

Figure 2.18: Particle trajectories in the bend plane of the 4.5° for a central momentum setting of 11.5 GeV/c.

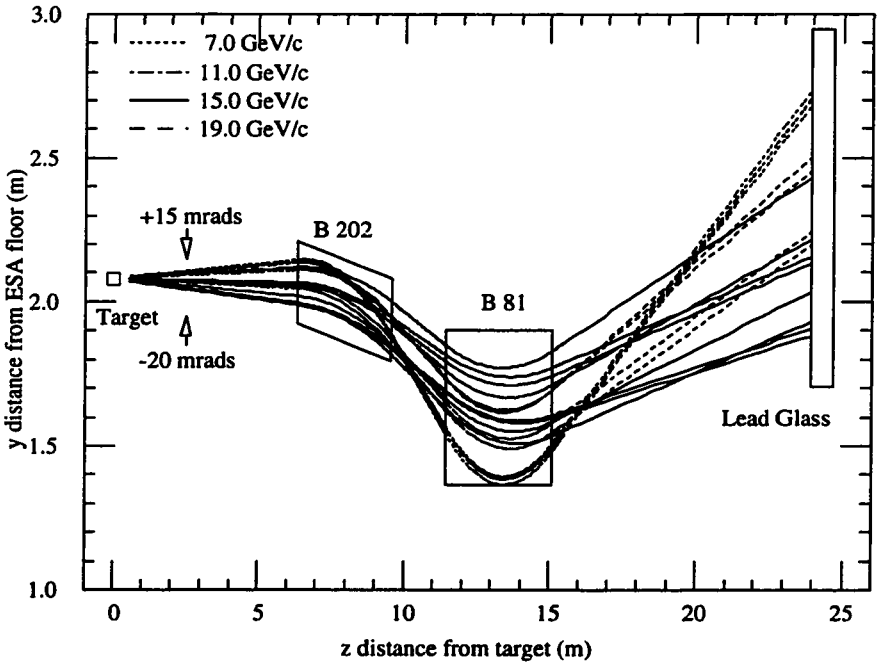

Figure 2.19: Particle trajectories in the bend plane of the 7.0° for a central momentum setting of 12.5 GeV/c.

also correlated with momentum which improved our resolution.

2.6 Čerenkov Detectors

Performing the asymmetry measurement required us to identify the scattered electrons from the pions and other debris created in the collisions at the target. The lead glass array and Čerenkov detectors were the principal tools used for electron identification and pion rejection. The π/e ratio varied from about 10 at 7 GeV/c to about 0.2 at 13 GeV/c, so a single N_2 threshold Čerenkov counter operating at a 13.0 GeV/c threshold would be sufficient for us. Second detectors operating in coincidence at 9.0 GeV/c thresholds were used to add redundancy and cleanliness to our electron trigger, as well as for systematics studies. The four Čerenkov tanks all worked under the same mechanism; electrons passing through the detectors produced Čerenkov radiation which was reflected by mirrors to a photomultiplier tube coated with wavelength shifter located outside of the path of the electrons.

2.6.1 Detector Design

The pion threshold, P_π, determines the index of refraction, n, of the gas in the counter through the relations

$$\cos\theta_e = \frac{1}{n\beta_e} < \frac{1}{n\beta_\pi} = \cos\theta_\pi = 1$$

where θ is the angle of emission of Čerenkov photons with respect to the trajectory of the charged particle of velocity β. We can rewrite this as

$$n = \sqrt{1 + \left[\frac{m_\pi}{P_\pi}\right]^2}. \tag{2.16}$$

For a 9.0 GeV/c pion threshold $(n-1) = 1.202\times10^{-4}$, and for a pion threshold P_π=13.0 we find $(n-1) = 5.763\times10^{-5}$. In both cases it is easiest to achieve these indices of refraction using a gaseous radiator. We chose to use nitrogen because of its excellent transmission of Čerenkov radiation from 150 nm to 700 nm, its low δ production rate, tolerable scintillation rate, and because it was readily available at

also correlated with momentum which improved our resolution.

2.6 Čerenkov Detectors

Performing the asymmetry measurement required us to identify the scattered electrons from the pions and other debris created in the collisions at the target. The lead glass array and Čerenkov detectors were the principal tools used for electron identification and pion rejection. The π/e ratio varied from about 10 at 7 GeV/c to about 0.2 at 13 GeV/c, so a single N_2 threshold Čerenkov counter operating at a 13.0 GeV/c threshold would be sufficient for us. Second detectors operating in coincidence at 9.0 GeV/c thresholds were used to add redundancy and cleanliness to our electron trigger, as well as for systematics studies. The four Čerenkov tanks all worked under the same mechanism; electrons passing through the detectors produced Čerenkov radiation which was reflected by mirrors to a photomultiplier tube coated with wavelength shifter located outside of the path of the electrons.

2.6.1 Detector Design

The pion threshold, P_π, determines the index of refraction, n, of the gas in the counter through the relations

$$\cos\theta_e = \frac{1}{n\beta_e} < \frac{1}{n\beta_\pi} = \cos\theta_\pi = 1$$

where θ is the angle of emission of Čerenkov photons with respect to the trajectory of the charged particle of velocity β. We can rewrite this as

$$n = \sqrt{1 + \left[\frac{m_\pi}{P_\pi}\right]^2}. \tag{2.16}$$

For a 9.0 GeV/c pion threshold $(n-1) = 1.202\times10^{-4}$, and for a pion threshold P_π=13.0 we find $(n-1) = 5.763\times10^{-5}$. In both cases it is easiest to achieve these indices of refraction using a gaseous radiator. We chose to use nitrogen because of its excellent transmission of Čerenkov radiation from 150 nm to 700 nm, its low δ production rate, tolerable scintillation rate, and because it was readily available at

	4.5° Spectrometer		7.0° Spectrometer	
Parameter	C1	C2	C1	C2
Interior Length	225 cm	422 cm	219 cm	422 cm
Interior Radius	52.7 cm	80 cm	52.7 cm	80 cm
Window Thickness	0.15 cm	0.1 cm	0.15 cm	0.1 cm
Effective Length	200 cm	400 cm	200 cm	400 cm
No. of Mirrors	2	3	2	3
Mirror Size ($\hat{x} \times \hat{y}$)	51 × 39 cm^2	71 × 44 cm^2	51 × 39 cm^2	71 × 44 cm^2
Radii of Curvature	120 cm	163 cm	120 cm	163 cm
Active Area	44 × 44 cm^2	60 × 107 cm^2	44 × 53 cm^2	59 × 99 cm^2
Pion Threshold	9.0 GeV/c	13.0 GeV/c	9.0 GeV/c	13.0 GeV/c
N_2 Pressure (22°C)	6.24 psia	2.99 psia	6.24 psia	2.99 psia

Table 2.5: The Čerenkov detector dimensions are given in this table.

extremely high purity. Since the amount of Čerenkov light produced by the passage of an electron is roughly proportional to the detector length (we must also consider absorption) we made the tanks as long as could be accommodated in the detector huts. Each detector was made of an aluminum cylinder with 1.27 cm thick side walls, and very thin end windows. The interiors were treated with a mild acid etch and steam-cleaned to remove the aluminum oxide and other surface contaminants, as part of a general effort to keep the devices clean. We list the dimensions and other parameters in Table 2.6.1, where for convenience we have called the 2 m long 9.0 GeV/c threshold tanks "C1" and the 4 m long 13.0 GeV/c tanks "C2". The two end windows of the C2 tanks deserve special mention. Normally in vacuum vessels one uses windows 1/1000″ thick for every inch in diameter, which would have meant using 1.5 mm thick windows for a tank this size. However, by hydroforming a disk of 2024-T3 aluminum at 30 psi, the stress was reduced on the window and it could be made 1 mm thick instead, without compromising safety, and reducing problems due to δ production and multiple scattering.

The envelope of Čerenkov radiation expected in the detectors was too large to be covered easily with a single mirror, so two spherical mirrors were used in each 2 m tank, and three spherical mirrors in the 4 m tanks. All of the mirrors were kindly

Characteristic	Hamamatsu R1584-01
Spectral Response	200 nm - 640 nm
Peak Quantum Efficiency	21% at 370 nm
Photocathode	Bialkali, 120 mm useful diameter
Dynode Structure	14 stages, linear focused
Operating Voltage	-2500 V
Anode Pulse Risetime	2.2 ns
Transit Time Spread	1.2 ns
Gain	$\approx 3\times10^7$

Table 2.6: Properties of Hamamatsu R1584-01 PMTs

manufactured for us at CERN by slumping a 3 mm thick 836 mm diameter disk of float glass into a stainless steel mold [78]. The glass was cut, cleaned, then coated with 80 nm of Al followed by a protective coating of 30 nm MgF_2 (which is transparent down to 115 nm [79]). Measurements of the reflectivities of our ten mirrors yielded an average of 80% at 160 nm and 89% at 200 nm. Image sizes at the focal point were estimated to be $\leq$3 mm in diameter. The mirrors were held at the sides by aluminum clamps cut to the curvature of the mirrors. The clamps squeezed pieces of tubing around the edges of the mirror and held them rigidly. In turn, the clamps were held in an aluminum frame mounted 19 cm upstream of the downstream end window. A schematic of one of the 4 m tanks is presented in Figure 2.20.

Mirror positions were optimized to focus all of the light onto a single 5″ photomultiplier tube, without the use of a Winston cone. Such a configuration maximized the signal/noise in our detectors. Hamamatsu 5″ R1584-01 UV glass photomultiplier tubes (PMTs), specially selected by the manufacturer for high quantum efficiency were used. Some characteristics of these PMTs are given in Table 2.6. The magnetic shielding provided by Hamamatsu was supplemented with an additional layer of Permendur to reduce the losses caused by the fringe fields of the dipole magnets (primarily a concern for C1 in the 7.0° where the fields were close to 10 G). In addition, the C1 tanks were wrapped with a few layers of Permendur to reduce the fringe fields of the dipoles in the tanks.

To capture the abundance of Čerenkov photons in the UV, we coated our tubes

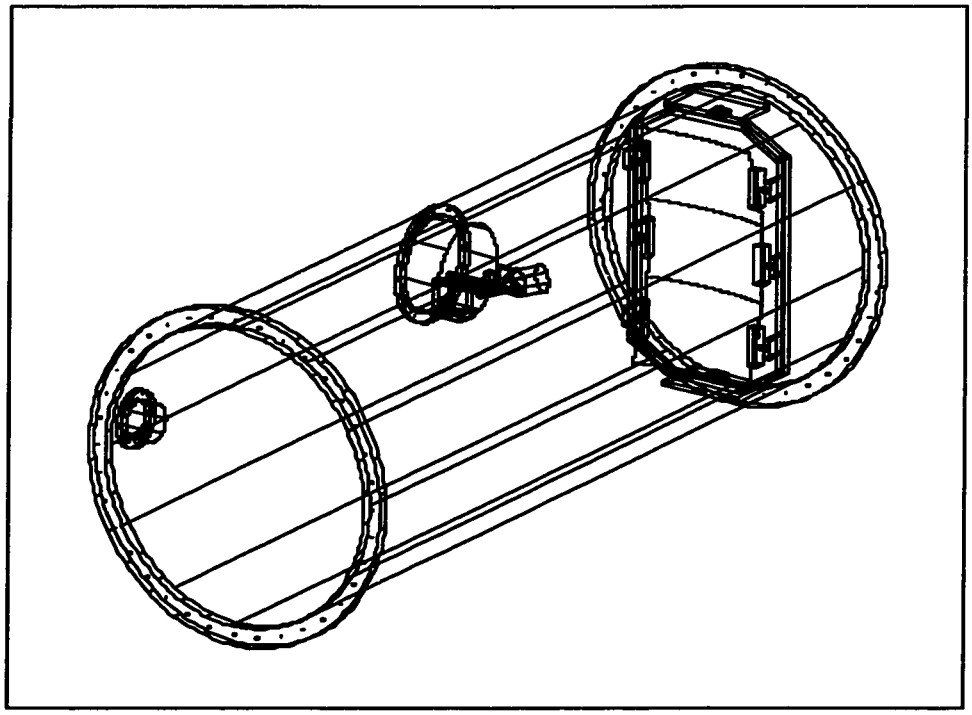

Figure 2.20: The layout of one of the 4 m Čerenkov tanks is shown here. The electrons enter from the left and produce Čerenkov radiation which is reflected by the three mirrors at the end of the tank onto the phototube at the side.

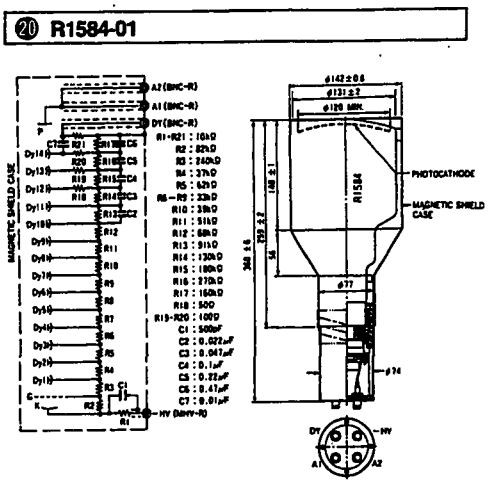

Figure 2.21: The resistor chain and dimensions of the 5″ phototubes used in our Čerenkov detectors are shown here.

with 2430 nm (0.3 mg/cm^2) of p-terphenyl wavelength shifter, followed by a protective coating of 25 nm of MgF_2 [81]. Film thicknesses were controlled during the vacuum deposition with a crystal thickness monitor. The fluorescence maximum of p-terphenyl is about 370 nm [80] which is well matched to the region of high quantum efficiency of our PMTs. Also, the short 1-2 ns decay time of this emission [80] enabled us to retain accurate timing information from the Čerenkovs. This was crucial for forming our trigger and for subtracting the pion background.

In advance of E142 a test of one of the 2 m tanks was undertaken at Brookhaven National Laboratory. From a comparison of coated versus uncoated tubes we concluded that the use of p-terphenyl on our PMTs resulted in a gain of $\approx 90\%$ in the number of photoelectrons produced. To exploit fully this gain, the gas used in the tanks must have high transmission in the UV to ensure a large flux photons for conversion. The use of gases such as O_2 or CO_2 then becomes inappropriate because of their strong absorption of photons with wavelengths smaller than 190 nm. N_2 is a good radiator because its transmission extends down to 150 nm.

2.6.2 Predicted Čerenkov Response to Electrons

The number of photoelectrons, N_{pe}, produced in our counters due to Čerenkov radiation can be estimated from

$$N_{pe} = \epsilon 2\pi\alpha L_{\rm eff} \int\int_{\beta_e n(\lambda)>1} \left[1 - \frac{1}{\beta_e^2 n^2}\right] \frac{R(\lambda)}{\lambda^2} \exp\left[-\sigma(\lambda)\frac{\rho L_\gamma N_{AV}}{A}\right] C(\lambda,\lambda') QE(\lambda') d\lambda d\lambda' \tag{2.17}$$

where $\sigma(\lambda)$ is the absorption cross section of N_2, N_{AV} is Avogadro's number, A is the molecular mass of N_2, $n(\lambda)$ is the index of refraction, ρ is the gas density, $L_{\rm eff}$ is the effective length of the detector (200 or 400 cm), L_γ is the average path length of a Čerenkov photon, $QE(\lambda)$ is the quantum efficiency of out PMT, and $R(\lambda)$ is the mirror reflectivity. The effect of the wavelength shifter is accounted for by the function $C(\lambda,\lambda')$. P-terphenyl will absorb photons ranging from 115 nm to 310 nm and re-emit them around $\lambda_r \approx 370$ nm with $\sigma_r \approx 30$ nm [80]. The quantum efficiency for this process, ϵ_r, is around 85% [83] and for thicknesses > 1000 nm is roughly wavelength independent [82]. Above 310 nm the conversion efficiency drops off rapidly [82], and above 350 nm the incident photons pass through the wavelength shifter unconverted with a small absorption loss estimated to be less than 6% [80]. Thus $C(\lambda,\lambda')$ takes the very approximate form :

$$\begin{aligned} C(\lambda,\lambda') &= \frac{\epsilon_r \epsilon_g}{\sqrt{2\pi}\sigma_r} \exp\left[-\frac{1}{2}\left(\frac{\lambda-\lambda'}{\sigma_r}\right)^2\right], \text{for } \lambda \in [110\text{nm}, 310\text{nm}] \\ &= 0.95\ \delta_{\lambda\lambda'} \qquad\qquad \text{for } \lambda \in [310\text{nm}, 640\text{nm}]. \end{aligned} \tag{2.18}$$

Here ϵ_g is a geometrical factor reflecting the fact that the re-emission is isotropic, so naively we expect $\epsilon_g = 0.5$. However, total internal reflection can occur at the N_2/p-terphenyl boundary. Only scintillation photons emitted back towards the N_2 with $\theta < \theta_{\rm critical} \approx 45°$ will be lost directly. This is a fraction $\frac{1}{2}(1-\cos\theta_{\rm critical}) \approx 15\%$ of the total solid angle. The remaining photons either pass to the photocathode or bounce in the wavelength shifter towards the photocathode. A similar situation occurs at the interface between the PMT glass and the photocathode (where n $\approx$ 3). Because of this potential for the Čerenkov photons to interact multiple times with the photocathode, the effective quantum efficiency is enhanced and ϵ_g lies somewhere between 0.55 and 0.75 [79]. The factor ϵ in front of (2.17) reflects inefficiencies such as absorption in the

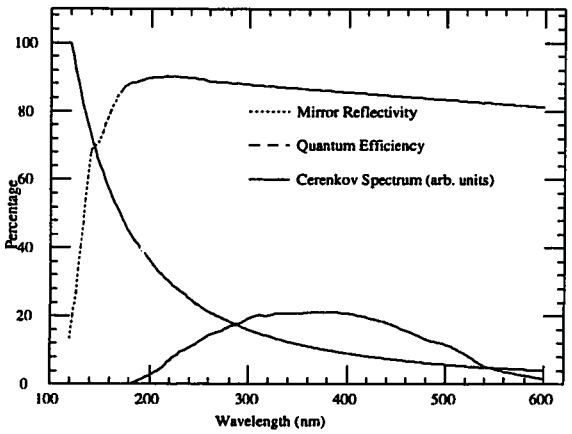

Figure 2.22: The mirror reflectivity and phototube quantum efficiency are plotted with the spectrum of Čerenkov radiation. High reflectivity and quantum efficiency are desirable at low wavelengths where the bulk of the Čerenkov photons are produced.

PMT glass and losses during photoelectron transit from the photocathode to the first and subsequent dynodes (this latter inefficiency is not quoted as part of the quantum efficiency of the tube). Estimates of ϵ vary, but it is seldom ever greater than 0.7, and often 0.5 or less [79]. The variations in efficiency across the face of a single tube can easily be 20% or more. In applications where only a small portion of the phototube is illuminated, it would be wise to map out the collection efficiency of the phototube beforehand to find the regions of maximum collection efficiency.

Performing the integrals in (2.17) using the inputs seen in Figures 2.22-2.25, we predict $N_{pe} = 8.8 \pm 1.5$ in each of our detectors, where the error comes from letting the unmeasured factors vary over a reasonable range. Doing the calculation assuming there is no wavelength shifter yields $N_{pe} = 5.1 \pm 0.8$.

2.6.3 Predicted Čerenkov Response to Pions

Pions with momenta above the 9 and 13 GeV/c thresholds will start to produce some Čerenkov radiation. The average number of photoelectrons, N_{pe}^{π}, expected from a

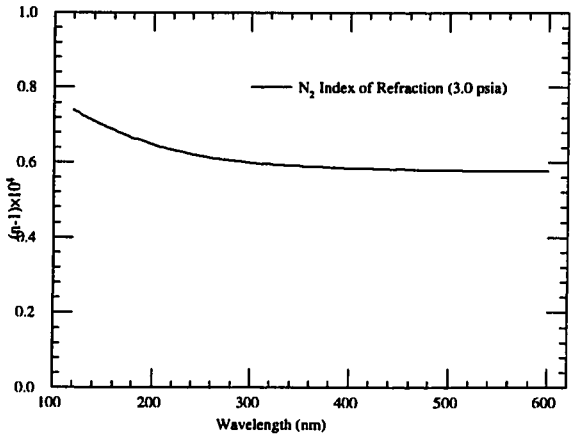

Figure 2.23: The variation of the index of refraction of nitrogen versus wavelength is shown at a fixed pressure (values below 200 nm are from an extrapolation). The small rise seen at lower wavelengths implies that the momentum threshold for producing Čerenkov radiation is not sharply defined

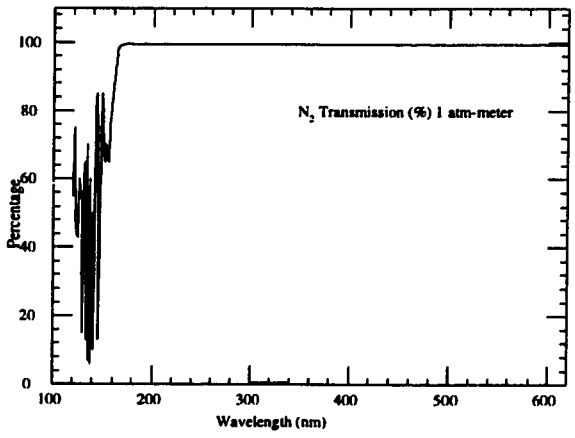

Figure 2.24: The transmission curve for 1 atm-meter of nitrogen is shown versus wavelength. Nitrogen transmits well down to 150 nm and so is a good gas for Čerenkov detectors.

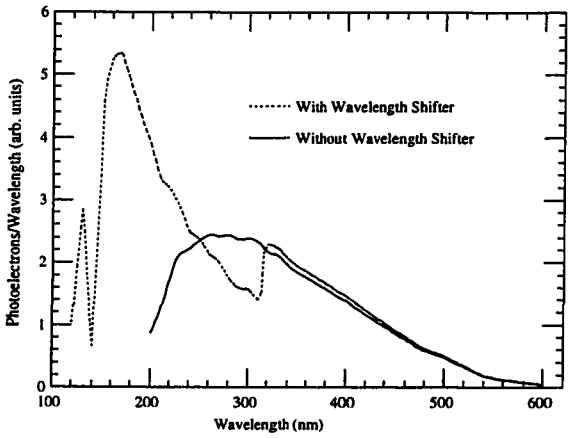

Figure 2.25: This plot shows the effects of the wavelength shifter on the response of the phototube to Čerenkov light. The height of each curve reflects the number of photoelectrons produced from light of a particular wavelength. The response at small wavelengths is seen to improve when a wavelength shifter is used.

pion of momentum P, can be written :

$$N_{pe}^{\pi} = N_{pe}^{e^-} \left(1 - P^2/P_t^2\right) \Theta \left(P - P_t\right) \tag{2.19}$$

where $N_{pe}^{e^-}$ is the average number of photoelectrons produced by an electron, and P_t is the pion threshold of the detector.

Since the index of refraction is a function of wavelength (see Figure 2.23), the pion threshold depends on wavelength. At smaller wavelengths the index is larger, and pions can often produce Čerenkov light below the nominal threshold, which was defined in our tanks at about 250 nm. This subthreshold behavior is counterbalanced by having discriminator cuts at 1 photoelectron or higher, so the effective pion threshold should be close to the nominal value. The observed response to pions is discussed briefly in Chapter 3.

2.6.4 Gas System

Ultra high purity nitrogen (> 99.999% pure) was delivered to the tanks in 12.7 mm diameter electropolished stainless steel tubing, after having passed through a Matheson 462 oil and water filter and a Nupro mesh filter. The filling and evacuating of the tanks was controlled remotely from the Counting House, and used a 50 cubic feet per minute pump equipped with a molecular sieve and liquid nitrogen trap. Such measures were necessary to minimize the possibility of oxygen, water and oil contaminating the vessels and absorbing the Čerenkov photons.

To set the pion threshold we measured the pressure and temperature in each tank. The index of refraction was then inferred from the Lorenz-Lorentz relation,

$$\frac{n(\lambda)^2 - 1}{n(\lambda)^2 + 2} = K(\lambda)\rho \tag{2.20}$$

where for N_2 $K(\lambda$=546 nm$) \approx 0.163$ cm^3/g [85]. Pressure in the 2 m tanks was monitored with Setra Model 270 pressure transducers accurate to $\pm 0.1\%$, and in the 4 m tanks by TransMetric Model P21A transducers, also accurate to $\pm 0.1\%$. The temperature was monitored with Yellow Springs Instruments Model 4320 Thermilinear thermometers, good to ± 0.1°C. At 22°C, the 4 m tanks operated at 2.99 psia, and the 2 m tanks at 6.24 psia. The tanks were partially evacuated and refilled once in the experiment to maintain a constant threshold to within a percent or so. Leak-up rates were from 30-60 mtorr/day.

2.6.5 Čerenkov Electronics

The pressure and temperatures in the tanks were read out by Slow Analog Monitors (SAMs) every five minutes and written to tape. Each PMT output went to the Counting House through fast Heliax 50Ω (β=0.96) cables, and was then split eight ways using LeCroy (LRS) 428F fan-outs. Four of these outputs were delayed and then went to our ADCs, with one output for each of our four crates. The remaining four went to LRS 821 discriminators. Here, signals passing a low threshold of 50 mV (just above one photoelectron) went on to form a part of the Main Trigger and hodogate (see section 2.9). The times of such events were recorded in the C1L or C2L TDC channel as appropriate. Čerenkov signals passing a 70 mV threshold were

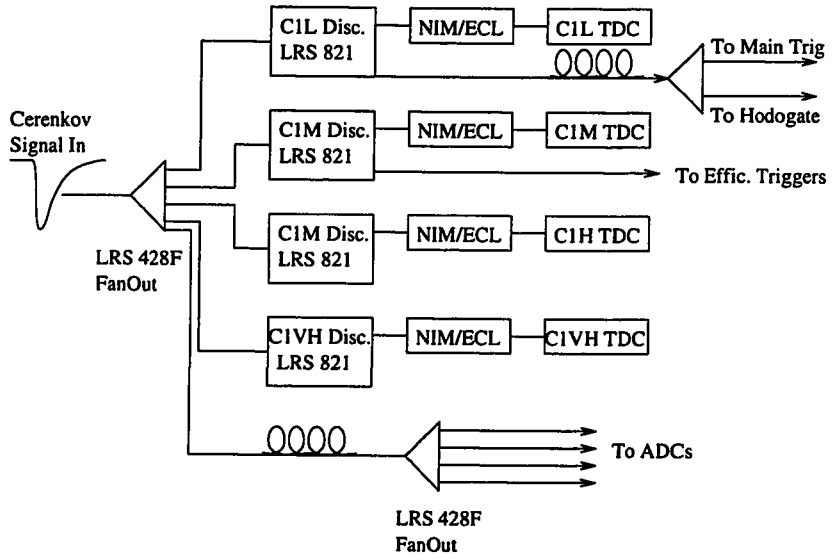

Figure 2.26: The signals from each Čerenkov were split 8 ways. Some of the outputs were used to form various triggers, and the others were digitized. In the offline analysis, Čerenkov pulse heights could be used to differentiate pions from electrons.

recorded as C1M or C2M in the TDCs, and formed part of the efficiency triggers. High and very high thresholds were set at 90 and 120 mV and recorded in the TDCs but were not used for any of the triggers. A schematic of the electronics is presented in Figure 2.26. LEDs were installed in each tank to be used in conjunction with those in the hodoscopes to facilitate timing the electronics. In addition, they were useful for determining the effect of the dipole magnet fields on our PMTs.

2.7 Hodoscopes

While the primary e^- identification came from the Čerenkov counters and lead glass array, a scintillator hodoscope tracking system was used to :

a) provide the initial energy calibration of the lead glass array.
b) verify that there was a track consistent with the Čerenkov and Pb glass data for each event.
c) assess possible systematic errors in the Čerenkov and Pb glass.

d) determine the pion asymmetry.

The hodoscope system has been described fully by Xu [86].

2.7.1 Geometrical Considerations

The angular resolution required of the hodoscope system was estimated according to

$$\frac{dx}{x} = \frac{1}{E'}\left(\frac{E}{E-E'}\right)\frac{dE'}{d\phi}d\phi + \cot\left(\frac{\theta}{2}\right)d\theta. \tag{2.21}$$

To achieve 10% resolution in Bjorken x from our momentum dispersion $(dE'/E')/d\phi$ $\approx$ 2.2%/mr, we find the required angular resolution to be dϕ and d$\theta \approx$ few mrads, and the momentum resolution $dE'/E' \approx 2\%$ [87]. By overlapping our fingers by 1/3 as shown in Figure 2.27, we doubled the spatial resolution. Then, given an area ΔX $\times$ ΔY to be covered by the fingers, and a plane separation of ΔZ, the required number of overlapping fingers, N, to achieve a resolution, $d\phi$, is determined from :

$$d\phi = \frac{1}{\sqrt{12}}\frac{1}{\Delta Z}\sqrt{\left(\frac{\Delta Y_{Front}}{2N_{Front}}\right)^2 + \left(\frac{\Delta Y_{Rear}}{2N_{Rear}}\right)^2}. \tag{2.22}$$

The layout was similar in each spectrometer. A total of 188 fingers grouped into 6 planes was used in the 4.5° spectrometer, and 182 fingers in 6 planes in the 7.0°. The six planes were denoted H1X, H2Y, H3Y, H4X, H5Y, and H6U where the second index is the plane number and the third index is the axis parallel to the fingers (U denotes a 45° angle). Each plane was oriented perpendicular to the central trajectory ($\hat{z}$ direction). The H1X, H2Y and H3Y planes were placed in front of the 4 m Čerenkov, and the H4X, H5Y and H6U planes at the other end, just in front of the Pb glass array. The resolution achieved with this system 0.8 mrads in ϕ and θ. The salient features are given in Table 2.7.

2.7.2 Construction Details

Given the large pion background, good timing resolution was required to minimize tracking ambiguities. For this reason, fast photomultiplier tubes (PMTs) and scintillators were selected. The fingers in the H1X, H2Y, H4X, H5Y planes were made of

Plane	Fingers	Width (mm)	Length (mm)	Thickness (mm)	Active Area $\hat{x}$(mm)× $\hat{y}$(mm)	Distance to Target (mm)
H1X	34	20	589	6.35	410 × 470	23471
H2Y	31	30	430	6.35	410 × 470	23490
H3Y	20	48	356	6.35	410 × 470	23621
H4X	27	30	1070	6.35	510 × 1050	28214
H5Y	55	30	510	6.35	510 × 1050	28233
H6U	21	75	200-820	10.0	510 × 1050	28420
H1X	23	30	690	6.35	400 × 560	18526
H2Y	36	30	430	6.35	400 × 560	18544
H3Y	20	48	483	6.35	400 × 560	18679
H4X	27	30	1070	6.35	500 × 950	23337
H5Y	55	30	510	6.35	500 × 950	23356
H6U	21	75	200-820	10.0	490 × 950	23543

Table 2.7: The dimensions of the 4.5° spectrometer (upper table) and 7.0° spectrometer (lower table) hodoscopes are listed.

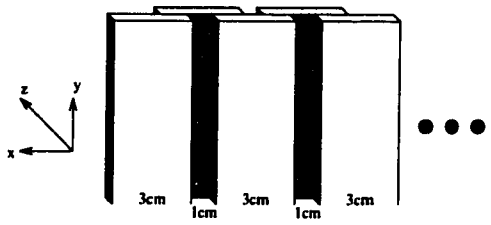

Figure 2.27: Hodoscope 1/3 finger overlap

Characteristic	Bicron BC404
Density	1.032 g/cm^3
Refractive Index	1.58
Light Output	68% of Anthracene
Rise Time	0.7 ns
Pulse Width	2.2 ns FWHM
Light Attenuation Length	140 cm
Wavelength of Maximum Emission	408 nm

Table 2.8: The properties of the hodoscope scintillator are listed.

Characteristic	Hamamatsu R4014
Spectral Response	300 to 650 nm (max. at 420 nm)
Photocathode	Bialkali, 10 mm useful diameter
Dynode Structure	10 stages, linear focused
Operating Voltage	1100 V
Anode Pulse Risetime	1.1 ns
Transit Time Spread	0.5 ns

Table 2.9: The properties of the hodoscope phototubes are listed.

Bicron BC404 scintillator (described in Table 2.8). The PMTs used in these planes were 1/2″ Hamamatsu R4014 (described in Table 2.9). The H3Y and H6U planes used 2″ tubes and played only a secondary role in the tracking, since their timing and spatial resolutions were less fine. The tubes were tested and those with lowest quantum efficiency were matched with the shortest fingers, in which light attenuation is a minimum. The PMTs were attached to a cylindrical light guide 2.54 cm long and 1.27 cm in diameter, which in turn was connected to a wedge shaped light guide attached to the scintillator. No optical grease was used, instead the tube and light guide were held rigidly by heat shrink tubing, fiberglass and electrical tape. A piece of black lucite was glued to the end of the finger to prevent reflections, then the whole finger was wrapped with Al foil and electrical tape. Completed H1X, H2Y, and H3Y planes were mounted in one Al frame, and the H4X, H5Y, and H6U planes in another. Within each plane, the fingers were mounted with a positional uncertainty of

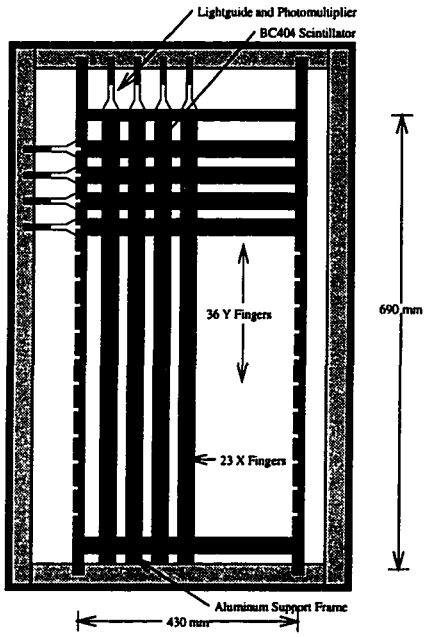

Figure 2.28: Schematic of a hodoscope plane

≤ 0.08 mm. Each three plane assembly was equipped with tooling balls so they could be located in the spectrometer hut with sub-millimeter accuracy. A schematic of a completed finger and plane is shown in Figure 2.28. To help determine the relative timing of fingers within a plane, the H1X, H2Y, H4X and H5Y planes were equipped with LEDs, driven by a common 0.4 ns risetime pulser. The interplane timing and final adjustments of the timing constants came from a careful analysis of the data taken during the run.

2.7.3 Hodoscope Electronics

The LeCroy 4032 high voltage supply for the PMTs was located in the Counting House and connected by 75 m of SHV cable. The output of the phototubes went to LeCroy 4413 discriminators located in the detector huts. Each signal passing a 50 mV threshold resulted in a 30 ns wide ECL logic signal. The logic signal passed via ribbon cable 48.8 m to a set of repeater cards. Here the logic pulses were reshaped as they had been broadened and attenuated. After another 48.8 m the signals entered the

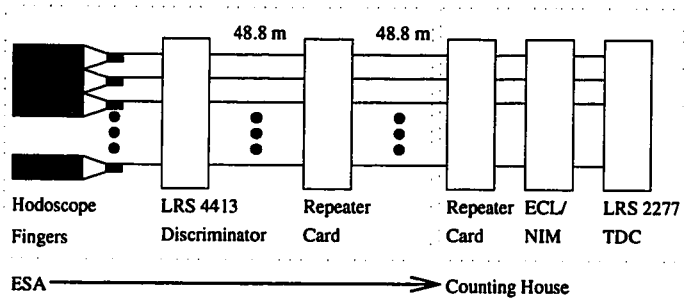

Figure 2.29: Hodoscope Electronics

Characteristic	Schott F2 Pb Glass Block
Composition	Pb 41.8%, O 29.7%, Si 21.5%, Na 3.7%, K 3.3%, Ce 0.35%
Dimensions	62 mm×62 mm×750 mm
Radiation Length	3.17 cm
Index of Refraction	1.58

Table 2.10: Properties of the Pb glass blocks

Counting House and were reshaped a second time. These repeater cards were gated by the Hodogate (see section 2.9) to reduce the event size. After an ECL→NIM conversion, the signals passed to LeCroy 2277 multihit TDCs, with one channel per finger. Each channel has 16 bit resolution (65 μs in 1 ns bins) and could record up to 16 hits with a timing resolution of 0.75 ns. Only hits separated by $>$ 20 ns could be distinguished. A schematic of the electronics is presented in Figure 2.29.

2.8 Shower Counter

2.8.1 Apparatus

Each spectrometer was equipped with an electromagnetic calorimeter to measure the scattered electrons' energies and to provide a tool for pion-electron discrimination. The calorimeters of each spectrometer were identical in design, each consisting of a 10×20 fly's eye array of extruded Schott F2 lead glass blocks. Some properties of the blocks are listed in Table 2.10. These blocks were originally part of the ASP detector of the PEP storage ring at SLAC [88]. They were fine for our use since they had been

treated with cerium to improve their radiation hardness and so were still in good condition. Also, being 23.7 radiation lengths long ensured that the electron shower would be completely contained.

The 400 best blocks from ASP were selected and wrapped with aluminum foil and two layers of 20 mil Calpico (black tape). At the downstream end was an Amperex XP2212PC 12 stage photomultiplier tube attached with Stycast 6061 optical epoxy. The active array of these 2″ tubes covered 42% of the block. No extra material was placed between the blocks when they were stacked, however there were $\approx$ 2 mm air gaps between the bars due to mm scale ripples in the Pb glass. When stacked, the entire array covered an area 635 mm $\times$ 1280 mm, with the long axis of the blocks almost parallel to the spectrometer axis. The assembly was placed in an aluminum box, which presented a 0.8 mm thickness to the incident electrons. To eliminate the possibility of electrons propagating entirely through the small gaps between blocks, the array was inclined with respect to the central trajectory. The 4.5° (7.0°) detector was rotated 4° (4.0°) counterclockwise in $\hat{x}$ and 2.26° (1.3°) counterclockwise in $\hat{y}$. A schematic of one of the calorimeters is presented in Figure 2.30. The shower counter has been described in more detail by Roblin [89].

2.8.2 Shower Counter Electronics

The bases for the shower photomultipliers were on 60 mm $\times$ 60 mm printed circuit boards located at the back of each tube, making the blocks easy to stack. The output of each block went via 50Ω foam cables about 90 m to the Counting House where the analog signal was split into 5 parts, each $\approx$ 17% of the original. Four of the signals were delayed 200 ns by a solid state chip so that the signals would fall inside our ADC gate. Each of the four signals went to a separate crate of ADCs, where the first crate was gated by the first trigger formed, the second crate by the second trigger, and so on. In this manner the ADC information for up to four triggers per spill could be recorded. Digitizing the signals was accomplished with LeCroy 2282 12 bit ADCs, with each crate controlled by a LeCroy 2280 processor. The fifth outputs of all 200 blocks were summed in a series of LeCroy 628 Linear Fan-Ins. This summed output went to a discriminator with five threshold settings, with each threshold having its own TDC channel so we could record the time of each event [90]. The thresholds and

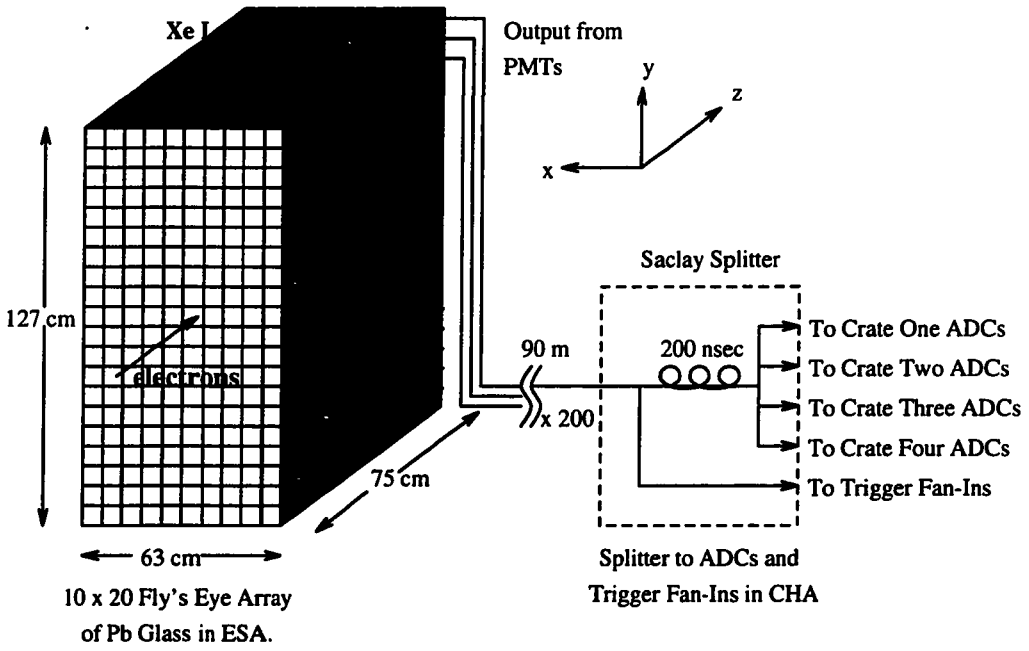

Figure 2.30: Schematic of the electromagnetic calorimeter with the first stage of its electronics.

their associated TDC names were : very low at 30 mV (called ShVL), low at 50 mV (ShL), medium at 115 mV (ShM), high at 156 mV (ShH), and very high at 180 mV (ShVH). Figure 2.31 shows the layout of the shower electronics.

Since electrons would surpass the ShL threshold with >95% efficiency, signals passing this threshold were used as an element in our Main Trigger[4]. Outputs from the ShVL discriminator were used in the PionOr pion trigger, while signals passing a medium threshold, ShM, were used in the efficiency triggers.

2.8.3 Xenon Lamp Calibration

Fiber optic cables were attached to each block and coupled to a Hamamatsu L2360 Xe flash lamp. The initial intention was to use this system to aid in the calibration of the shower counter, however the transmission coefficients and coupling of the 200 fibers to the blocks were not uniform and showed large fluctuations. Instead the system was used to check that the hardware of each lead glass block was functioning properly during the experiment.

2.9 E142 Triggers and Data Acquistion

The triggers for each spectrometer were identical in design, but operated independently. They were designed to :

a) provide rapid electron identification.
b) trigger on events useful for determining detector and trigger efficiency.
c) permit sampling of the pion background in our experiment.

2.9.1 The Main Trigger

The majority of the data written to tape, $\approx$ 97%, was selected with our Main Trigger. This consisted of a triple coincidence, denoted by C1L·C2L·ShL, between signals passing the low thresholds of each Čerenkov and the low threshold of the shower

[4]The trigger used for recording electron data

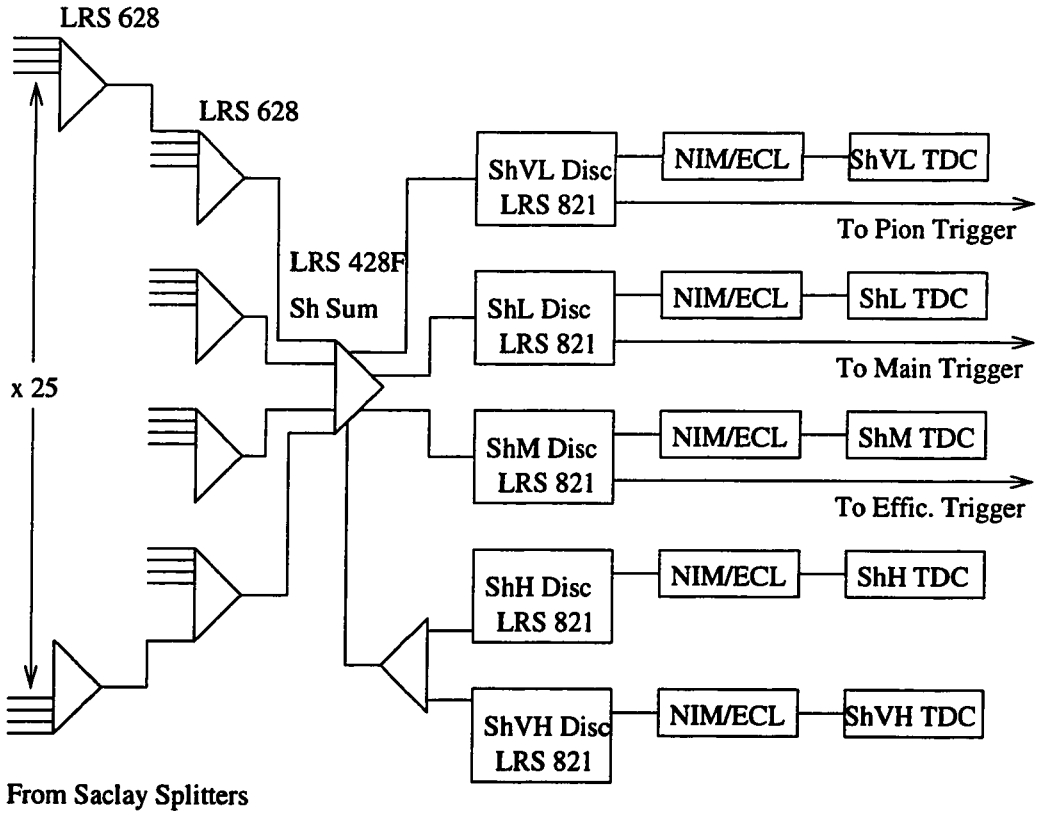

Figure 2.31: The output of each block was fanned out five ways (see Figure 2.30), and one of these was combined with the output of all other blocks through a series of LRS 628 fan-ins. This sum of all activity in the calorimeter was fanned out to five discriminators, and signals passing the thresholds were used to form various triggers.

counter (where · denotes a 20 ns coincidence). Each Čerenkov component of the trigger was > 99% efficient at detecting electrons, and the shower component was ≈ 98% efficient. Reducing the shower threshold would have increased its efficiency, at the expense of being contaminated by more pions. With this setup, electrons scattered through our spectrometers caused a Main Trigger to be formed with >96% efficiency. In principle, from here we needed only to record the ADC information of the shower counter to reconstruct the energy of the electron, and repeat the process about 300 million times. In practice, we need to record timing information to help separate background events, and we need to use other triggers to investigate backgrounds and efficiencies. The trigger and electronics have been described by Spengos [90].

2.9.2 ADC Gating

Coincidence widths set in the electronics were 20 ns wide, and the coincidence units themselves were of the "updating"/"extendable" variety to reduce the losses in efficiency from noise in the inputs. This choice also made it easier to calculate the electronics deadtime of the system. Output from the Main Trigger coincidence unit did not directly gate the electronics, but was sent to the MainOr. The MainOr was the logical OR of its inputs, which included the Main Trigger, as well auxiliary triggers used to measure detector and trigger element efficiencies (called Efficiency Triggers), and finally a trigger used to detect pions (called the PionOr). Output from the MainOr was sent to the trigger divider. Upon being triggered once, this device would send an output to a gate generator, which in turn would gate the LeCroy 2280 processor controlling the first crate of LeCroy 2282 12 bit ADCs. The ADCs were used to record pulse heights from the lead glass blocks and from the phototubes of the Čerenkovs. The FWHM of this ADC gate was about 97 ns and easily overlapped the signals from the detectors. A second trigger to the trigger divider would gate the second crate of ADCs and so on up to 4 triggers/spill. The trigger divider was reset at the end of each spill and had a deadtime of 5 ns. This system was devised because each ADC in a crate shared the same gate (the one gating the 2280 processor), and only one gate per processor was allowed per spill. The processor performed pedestal subtraction and zero-suppression so only useful information was written to tape. A schematic of the E142 triggers is presented in Figure 2.32.

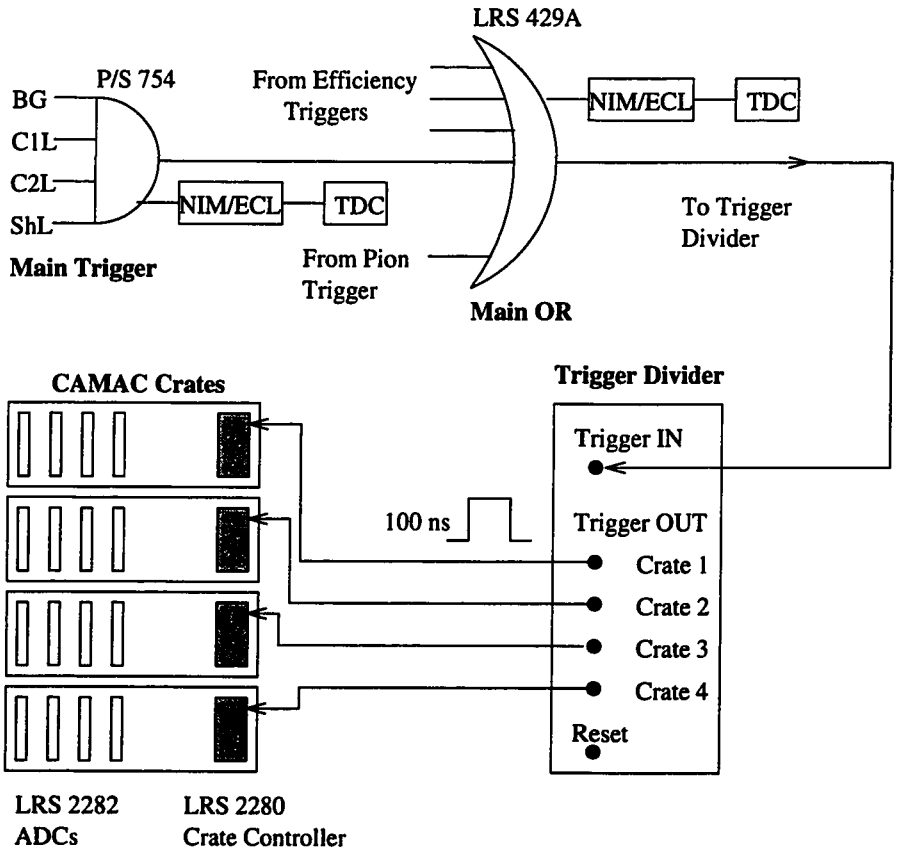

Figure 2.32: The Main trigger, Efficiency triggers and PionOr are each triggered separately. Their output goes to the MainOr, which in turn causes the trigger divider to gate the ADCs. (BG in the diagram denotes beam gate.)

2.9.3 TDC Gating and the Hodogate

All TDCs were ungated except for those connected to the hodoscopes. Ungated TDCs were attached to the Čerenkovs so the times of events passing any of four different thresholds could be recorded. Similarly, the times that the summed shower output passed different thresholds was also recorded. The times of coincidences used in forming the trigger were likewise recorded. The hodoscope TDCs, however, could not be run ungated because the event size became unmanageably large. Instead, the TDCs of the hodoscope were gated with a trigger element called the "hodogate". A separate gate apart from the ADC gate was required because, unlike the ADCs, the hodoscope signals going to the TDCs were not delayed so their gate had to be formed more quickly. Since the summed shower signal was the slowest element to form, the hodogate was formed without the shower counter. To replace it, a charged particle signal, S, was formed from a triple coincidence of two planes of lucite (L1 and L2) and the signal resulting if the summed output of one of the hodoscope planes exceeded a threshold (the H2X (H2Y) plane was used in the 4.5° (7.0°) spectrometer), so $S = H2 \cdot L1 \cdot$ L2. The lucite counters were single sheets of lucite covering the entire acceptance, placed after the last plane of hodoscopes. Two phototubes on opposite corners of the sheets responded to Čerenkov light produced by the passage of a charged particle. The lucite outputs, summed output of one hodoscope plane, and the Čerenkov signals all came to the Counting House by fast Heliax 50Ω cables (β=0.96) to allow the hodogate to be formed quickly. The hodogate was formed from an OR of any of a C1L·C2L coincidence, a prescaled coincidence of one of the Čerenkov low signals and the signal S, or just a prescaled output from S. The hodogate was 100 ns wide and allowed us to record the hodoscope hits during the time in which the ADCs were gated. Every Main Trigger was accompanied by a hodogate.

2.9.4 Efficiency Triggers

A variety of coincidences were formed to aid in our estimation of trigger element and detector efficiencies. The major ones were C1M·ShM·S/N4 (N4 is a prescale factor, which we set to 1), C2M·ShM·S/N4, and C1M·C2M·S/N4. We use the medium thresholds to reduce the effects of noise since we want the triggers to fire only on

real events. The outputs of these coincidences went to the MainOr. Note that these triggers and the Main Trigger were not exclusive, usually 35% of Main Trigger coincidences were accompanied by at least one efficiency trigger coincidence (the rate was not higher because the lucite component of S was <50% efficient).

2.9.5 PionOr Trigger

The trigger C1M·ShM·S/N4 could be fired by a pion whose momentum surpasses the 9 GeV/c threshold of the first Čerenkov (C1). However, to sample the majority of the pions (which have momenta less than 9 GeV/c) we formed a PionOr trigger which was the OR of S/N1, ShVL·S/N2, and ShL·S/N3. During E142 we set all of the prescale factors N1, N2, and N3 to 64, so the pion trigger was effectively S/N1=S/64. This trigger would of course be fired by electrons, but it had the virtue of not excluding any pions, unlike all of the other triggers.

2.9.6 Data Acquisition

The data acquisition cycle was initiated by the A2N accelerator timing pulse which arrives 2.5 μs before the spill, at 120 Hz. (E142 actually ran at 119 Hz since the 120th pulse was used by the linac operators to monitor the beam and for another experiment, E146, running coincidentally.) The A2N went to our beam gate generator which would form a 6 μs long beam gate starting 2 μs before the beam hit the target, and overlapping the beam spills which were typically 1-1.4 μs long. If we were in a run state, the μVax 4000-200 (known locally as ESAU6) would issue a high output called the "run level". The run level and beam gate went to the beam gate switchbox which generated the gate to enable the trigger and electronics. If the computer was busy, beam gate generation was suppressed. The run level/beam switch box scheme allowed us to run with or without computer control of the electronics, or even continuously. The latter were useful for taking calibration data for the shower counter with the xenon lamp, or for special runs with a pulser used to determine timing constants for the hodoscopes. In a normal run state, a delayed output from the beam gate generator was used to generate an interrupt. This interrupt came long after the beam crossing and was serviced by our μVax 4000-200 running VaxELN, a realtime

operating system. The interrupt initiated the CAMAC read and data transfer of the beam and spectrometer information from the spill. The data were read in the following order : beam data, 4.5° spectrometer TDC data, 7.0° TDC data, 4.5° ADC data, 7.0° ADC data. There were three sets of beam polarization information to be written. The polarization bits from the Mach line and Pockels Cell High Voltage were ready 300 μs after the A2N, and were written in the headers of the beam and spectrometer data. The polarization bits from the Veto module arrived 1.5 ms after the A2N, too late to be included in the beam header but usually ready by the time the spectrometer data were read out. To decrease the reading time, the TDC data for each spectrometer were read with one DMA. Separate TDC modules were distinguished by sending a pulse to the last channel of each module 8 μs after the beam gate opened. The resulting TDC hits were clearly separated in time from the TDC stops occurring during the spill, and allowed the divisions between modules to be made unambiguously. The data were sent by DECnet to a Vax 4000-60 (ESAU7) which buffered the data and wrote it to 8 mm tape. The maximum writing speed to tape was 250 kB/s which corresponds to a sustained rate of 2100 bytes/spill. Typically there were 324 bytes of beam data, 800 bytes of 4.5° spectrometer data and 500 bytes of 7.0° data (averaging $\approx$ 550 bytes/electron). The computers ESAU6 and ESAU7 were separated from the rest of the ESA LAN by a bridge to minimize network traffic that could interfere with data taking. The buffered event data on ESAU7 were sampled by two Vax 4000-60 workstations, one for each spectrometer arm, allowing 5-10% of the data to be processed online. The primary intent of the online system was to monitor the detectors and not to extract an asymmetry measurement. Beam control was the responsibility of a dedicated μVaxII running VaxELN. This system performed beam steering and recorded information from the wire arrays, position and energy cavities, as well as the toroids used to measure beam current. The beam information was transferred to ESAU6 before being sent to ESAU7 to be recorded. The beam control computer was also used to recalibrate the toroids (done daily) and measure the ADC pedestals of the wire arrays and toroids. Auxiliary programs needed to run the experiment all ran from a Vax 4000-300 (ESA). These tasks included control programs for the Møller and spectrometer magnets, control of the NMR and Hall probes monitoring the magnets, monitoring crate voltages, controlling the LeCroy

4032 HV chassis, recording SAM and scaler information, as well as logging the data from the target computer.

Chapter 3

Data Analysis

3.1 Overview

The experiment E142 ran for six weeks starting in November of 1992. Data were taken at three beam energies, 19.42, 22.66 and 25.51 GeV, resulting in about 250 Gbytes of data written on 100 8 mm tapes. The data were composed of $\sim$ 300 runs dedicated to measuring the longitudinal asymmetry, 11 transverse asymmetry runs, 10 runs with the magnets' polarities reversed to measure charge symmetric backgrounds, and 32 reference cell runs for measuring the dilution factor. A run consisted of about 500 000 beam spills and required close to $1\frac{1}{2}$ hours (though reference cell runs were typically 100 000 spills). The average event rate in the 4.5° spectrometer was 2 electrons per spill, while in the 7° it was 0.8, with a total of $\sim$ 400 million possible events for the asymmetry analysis before any cuts.

The analysis chain was straightforward. The 8 mm tapes were read back and runs passing cuts on beam, target and detector stability were selected for the asymmetry analysis. In these runs, spills passing cuts on beam quality were further examined for electron candidates. The energies of the electron candidates were reconstructed and the results binned in E′ and θ. These summaries of the data were written out for each run, resulting in a large disk file synopsis of the experiment. From here, a second program was used to extract the asymmetry from the summary files and ultimately produce a value for $\Gamma_1^n(Q^2)$.

3.2 Run Selection

Not all of the data taken during E142 were of sufficient quality that they could be used to extract the spin structure function. Some of the reasons that runs were discarded are :

1 Runs were discarded in which more than 30% of the spills were rejected because the beam failed to pass our beam cuts (see below). This cut removed 12 runs from the analysis.

2 Five runs were removed because they had been cut short due to accelerator or beam steering problems and had fewer than 50 000 spills.

3 Six runs in which one of the dipoles of the 7.0° spectrometer kept losing power were removed from the 7.0° data set.

4 One of the target cells used in the experiment apparently began to leak ^{3}He after a few runs as evidenced by a decline in event rate and decrease in the size of the ^{3}He NMR signal. Because the dilution factor and polarization of this cell could not be reliably extracted for these runs, they were dropped. This resulted in the loss of 26 longitudinal asymmetry runs and 2 transverse asymmetry runs.

In the remaining runs the beam, target and detectors were sufficiently stable for the asymmetry analysis. In Figure 3.2 we show the event rates in the two spectrometers versus run number. The event rate for these runs remained stable at the percent level and drifted primarily as the beam wandered over a 0.5 mm diameter area on the target, and as the beam spot changed from 1.5 to 3 mm^2 in area.

3.3 Spill Selection

Once runs had been selected for the asymmetry analysis, criteria were developed for selecting or rejecting spills within a run. The only spills accepted for analysis were those in which the beam position, width and charge passed some simple quality checks, in addition to the requirement that the helicity of the beam be well determined.

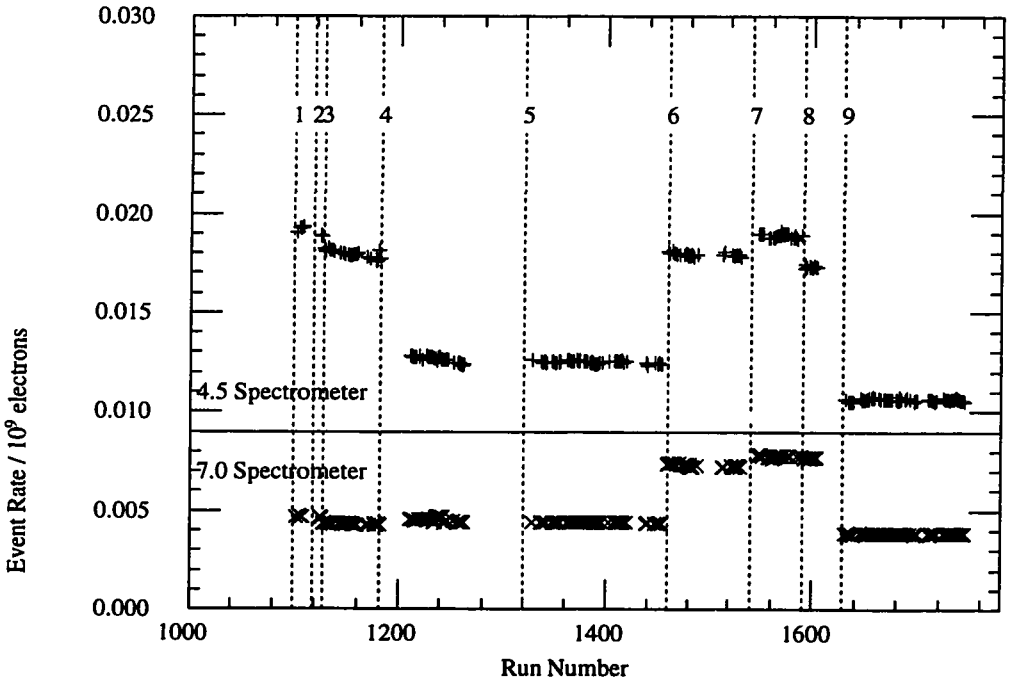

Figure 3.1: The stability of the event rate of the runs selected for the asymmetry analysis are shown. The steps in event rate were caused by : (1) Experiment started at 22.66 GeV beam energy. (2) Target cell changed from Minnehaha to Hiawatha. (3) Target position changed. (4) Target changed from Hiawatha to Gore, and the central momentum setting of the 4.5° spectrometer was changed form 12.5 to 11.5 GeV/c. (5) Target changed from Gore to Minnehaha. (6) Beam energy changed from 22.66 to 19.42 GeV. (7) Target position changed. (8) Central momentum setting of the 4.5° spectrometer changed from 8.6 to 11.5 GeV/c. (9) Beam energy changed from 19.42 to 25.51 GeV.

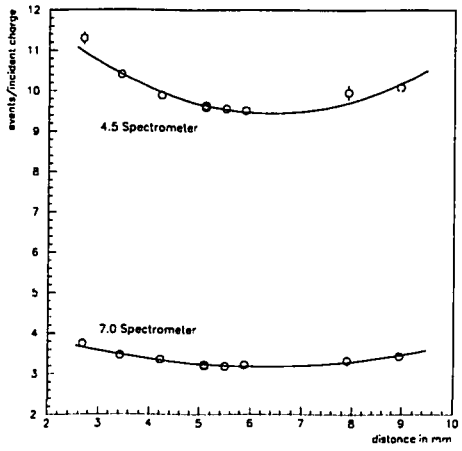

Figure 3.2: This figure shows the change in event rate as the target is swept through the beam. The change in rate is well described by a quadratic and is attributed to the beam passing through increasingly thick parts of the target endcaps. During data-taking the target is positioned at the event rate minimum.

3.3.1 Beam Cuts

Variations in the beam position and spatial distribution at the target will have an impact on the measured asymmetry. This occurs primarily by affecting the ratio of events coming from ^{3}He to those coming from the glass endcaps of the target (the dilution factor) because the endcap thickness increases away from the center while the path length in ^{3}He remains roughly constant. If the ratio fluctuates in a manner dependent on the beam helicity then the measured asymmetry will be biased. Our saving grace is that target polarization reversals allowed us to average over possible helicity dependencies in the beam parameters so over the whole experiment the average dilution factor will be the same for the $\sigma_{1/2}$ and $\sigma_{3/2}$ measurements. We can estimate limits on acceptable values of the beam position and size (σ) by looking at the event rate as the target is swept through the beam. Such a sweep is shown in Figure 3.2 in which the event rate/incident charge is seen to rise quadratically as the beam is moved away from the thinnest region of the target endcaps. The rate of rise in the 4.5° and 7.0° is consistent with a <2% change in rate for a 1 mm change in beam position away from the center. We can then determine that beam induced false asymmetries will be insignificant if the left and right handed beams hit the tar-

Beam Parameter	Left (L)	Right (R)	(L-R)	(L-R)/(L+R)
charge/spill (10^9 e^-)	131.1559	131.1273	+0.028600	+0.000109
x (mm)	0.009144	0.008864	+0.000281	———
y (mm)	0.177184	0.176689	+0.000494	———
σ_x (mm)	1.652138	1.652549	-0.000411	-0.000124
σ_y (mm)	1.335076	1.335148	-0.000072	-0.000027

Table 3.1: Important beam quantities averaged over the experiment.

get at the same position within 0.002 mm (given a true counting rate asymmetry of $\sim 5\times10^{-4}$). In Table 3.1 we show the values averaged over the experiment of the important beam parameters for the two beam helicity states (where Right refers to positive helicity electrons *at the target*). The differences between the left and right handed beams are well below the level at which they would generate a significant false asymmetry (this is confirmed by another method). Note that the absolute x and y positions of the beam on the target are arbitrary, only the helicity dependence of the difference is meaningful. Having confirmed that the beam helicity dependencies are innocuous, we still needed to implement cuts to ensure that the beam hits the target in the center and that the beam conditions remain stable. To this end, the spills in which the beam position or width varied by more than 4σ from its average value in the run were excluded. If the incident charge fluctuated by more than 5σ then these spills were discarded. An example of the cuts is seen in Figure 3.3. These cuts were relatively loose and were useful for removing the small fraction of spills with properties far from the average. This ensured the stability of the dilution factor and prevented large fluctuations in rate within a run which would distort our detection efficiency due to rate dependent effects. As noted above, over the whole experiment the beam was kept centered on an area about 0.5 mm in diameter on the target, and the spot size varied from 1.5 to 3 mm^2, ensuring that the dilution factor was stable from run to run.

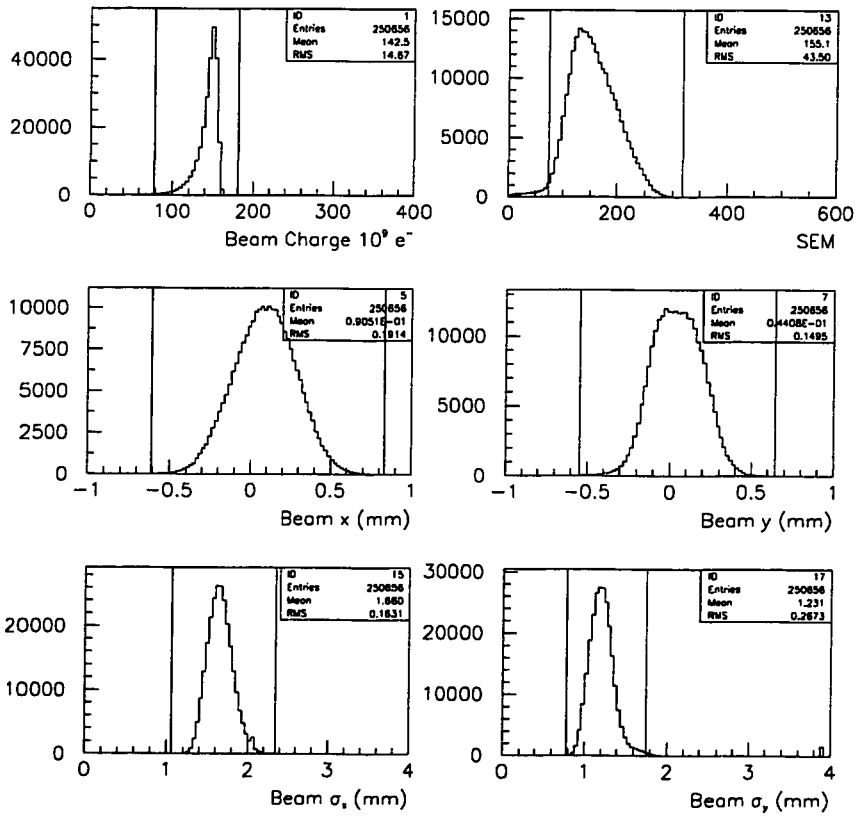

Figure 3.3: The effects of the beam cuts on spill selection can be seen in these plots. Solid lines represent the acceptable range of beam parameters for this particular run. It is seen that the cuts, which are purposefully loose, serve to remove the aberrant spills only.

3.3.2 Polarization Determination

Another criterion for accepting or rejecting a spill was that we know the polarization of the beam for that particular spill. Although there were three separate sets of beam polarization information (see sections 2.9.6 and 2.2.4), the Veto bits demonstrated a serious timing problem so that they were not read out reliably by the data acquisition system and could not be used for the asymmetry analysis. Instead, a spill was selected if the Mach line and Pockels cell high voltage line both independently indicated the same helicity state for the beam. The two systems were in disagreement for only 24 out of more than 300 million spills, suggesting an error rate at or below the level of 10^{-7}.

As a check on the integrity of the system, several tests were performed in which beam of predominantly or entirely one helicity was sent to the end station. The pattern of beam helicity recorded in our data acquisition was then checked with that issued at the source and found to agree. In principle there was a final check we could perform on the integrity of the beam polarization determination. Since the beam polarization on a spill to spill basis was determined with a known algorithm, it could be predicted from one spill to the next based on the helicity of the previous 33 spills (see section 2.2.4). In practice this was difficult to achieve because the polarization information of every 120th spill was not retrieved by our data acquisition (this spill was used for accelerator tuning and didn't enter the end station). This caused the predicting algorithm to lose synchronization with the beam every 120 pulses, but in a regular fashion from which we could recover from by counting beam pulses, looking at the time of the spill from a real clock, and by looking for a spill using the same time slot as the previous spill. Another difficulty was that each run was paused from ten to twelve times to write out diagnostic information from the detectors and beam monitors. The exact timing and duration of these checkpoints were not synchronized with the beam so the polarization of at least several hundred spills could not be predicted while the predictor got back in synchronization with the beam. Any other pauses in the run would also disrupt the prediction of the polarization bits. Given these exceptions we expected the predictor to be perfectly accurate for the remaining 99.9%+ of the spills composing a run, which was confirmed in random test cases. This success gave us further confidence that the Mach line and Pockels cell high voltage

line were valid, especially considering their mutual agreement to better than a part in ten million.

3.4 Trigger Selection

Having selected a run to be analyzed, and the spills within the run, the next step was to isolate particular triggers within a spill for further study. The Čerenkov and shower counter responses of these selected triggers were examined for evidence of an electron as we describe below. It is at this stage that the analysis of each spectrometer becomes independent since they were each triggered separately.

In each spectrometer separately, the gates of the shower counter and Čerenkov ADCs were opened by the output of a coincidence unit called the Main Or. Each Main Or in turn was activated by any of five different triggers, each of which had a different efficiency for triggering on electrons (see section 2.9.2). For this analysis we only examined spills for which the Main Trigger; C1L·C2L·ShL representing a triple coincidence between the two Čerenkovs and the shower counter, had fired within ± 10 ns of the Main Or. The Čerenkov components of the trigger were 99% efficient at detecting electrons, and the shower component was 98%, for an overall trigger efficiency of 96% (see section 2.9.1). A further criterion for accepting a trigger for analysis was that the ADC of each Čerenkov had to exceed 25, which was slightly above the one photoelectron threshold. This reduced our sensitivity to noise in the Čerenkovs and removed a few of the triggers caused by pions above the 13 GeV/c Čerenkov threshold. The rate dependence of the trigger efficiency and its implications for the asymmetry measurement are discussed in section 3.6.5 on electronic deadtime effects.

3.5 Electron Identification

Identifying deep inelastically scattered (DIS) electrons and determining their energy was the next essential step in extracting $g_1^n(x, Q^2)$ from the raw detector data written to tape. The primary background to be disentangled came from pions created by photoproduction at the target. These were rejected at the trigger level by requiring

the formation of a Main Trigger, which required that both Čerenkovs fired. Since very few pions had momenta greater than 13 GeV/c, only a small fraction could fire the Čerenkovs and set off the Main Trigger. The result is that by requiring a Main Trigger and demanding that the Čerenkov ADCs be >25, we were almost guaranteed that an electron had entered the spectrometer. It remained to identify the electron in the lead glass calorimeter and determine its energy.

3.5.1 Observed Cerenkov Response to Electrons

Since the Čerenkov detectors were an integral part of our trigger, it is helpful to discuss their response to electrons in order to understand our electron identification scheme. Although a great deal of information about the charged particles traversing a detector is contained in the Čerenkov signal, we will focus our discussion on the number of photoelectrons produced, since this quantity is closely related to the electron detection efficiency. The average number of photoelectrons in our counters was estimated using the efficiency triggers. To test the large C2 detector, we select events with triggers caused by a C1M·ShM·S coincidence and verified that there was a track and shower cluster present with $|E/p - 1| < 0.15$ and a neural network response >0.95 (see section 3.5.4). This defines a good electron in a manner completely independent of the response of C2 (we can do the same for C1 by using C2 in the trigger selection instead). After plotting the ADC response to such events we can extract the number of photoelectrons, N_{pe}, by several techniques. If the fluctuations in PMT output are dominated by Poissonian variations at the photocathode, then the probability of having zero photoelectrons produced is $P(0) = \exp(-N_{pe})$. This null response, smeared by pedestal fluctuations is visible in Figures 3.4-3.5. A second commonly used technique is to assume that the gain at the first few dynodes is very high so that the electron multiplication in the dynodes can be considered noise-free. Then $N_{pe} = (\mu/\sigma)^2$, where μ is the mean and σ^2 is the variance of the ADC spectrum. If we take into account the statistical fluctuations (assumed Poissonian) occurring during multiplication, then

$$\left(\frac{\mu}{\sigma}\right)^2 = \frac{N_{pe}}{1 + \sum_{i=1}^{k} \prod_{j=1}^{i} \frac{1}{g_j}} \tag{3.1}$$

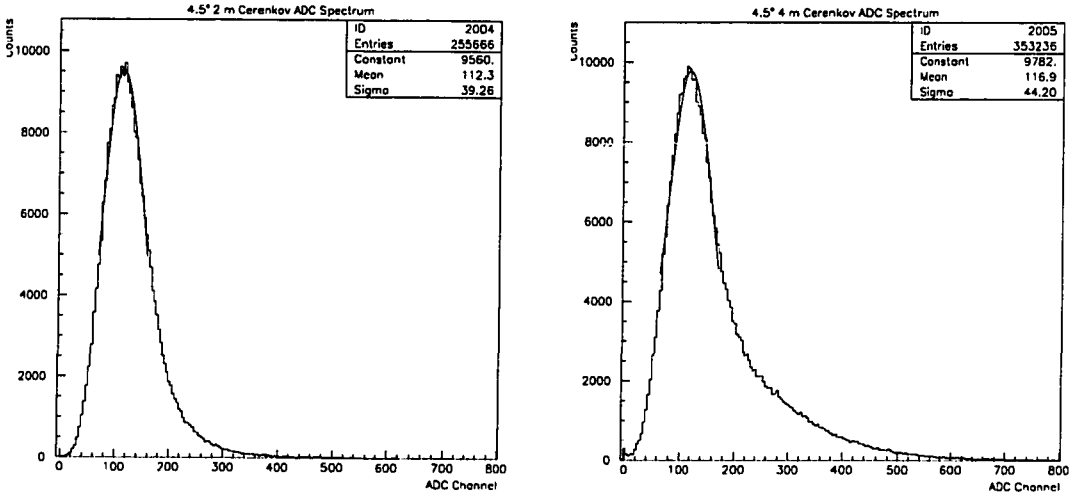

Figure 3.4: ADC Response of C1 and C2 of the 4.5° spectrometer.

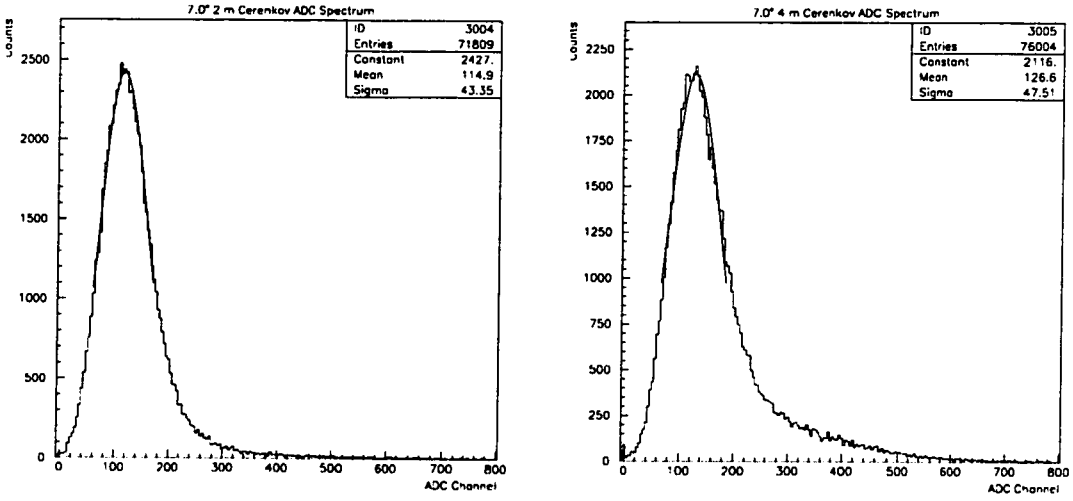

Figure 3.5: ADC Response of C1 and C2 of the 7.0° spectrometer.

Spec.	N_{pe} in C1	N_{pe} in C2	N_0 in C1 (N_{pe} cm^{-1})	N_0 in C2 (N_{pe} cm^{-1})
4.5°	8.1 ± 0.5	7.3 ± 0.3	169 ± 10	158 ± 6
7.0°	7.4 ± 0.4	7.2 ± 0.4	154 ± 8	156 ± 8

Table 3.2: Čerenkov Detector Photoelectron Yields

where k is the number of dynodes and g_j is the gain of the jth dynode [91]. Evaluating this factor for our PMTs yields $N_{pe} \approx 1.16 \times (\mu/\sigma)^2$. Fitting the top half of the ADC spectra with Gaussians suggests that $N_{pe} = 9.5 \pm 1.5$ for C1 of the 4.5°, and 8.0 ± 1.5 for the others. These results are strongly dependent on the fitted range and the χ^2/df were typically 2-4.5.

A Monte Carlo of the multiplication process at the photocathode and first four dynodes with several different Polya distributions showed that the most accurate information about N_{pe}, least dependent on the statistics of dynode multiplication, is gleaned by estimating $P(0)$. This seems reasonable since with high first gain dynodes, $g_1 > 10$ as in our PMTs, the probability of events with more than one photoelectron at the photocathode yielding a null output are $< 10^{-4}$. The results of this approach, which we take to be accurate reflections of the detector response, are shown in Table 3.2, where the errors reflect the uncertainty in $P(0)$. The discrepancy in photoelectrons with the peak fitting method is not serious because the ADC spectra are clearly non-Gaussian, and using the mean and sigma of the ADC distribution is only an approximation. The non-Gaussian behavior can result from non-uniformity in gain of the dynodes, and from variations in the collection efficiency across the face of the PMT. The response is better described by a Polya distribution (effectively the sum of Poisson distributions of different means). The effects due to non-uniformity are at a maximum for us because we use the full face of the PMT for light collection.

A common measure of Čerenkov response is the value N_0, which is defined by $N_{pe} \equiv N_0 L \sin^2\theta$. These are given in Table 3.2 and average to ≈ 160 cm^{-1}, which is a good level of performance for a detector of this type. If we estimate our efficiency, η, from $\eta = 1 - \exp(-N_{pe})$, we find $\eta > 99.9\%$. In practice, the most useful measure of efficiency depends on the cuts. In our analysis we have required the Čerenkov ADCs to be a minimum of 25 channels. This corresponds to a cut of slightly more than 1 photoelectron for which our expected efficiency is $\approx 99.4\%$. The efficiencies

Spec.	Efficiency (ADC>25) in C1	Efficiency (ADC>25) in C2
4.5°	0.99880 ± 0.00006	0.9963 ± 0.0001
7.0°	0.9944 ± 0.0003	0.9959 ± 0.0002

Table 3.3: Čerenkov efficiencies after an ADC cut of 25

after this cut are shown in Table 3.3. An asymmetry measurement only requires that the detector efficiency be the same for both helicity configurations, so in principle wild variations in detector response over the acceptance are innocuous. In practice, the efficiency after cuts of all detectors is rate dependent, and since measuring an asymmetry is the same as measuring a difference in rates, the asymmetry measured is necessarily biased at some level. If the detector response is not uniform, the rate dependence will vary with position and be difficult to account for. Though these effects may be small, we are obviously better off if the detector response is uniform. Apart from a seldom hit corner of C1 of the 7.0°, the efficiencies were $\approx$ 99.5% and uniform below the one percent level. We also note here that the cut at 25 falls in a part of the ADC spectra that is not too-steeply rising and so is only weakly sensitive to variations in the phototube output caused by temperature fluctuations ($\leq 0.2\%/^{\circ}C$) and instabilities in the high voltage.

3.5.2 Observed Čerenkov Response to Pions

The response of the detectors to pions is shown Figure 3.6. The lines on the scatterplot are the theoretical prediction of section 2.6.3 and are seen to match the data well.

3.5.3 Shower Counter Response to Electrons

The response of electromagnetic calorimeters to high energy electrons has been fully described and studied elsewhere [92, 93, 94, 95] so in the following discussion we only introduce the ideas needed to explain our treatment of the calorimeter data.

Electrons impacting the blocks of the shower counter will lose their energy initially by bremsstrahlung. The resultant high energy photons subsequently undergo pair production and the cascade continues until the energies of the secondary electrons and positrons is so low that excitation and ionization become the dominant

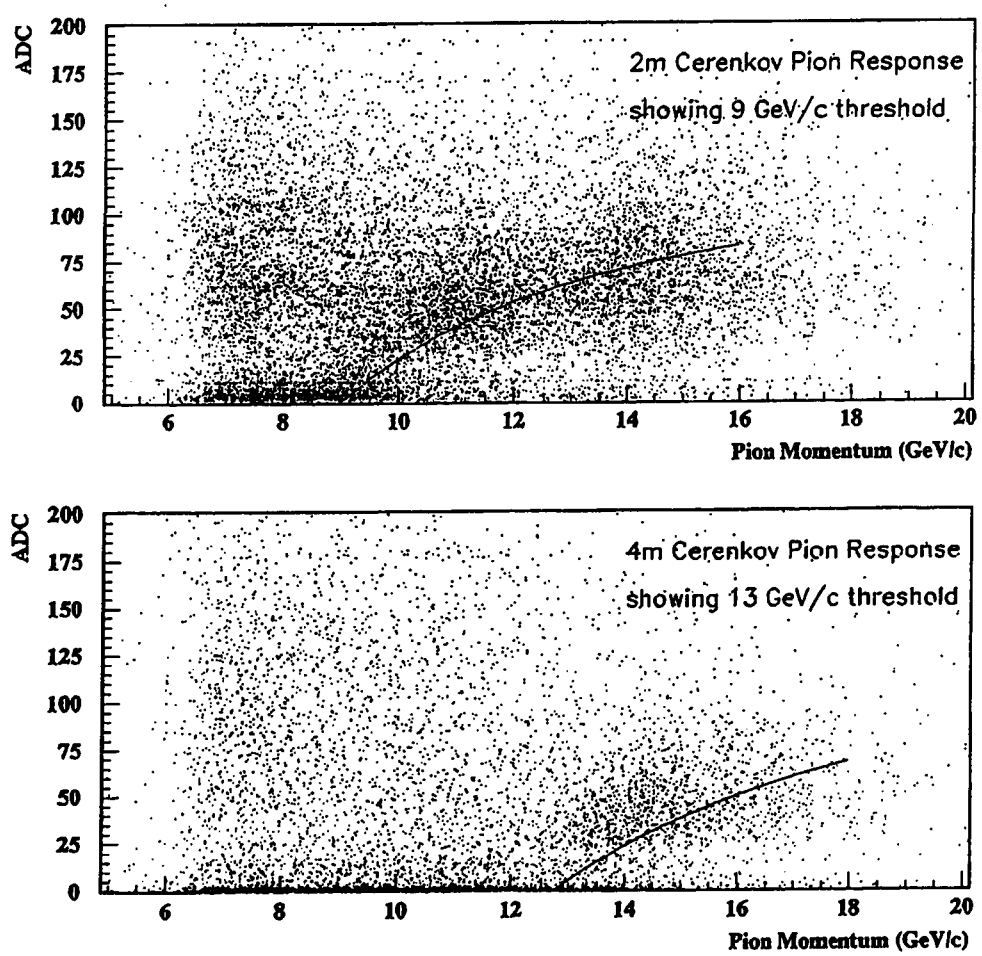

Figure 3.6: The Čerenkov response to pions is shown in this scatterplot of Čerenkov ADC versus particle momentum. The onset of light production above the momentum threshold matches the prediction, shown as a solid line.

energy loss mechanisms. The energy at which radiation and collisional losses become equal is called the critical energy (Rossi has an alternate but similar definition [92]) and is around 15 MeV in our Pb glass calorimeter. The development of the shower depends mostly on the density of electrons in the calorimeter, characterized by the radiation length which was 3.17 cm. Since our lead glass blocks were almost 24 radiation lengths we expected the secondary particles to be at least 99% contained in the detector. The transverse radius of the electromagnetic cascade is typically 2 Molière radii or about 8 cm in our case for 90% containment. With these simple estimates we expect the electrons to deposit all of their energy in about nine of our blocks. Since the secondaries lose energy by more than one mechanism (ionization, excitation, emitting Čerenkov radiation, ...) we don't directly measure all of the incident energy but instead detect the Čerenkov radiation produced by the secondaries, which is taken to be proportional to total energy deposited. The relation is not exact because secondaries below the Čerenkov threshold of <1 MeV do not contribute to the signal detected, and for the particles close to the critical energy the competing loss mechanisms distort both the number of secondaries and the amount of Čerenkov light produced. These latter effects are ultimately what determines the energy resolution of the calorimeter. In the next section we apply these ideas to the response of our calorimeter.

Energy Calibration

The obvious purposes of the calorimeter were to allow us to both detect the DIS electrons and determine their energy. The process began during data-taking with the formation of a trigger. This opened the gates of the ADCs connected to the photomultipliers of the shower counter for 100 ns. In any PMTs which fired the total charge, which was proportional to the amount of Čerenkov light produced in the block, was digitized then written to tape. In the offline analysis the patterns of charge collected in the calorimeter were examined trigger by trigger for clusters of hit blocks we could associate with single incident particles. The remaining task was then to relate the total charge output of the PMTs in a cluster to the energy of the incident particle.

The charge output of a PMT belonging to a block in a cluster was proportional

to the gain of the PMT as well as to the energy deposited in that particular block (nonlinearity of the ADCs and PMTs in the range in which they were operated were negligible). Each block had four separate calibration constants relating charge to energy corresponding to each of the four triggers. Four constants were necessary because the splitters which divided the signals of each shower block into five parts (one for each crate of ADCs and one to form the shower component of the trigger) didn't necessarily divide the signals evenly. Also, the four ADCs associated with a single block had slightly different gains.

Before describing the details of the final calibration of the shower counter, we need to discuss the NPI engineering run and hodoscope tracking, both of which were important elements in the calibration procedure.

NPI Run

An initial calibration of the blocks came from a week-long test run one month prior to E142. This run used the Nuclear Physics Injector (NPI) at SLAC to produce an unpolarized 4.99 GeV beam which hit a hydrogen gas target. The elastic scattering peak was easily seen in each shower counter and provided us with an absolute energy scale. By adjusting the spectrometer magnets' fields we swept the elastic peak across the face of the calorimeter so that many blocks could be calibrated. The NPI run also allowed us to confirm that the passage of electrons through the magnetic spectrometers was understood by comparing the position of the elastic peak in the calorimeter with that predicted from the TRANSPORT matrix elements describing the magnet optics. The momentum resolution of the hodoscope tracking system was sufficiently good (see section 3.5.3) that this was a meaningful test of the spectrometer system. While the NPI run was quite successful in these regards, it indicated that we needed to adjust the voltages of some of the shower PMTs to reduce or expand their dynamic range as required. This meant that the calibration coefficients from the NPI were not used in the end, but we had certainty that the lead glass could be calibrated by tracking the electrons and reconstructing their momenta with the reverse matrix elements describing the magnet optics.

Hodoscope Tracking

To reconstruct the particle momentum from its trajectory after it had passed through the spectrometer magnets, we used the particle's track position at the final plane of hodoscopes (x_f, y_f) and its angles in the non-bend and bend planes (θ_f, ϕ_f). These values were converted using fifth order in y_f and ϕ_f reverse-order TRANSPORT matrix elements to initial positions and angles at the target (x_0, y_0, θ_0, ϕ_0) as well as yielding the particle's momentum [96, 97]. The intrinsic momentum resolution of the fifth order reconstruction was <0.3%, well below the actual momentum resolution set by the granularity of the hodoscope tracking system and multiple scattering [97].

Particle tracks were identified with a simple algorithm which examined the TDCs of the hodoscopes spill by spill. The sixth, H6U, plane was dropped from the analysis to make the algorithm faster. Since these fingers were quite broad and consequently noisy, the resulting losses in momentum resolution and tracking efficiency were negligible. To form a track we were obligated to find an x-y pair of hits in the front and rear planes of hodoscopes; in the front planes we required an H1X and H2Y or H3Y hit, and in the rear plane an H4X and H5Y hit. The main steps in the tracking algorithm were :

1 Hodoscope finger times were first corrected for a time slewing effect arising from electronic crosstalk in the ribbon cables and electronics of the hodoscope system. These corrections were usually of the order of a nanosecond.

2 Hits which were 20 ns earlier or 15 ns later than the Hodogate were excluded since they were the result of electronic pileup (resulting from the finite risetime of the Hodogate).

3 Pairs of adjacent fingers which fired within 7 ns of each other were grouped together and considered as single hits.

4 Starting from each H1X hit, the other planes were searched for hits which coincided with the H1X hit within 12 ns (having adjusted for the time of flight). When enough hits in the other planes were found to form a track candidate, the combination of hits was stored in a table, and the searched resumed until all possible track candidates had been identified.

5 Each combination of hits composing a track candidate was then fit, and those which did not pass phase space cuts, or which didn't point to a cluster in the shower counter were dropped.

6 The remaining candidates were refit with the x and y position of the cluster they pointed to being considered as a point on the track (The uncertainty in a cluster's x or y position was estimated as 10 mm).

7 The timing and spatial χ^2 of each track were then examined, having accounted for the light propagation speed in the scintillator of 143 mm/ns, and tracks with $\chi^2/df > 4$ were dropped. The timing resolution of most of the hodoscope fingers was between 1-2 nanoseconds.

If at this stage if there was more than one track pointing to a cluster, then we decided from amongst these tracks using an argument based on phase space probability. Given that the bend angle and particle momentum were correlated, if the particle we were tracking was an electron then by examining the shower energy we could infer a preferred bend angle. To decide from amongst the remaining acceptable track candidates we selected the one with the favored bend angle. This procedure was not used during the calibration of the shower counter, where we instead chose the track candidate with the smallest χ^2/df. The two approaches selected the same track $> 90\%$ of the time, and only differed when there was a lot of noise in the hodoscopes. In these cases the relative difference in momentum of the tracks was less than 5% and the absolute difference usually less than 0.5 GeV. Note that the two approachs would have yielded the same tracks had we made the χ^2 and phase space cuts more restrictive, at the expense of efficiency.

The tracking efficiency averaged to about 90% in the 4.5° spectrometer and 80% in the 7.0° spectrometer, with the inefficiency being due to noise in the hodoscope fingers. A charged particle passing through a hodoscope finger which had a noise hit within the previous $\sim$25 ns would be unable to register a second hit due to electronics deadtime. The resulting pattern of hodoscope hits would often not allow a track to be reconstructed. In the 7.0° spectrometer a significant number of one bounce photons made their way through the dipoles and inundated the lower half of the first x-y plane of hodoscopes, reducing the tracking efficiency further. It is important to note that

the hodoscope system was intended primarily to calibrate the lead glass calorimeter, so high tracking efficiency was never required for the success of the experiment.

Shower Calibration Algorithm

The shower counter was calibrated with the deep inelastic scattering data collected during the experiment. Runs which were selected for use in the calibration were examined spill by spill. Every trigger within a spill which was a Main Trigger was searched for electron cluster candidates by first looking for a block having more energy than its eight nearest neighbors, using preliminary calibration values for each block. Then a total energy for the cluster was formed by summing up the energy of the nine blocks. If a track was found pointing to the cluster, then the ratio of energy, E, to momentum, p, was accumulated in a histogram for the central block if this block received more than 65% of the total energy of the cluster. Separate histograms were kept for each trigger since the calibration constants were expected to vary slightly from trigger to trigger for each block. At the end of the run the histograms were fitted with Gaussians and the the calibration constant for each trigger of each block was divided by the mean value of the fit in order to center E/p on 1. This process was repeated until the calibration constants changed by less than 1% between iterations.

Improved Cluster Identification

Following the initial energy calibration of the shower counter we implemented a slightly more sophisticated technique to recognize clusters in the lead glass calorimeter. The reasons behind this were to improve our ability to separate partially overlapping clusters, and to accommodate the fewer than 5% of all electron clusters in which the cluster spread beyond a central block and its eight nearest neighbors. GEANT simulations suggest that in the sixteen blocks surrounding the core of nine blocks, <0.5 GeV would be deposited, and from the data we observed an average of 0.6 GeV [98]. In an effort to recover this lost energy the following cluster recognition algorithm was employed [98]:

1 Consider any block (called the peak block) which has more energy than any of its eight nearest neighbors and associate it with it them to form a cluster.

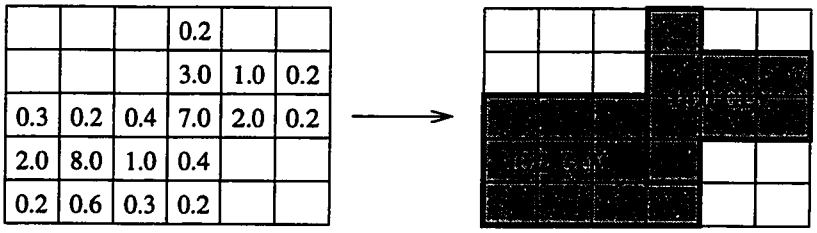

Figure 3.7: The left figure shows the energy deposited in 30 blocks of the calorimeter. Applying the clustering algorithm identifies the two clusters seen on the right.

A block which neighbors two peak blocks is associated with the cluster of the higher energy peak block.

2 Examine the sixteen next nearest neighbors of each peak block. If any of these sixteen blocks have non-zero energy and are not already associated with a cluster, then they join the cluster of the peak block.

An example of the clustering algorithm is shown in Figure 3.7. Blocks with less than 200 MeV of energy deposited are ignored in this algorithm.

Systematic Effects in the Shower Counter

The clustering and tracking routines used initially to calibrate the shower counter were different from those used in the final analysis of the data. For internal consistency, a second set of calibration coefficients were derived using a consistent set of tracking and clustering routines. During the recalibration, a systematic dependence of the E/p ratio on the position of the electron hit within a block was addressed. The effect is seen in Figure 3.8 and has been reproduced with moderate success in GEANT [99].

Two mechanisms are thought to be at work to produce this effect, and both are caused by the 2 mm of black tape (which we can consider as graphite) and $\sim$ 2 mm of air separating the blocks. The first effect is related to the attenuation of Čerenkov light in the blocks and comes about when electrons hit close to the gaps. Many of the high energy electrons and positrons composing the initial stage of the shower will propagate in the gaps between the blocks without much additional showering,

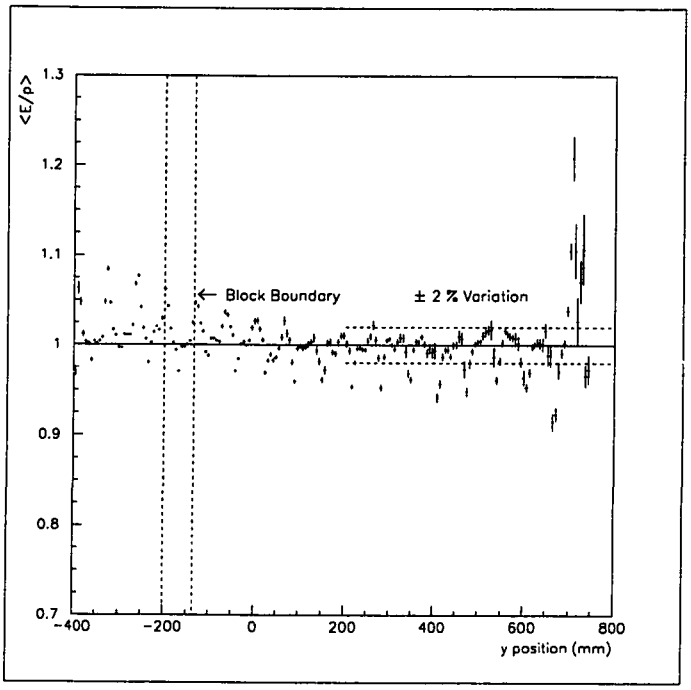

Figure 3.8: A systematic dependence of E/p upon the position of the hit in the lead glass calorimeter is seen in this plot. The peaks in E/p fall exactly on the boundaries between blocks.

and carry their energy deeper into the adjacent blocks before the shower resumes. The Čerenkov light from these particle is produced closer to the PMT and is more likely to be detected than had it been produced earlier in the block. The second effect is caused by a reduction in the energy detected when an electron hits near the center of a block. In this case, the low energy halo from the later stages of the shower is what is propagated from the central block to the adjacent ones. These electrons and positrons with energies of the order of a few MeV and below experience a large increase in critical energy (from 15 to $\sim$ 80 MeV) in the gap. Since they traverse the gap at shallow angles they see several cm of carbon and air and lose a large fraction of their energy from collisional losses and drop below the threshold to produce Čerenkov radiation [100, 101]. The energy of these particles is lost and we then underestimate the energy of the shower. Both effects conspire to make edge hits leave more detectable Čerenkov radiation in the cluster than central hits.

To treat these systematic effects we used two energy dependent corrections, with one applied to the energy in the central block to treat attenuation effects, and the

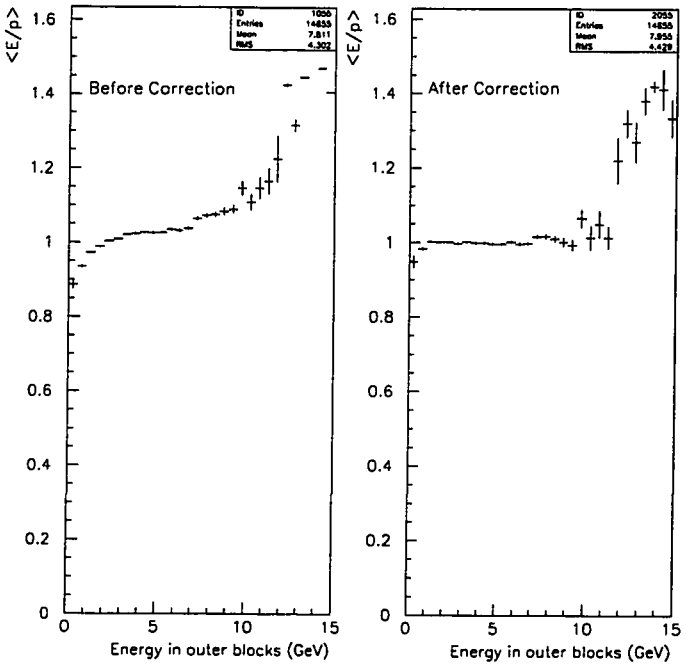

Figure 3.9: On the left we see the systematic rise in E/p as the energy deposited in the outer blocks increases (corresponding to the hit being closer to a block boundary), and the softening of the effect after the correction, on the right. The extreme behavior at high energies is due to overlapping clusters.

second applied to the total energy propagated to the surrounding blocks, accounting for attenuation and transition effects. The energy corrections took the form of cubic fits to the dependence of E/p on energy, the results of which are seen in Figures 3.9 and 3.10. The improvement in energy resolution is clearly visible in Figure 3.11 where we have plotted E/p for identical events with and without the energy correction. The reduced width of the distribution after correction indicates that the energy has been determined with greater accuracy. It is important to note that the treatment of these systematic effects did not cause us to cut or gain any data (except at the limits of our acceptance). The implication is that the asymmetry measurement is unaffected except for having improved our resolution in x.

Energy and Momentum Resolution

The energy resolution of the shower counter was measured in a test beam at CERN to be $dE/E=0.025+0.065/\sqrt{E}$ [102]. The momentum resolution is calculated from the

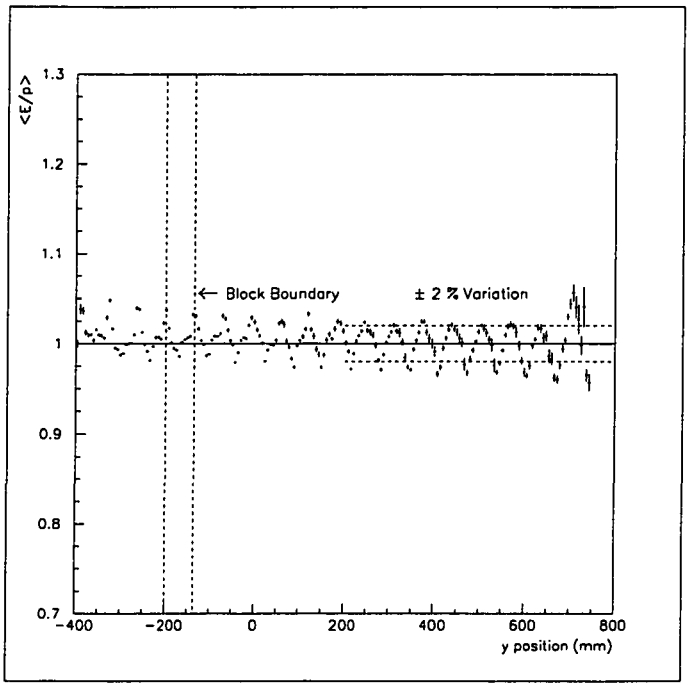

Figure 3.10: After implementing an energy dependent correction to the cluster energy, the large variation in E/p across block boundaries seen in Figure 3.8 has been reduced to a 2% effect.

angular resolution of 0.8 mrads in the hodoscope system coupled with the $dp/d\phi$ spectrum of electrons after passing through the magnets, seen in Figures 3.12 and 3.13.

In Figures 3.14 and 3.15 we show the expected momentum and energy resolution of our detectors, where the 0.3% intrinsic uncertainty in the momentum reconstruction as well as the effects due to multiple scattering are included. The momentum resolution is everywhere below 2.5% and is better than the shower counter energy resolution over thc whole range of our data. Also shown on the plot are the expected and observed width of E/p. The discrepancy between the two is due to errors in tracking, overlapping clusters distorting the energy measurement, and the effects of energy straggling as the electrons traverse about 0.1 radiation lengths of material in the target and detectors before reaching the calorimeter. These effects, and the residual systematic dependence of energy on hit position in the lead glass will contribute to a reduction in resolution. In Figures 3.16 and 3.17 we show the observed energy distribution of electron events in the 4.5° and 7.0° spectrometers. Marked on the plots are the scattered electron energies corresponding to the particular values of

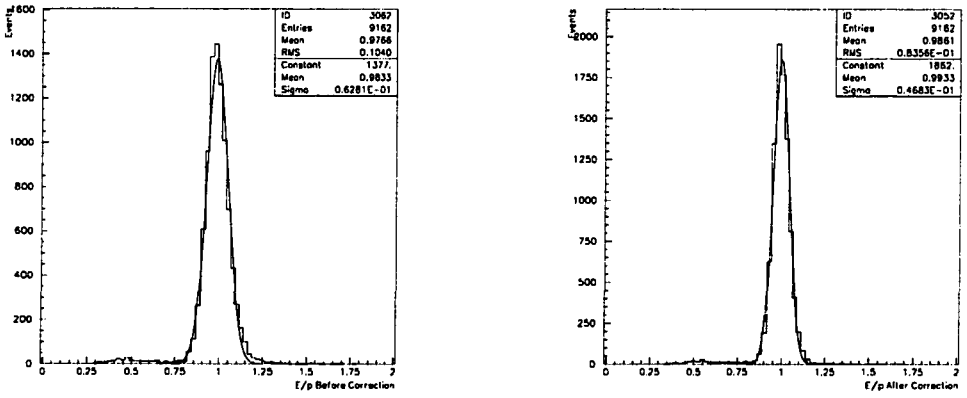

Figure 3.11: The ratio E/p is plotted on the left for a sample of electron events, and fitted with a Gaussian. On the right, an energy correction is applied to the same events which mitigates the effects of the gaps between the shower blocks. The resulting E/p spectrum is narrower, indicating that the energy has been measured more accurately.

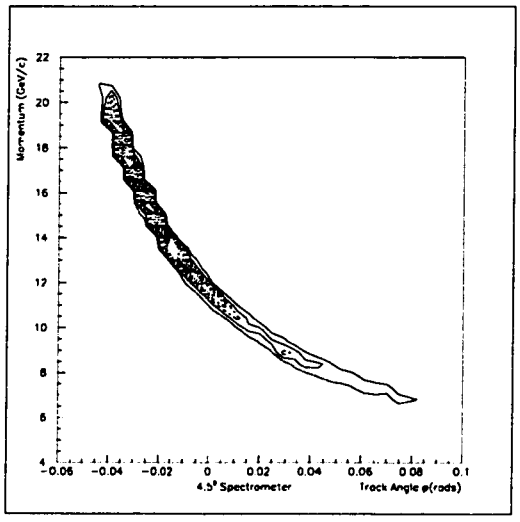

Figure 3.12: This figure shows the momentum dispersion of the tracks after having passed through the 4.5° spectrometer magnets at a central momentum setting of 11.5 GeV/c. The best momentum resolution occurs at low E′ where $dp/d\phi$ is smallest.

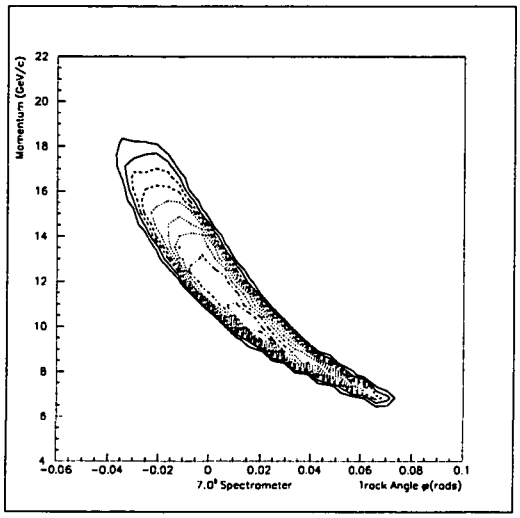

Figure 3.13: This figure shows the momentum dispersion of the tracks after having passed through the 7.0° spectrometer magnets at a central momentum setting of 12.5 GeV/c. The best momentum resolution occurs at low E′, as in the 4.5°.

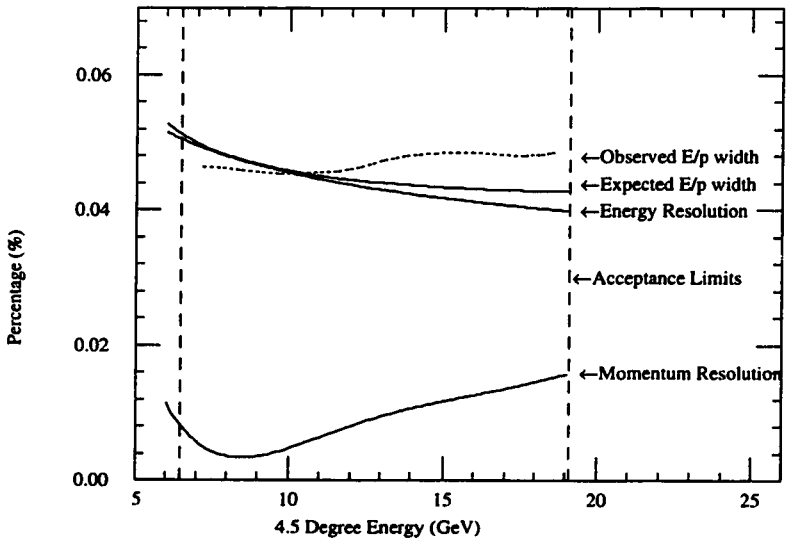

Figure 3.14: The momentum resolution of the hodoscope system at a central momentum setting of 11.5 GeV/c is shown with that expected from the shower counter. Our observed width of the ratio E/p is somewhat worse than that predicted using simple models of the detectors' response, but adequate for our measurement.

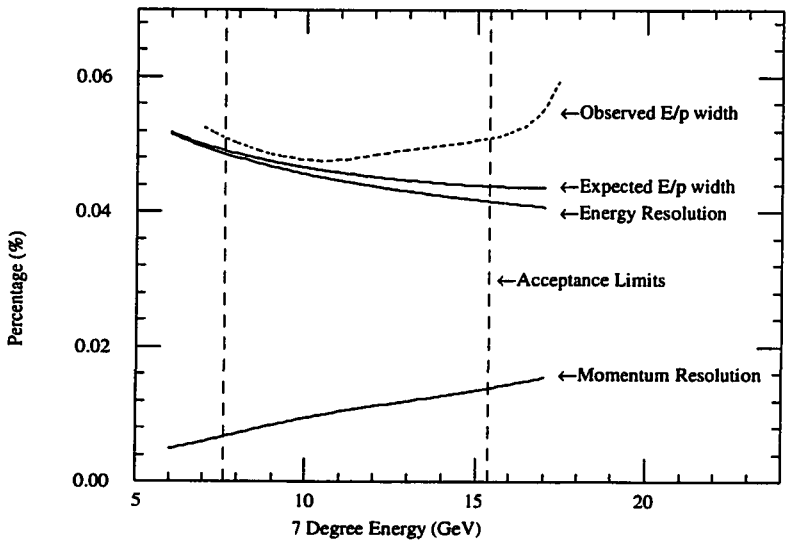

Figure 3.15: The momentum resolution of the hodoscope system at a central momentum setting of 12.5 GeV/c is shown with that expected from the shower counter. The expected and observed width of the ratio E/p is also plotted.

Bjorken x defining the x bins used in our analysis. We will use data from the 4.5° spectrometer coming from x=0.03 up to x=0.4. The 7.0° data will be taken from x=0.06 to x=0.6. It is seen that these x bins are at least 1 GeV wide, so all that is required is energy resolution of a similar order. The observed energy resolution of the shower counter is then seen to be quite adequate for this experiment.

3.5.4 Neural Network for Particle Identification

A neural network was employed to help distinguish pions from electrons in the shower counter for systematic studies [103]. Essentially, the neural network combines attributes of a cluster in the shower counter in a non-linear manner to yield a figure of merit between -1 and +1, where +1 corresponds to a high probability that the cluster was made by an electron, -1 to a pion. Typically electrons would yield a neural network response > 0.95, and pions < -0.5.

Attributes of the cluster which were important for distinguishing pions from electrons include the total energy of the cluster, the total number of blocks hit in the cluster, the ratio of energy in the peak block (highest energy block) to that in the

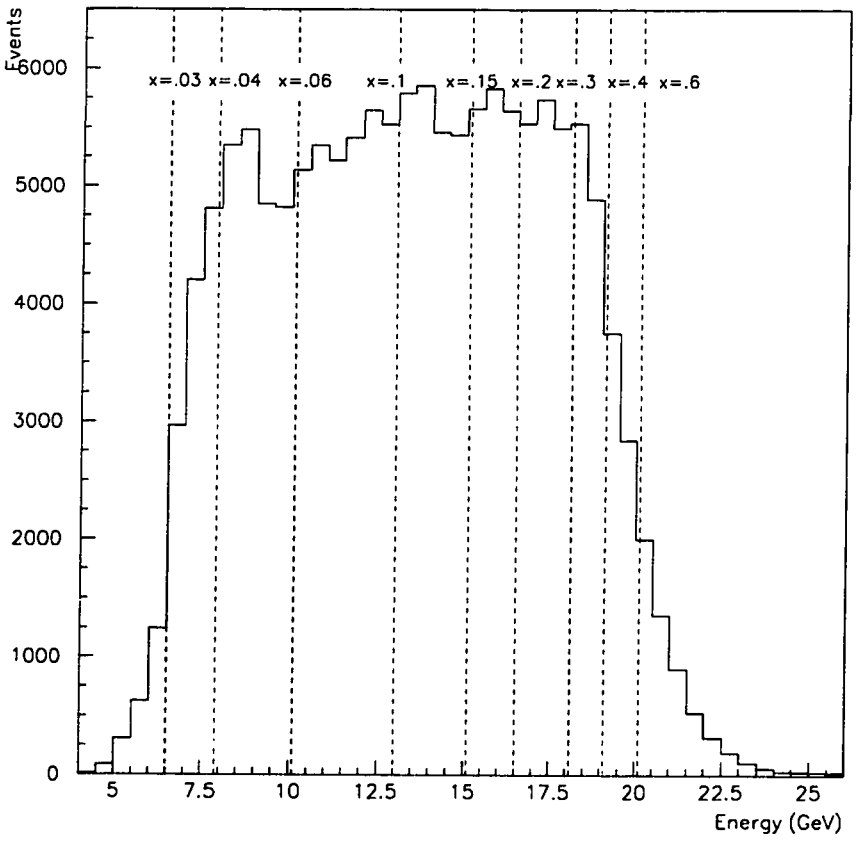

Figure 3.16: The energy distribution of electrons scattered into the 4.5° spectrometer during a run is plotted, along with the corresponding values of Bjorken x. The incident beam energy was 22.66 GeV/c^2.

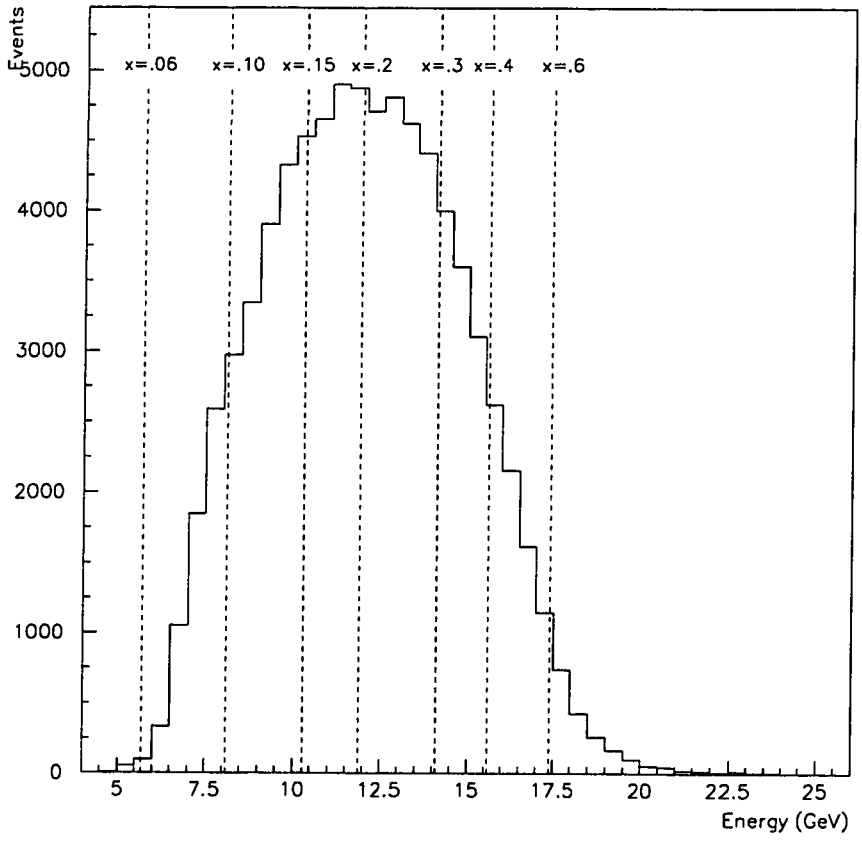

Figure 3.17: The energy distribution of electrons scattered into the 7.0° spectrometer during a run is plotted, along with the corresponding values of Bjorken x. The incident beam energy was 22.66 GeV/c^2

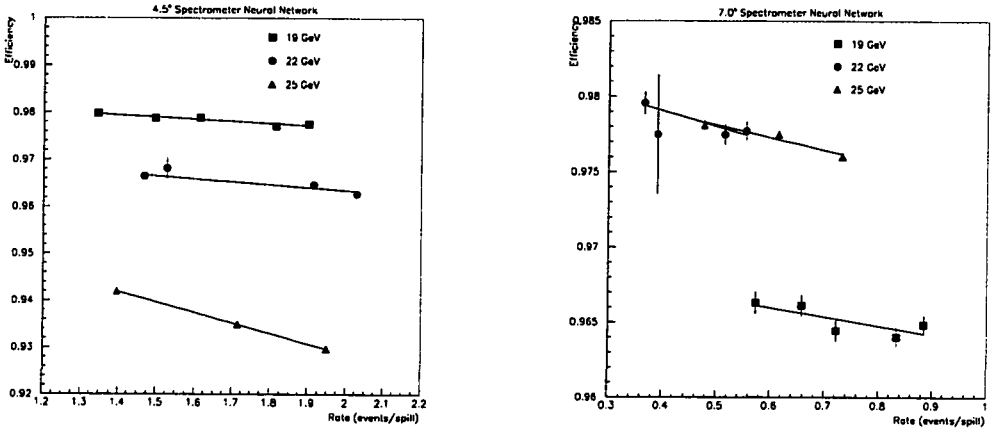

Figure 3.18: The electron identification efficiency of the neural network versus rate is plotted for the 4.5° spectrometer on the left, and for the 7.0° on the right for the three incident beam energies, averaged over all cluster energies. The small rate dependence seen would bias the overall measured asymmetry by less than 5% on average, however the rate dependence was worse at lower cluster energies, precisely where the pion/electron separation must be made.

3×3 array of blocks containing the peak block, and the total energy deposited in the 16 next-to-nearest neighbors of the peak block. Pion clusters have their energy spread out more evenly and over more blocks than electron clusters, so an electron cluster overlapped by another cluster will tend to look like a pion cluster.

While electron identification with the neural network was an excellent tool for systematic studies, it is not obvious that it is suitable for an asymmetry measurement. Since differentiating between pions and electrons depends heavily on the activity in the 16 next-to-nearest neighbors of the peak block, the neural network is sensitive to background rates. If the background has a spin dependence, we will accept or reject clusters in a spin dependent manner, and certainly in a rate dependent manner since we have more overlapping clusters at higher rates. To test the magnitude of these effects a plot of the neural network rate dependence is shown in figure 3.18; it is seen to be small. The next issue to address is whether the neural network is necessary. Distinguishing pions from electrons is most important in the x=0.035 bin of the 4.5° spectrometer where the possibility of misidentifying pions as electrons is highest. For

these low energy clusters, cutting on a neural network response > 0.95 yields an almost pure sample of electrons, but it also rejects a large number of good electrons. Using equation (3.6) we estimated the uncertainty in the electron asymmetry determined with and without a neural network used cut to identify electrons. The results showed that higher electron statistics (albeit with greater pion contamination) was preferred over a more pure, but smaller sample of electrons passing a neural network cut. On these grounds, the neural network was not used to identify electrons for the asymmetry analysis.

3.5.5 Final Event Selection

We now list the procedure followed to identify electrons for our asymmetry measurement.

1 Runs were selected in which the beam, target and detectors were all observed to be stable.

2 Within these good runs, spills in which the beam passed simple cuts on quality were further examined for electron candidates.

3 The data taken during each of these good spills were examined for evidence that the Main Trigger had fired, indicating that an electron may have entered the spectrometer. Each spectrometer was handled separately at this point since they were triggered separately.

4 For each Main Trigger found within a good spill, the two Čerenkovs were checked to see if the ADC values were greater than 25, which was true about 99.5% of the time.

5 The ADCs of the shower which were gated during the trigger were then examined for clusters.

6 Clusters which were centered on the outer blocks of the calorimeter and which may not have been fully contained were dropped from further analysis.

7 'Ghost' clusters were also dropped from further analysis. These were false clusters which appeared when a second electron event came more than 30 ns later

than a previous event, but less than 100 ns later. In these cases, the second electron would cause a second trigger to be issued, so the ADCs of the shower counter were gated. However, the second gate would enclose some of the energy of the first electron and it would appear as if a low energy electron had hit during the second gate. These ghost clusters were excluded from the analysis.

8 Clusters which were affected by malfunctioning shower blocks (there were three) were dropped from further analysis since we couldn't determine the cluster energy accurately for these events.

9 Of any remaining clusters the highest energy cluster was taken as our electron candidate. This cluster had to have a energy, E', greater than 5.5 GeV.

10 The position of the cluster within the calorimeter was used to determine the scattering angle, θ, of the event.

11 The event was binned in E' bins 0.5 GeV wide and θ bins which were 3.65 mrads wide in the 4.5° spectrometer, and 6.5 mrads wide in the 7.0° spectrometer.

12 After binning the event the next trigger or spill was processed. Once all of the spills in a run had been processed a summary file was written out, and the next run was analyzed.

We note that a maximum of one electron event was selected from each Main Trigger. Occasionally there were two electrons within a single trigger so the above algorithm will fail, but the correction for this effect is straightforward.

Despite its simplicity the algorithm described above for event reconstruction was perfectly adequate since the cluster of the electron causing the Main Trigger was usually trivial to find in the calorimeter. Clusters caused by pions entering the spectrometer at the same time were easily separated since pions deposit much less energy in the calorimeter and only rarely more than 5.5 GeV. Taking the highest energy cluster almost guaranteed that the electron would be selected whenever both a pion and electron cluster appeared in the calorimeter at the same time. In Figure 3.19 we demonstrate the effectiveness of this algorithm.

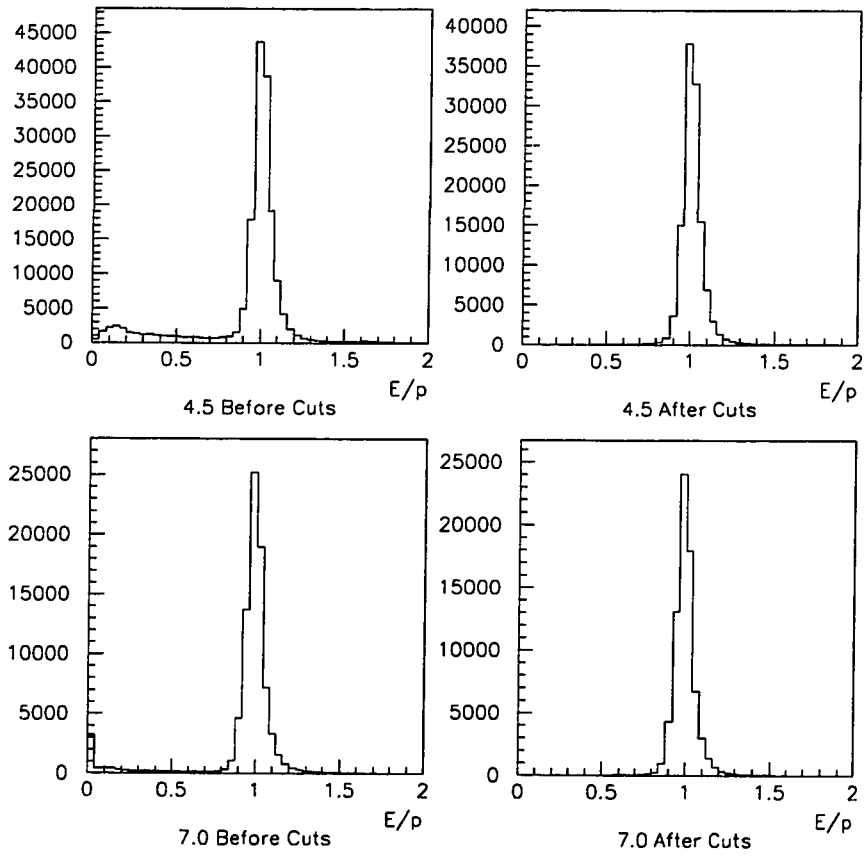

Figure 3.19: In the plots on the left we show the ratio E/p of events detected in the shower counters of the 4.5° and 7.0° spectrometers. The electrons are visible as a peak centered around E/p=1, whereas the pions, which deposit much less energy in the calorimeter, are visible as a tail at values of E/p<0.8. By selecting the highest energy clusters and requiring a Main Trigger, we get the event sample seen in the right hand plots, which is a > 99% pure sample of electrons. These are the events used in our analysis.

3.6 Asymmetry Analysis

Once the tapes had been spun through, the summary files were used to extract the asymmetry, $A_1^{^3He}(x, Q^2)$. The starting point was the raw counting rate asymmetry, $A_{\|}^{raw}$, which was extracted from every run in each spectrometer separately :

$$A_{\|}^{raw}(x) = \frac{N_{1/2}(x)/Q_{1/2} - N_{3/2}(x)/Q_{3/2}}{N_{1/2}(x)/Q_{1/2} + N_{3/2}(x)/Q_{3/2}} \tag{3.2}$$

where N(x)/Q is the number of events passing our cuts normalized by incident charge, with Bjorken x being determined from the E′ and θ of the events. The subscript 1/2 refers to data taken with antiparallel beam and target spins, and 3/2 to parallel beam and target spins.

The raw asymmetry in (3.2) must undergo many corrections before it can be interpreted as $A_1^{^3He}(x)$. First, not all of the events which pass our cuts are the DIS electrons in which we are interested, so a background subtraction must be performed. We will write the raw counting rate asymmetry for these DIS electrons as $A_{\|}^{raw\ e^-}$. Second, the electron beam and target were not 100% polarized, and further, not all of the events coming from the target came from scattering off of ^{3}He since a large fraction came from the glass endcaps. Correcting for these effects, we can write a more meaningful asymmetry

$$A_{\|}^{e^-} = \frac{A_{\|}^{raw\ e^-}}{P_b P_t f} \tag{3.3}$$

where P_b is the beam polarization, P_t is the target polarization and f, the dilution factor, is the fraction of all events originating from scattering off of ^{3}He. This asymmetry is still not in a form that enables us to extract any physics results. A resolution correction must first be applied to account for the fact that we cannot measure the energy of the scattered electrons perfectly. Also, effects due to deadtime in the electronics will bias the measured asymmetry and must be corrected for. Another complication to be considered before we can get extract $A_1^{^3He}$ is that the DIS electrons we detect are not all the result of the single virtual photon exchange process we would like to determine, so radiative corrections must be made to the measured results. Finally, there is a small contribution from the transverse asymmetry, $A_\perp$ which enters into $A_1^{^3He}$. The final expression we will use to go from the raw asymmetry to $A_1^{^3He}$ takes

the form :

$$A_1^{^3\mathrm{He}} = \frac{1}{D(1+\eta\zeta)}\left[\frac{(A_{\|}^{\mathrm{rawe}^-} + \Delta_{dt})}{P_b P_t f}\right] + \Delta_{RC} - \frac{\eta}{d(1+\eta\zeta)}\left[\frac{(A_{\perp}^{\mathrm{rawe}^-} + \Delta_{dt})}{P_b P_t f}\right]. \quad (3.4)$$

where Δ_{dt} is the deadtime correction, and Δ_{RC} are the radiative corrections. The remaining kinematic factors η, ζ, D and d were discussed in Chapter 1.

We will now examine each of the corrections in greater detail.

3.6.1 Resolution Correction

Our calorimeter has a finite energy resolution so an electron of energy E_{true} will usually appear with a slightly different energy, E_{obs}. If we systematically mismeasure the energy then events will be placed in the wrong Bjorken x bins, and the kinematic factors will be evaluated incorrectly.

The range in energy of the detected electrons is determined at low energy by the spectrometer acceptance and at high energy by the steep decrease in cross section. In our low energy bins are many higher energy particles which have leaked down due to fluctuations in the calorimeter response. Since there is no compensating influx of lower energy events (due to the spectrometer acceptance cutoff) we expect that at low energies we systematically underestimate the energy of the electrons. The converse is true for the highest energy electrons we detect. Given an estimate of the true energy spectrum of detected electrons, $F(E)$, and the shower counter energy resolution, $\delta(E)$, we can calculate the correction factor to be applied to electrons of observed energy E_{obs} :

$$\frac{E_{\mathrm{true}}}{E_{\mathrm{obs}}} = \frac{\int_{E_{min}}^{E_{max}} EF(E)\exp\left[-\frac{1}{2}\left(\frac{E-E_{\mathrm{obs}}}{\delta(E)}\right)^2\right]dE/\sqrt{2\pi}\delta(E)}{\int_{E_{min}}^{E_{max}} E_{\mathrm{obs}}F(E)\exp\left[-\frac{1}{2}\left(\frac{E-E_{\mathrm{obs}}}{\delta(E)}\right)^2\right]dE/\sqrt{2\pi}\delta(E)} \quad (3.5)$$

where the limits of integration are determined by our acceptance. The results of this calculation are shown in Figure 3.20. As a test of our understanding of the resolution we can take a model of the true electron energy spectrum and by folding in the finite energy resolution of the shower counter, make a prediction for the observed energy

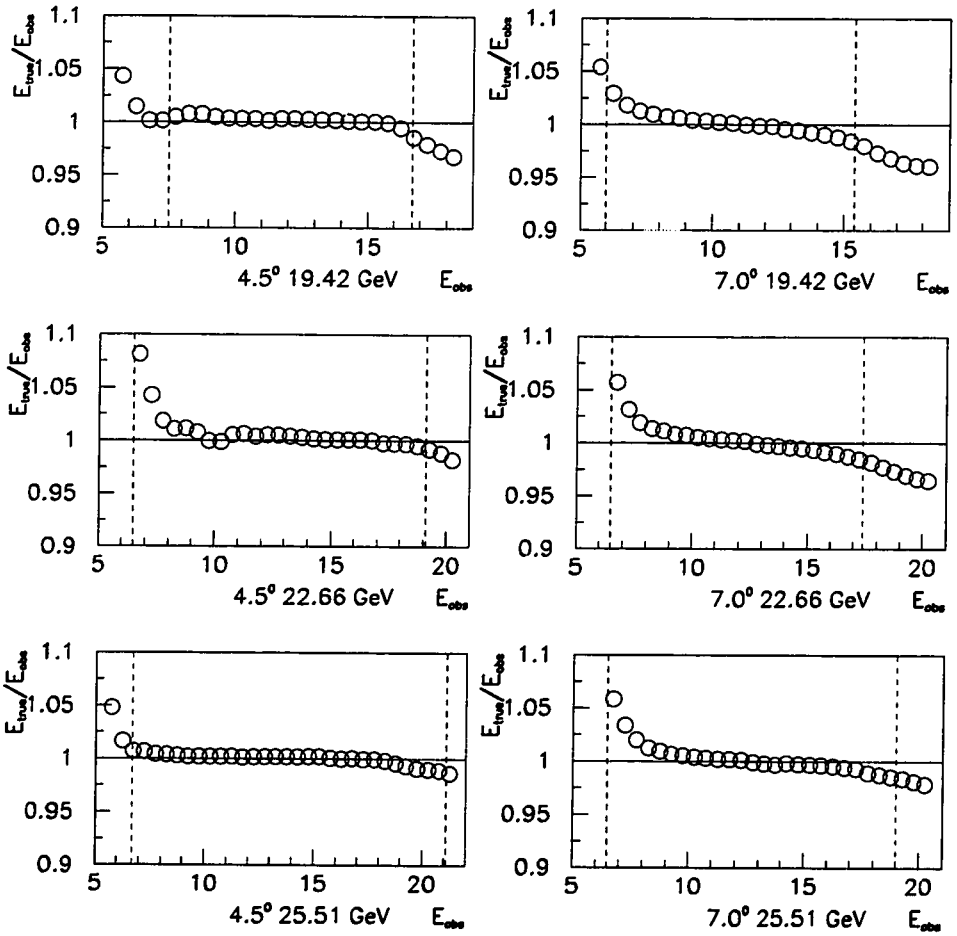

Figure 3.20: The plots show the ratio of true energy to observed energy for the six spectrometer settings of E142. We use dashed lines to indicate the range of electron energies used in the analysis, which shows that the resolution correction has little impact except on about 15% of the 4.5 low x data where the electron energies are modified by 4-8%, and in the low energy region of the 7.0° spectrometer. The wiggle in the 4.5° data around 9 GeV is due to a region of reduced efficiency in the calorimeter which was fixed before we went to a beam energy of 25 GeV.

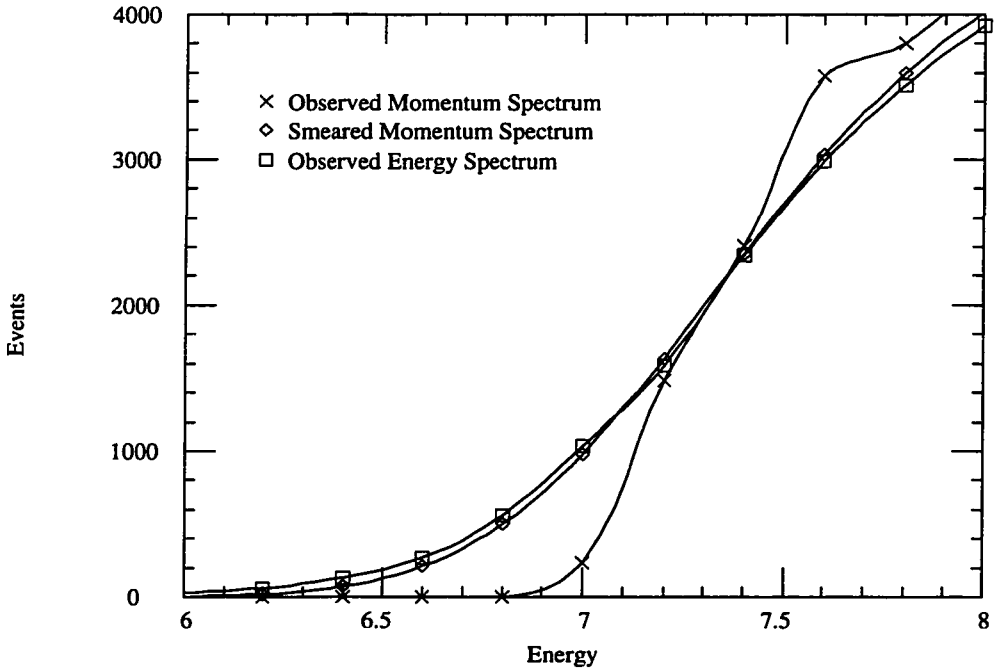

Figure 3.21: This plot shows the effects of finite shower counter energy resolution on the observed energy spectrum. The true energy spectrum is determined from the momentum spectrum of electrons returned by our hodoscope tracking system. For these low energies, the momentum resolution is at or below 1% and so provides a good model of the true energy spectrum. Taking the same events, and accounting for energy smearing in the calorimeter we can predict the energy spectrum for the same events in the shower counter. The prediction compares favorably with the observed spectrum.

spectrum. An example of the results of such a test is shown in Figure 3.21. In the analysis of the asymmetry we account for the shower resolution effects by scaling the observed energy, E′, by the ratio determined in (3.5) above, and use this corrected energy to determine the value of Bjorken x. This has essentially no impact except on the first x bins used in each of the 4.5° and 7.0° spectrometers.

3.6.2 Backgrounds

The events passing our cuts and used to form the asymmetry are not a pure sample of deep inelastically scattered (DIS) electrons, so our expression (3.2) for the total counting rate asymmetry must be modified to extract the DIS electron counting rate asymmetry. Some of the electrons we detect have their origin in charge symmetric processes such as $\pi^0 \rightarrow 2\gamma \rightarrow e^+e^-e^+e^-$, where the π^0 are photoproduced in the target. Furthermore, charged pions and at a lesser rate kaons and muons, entered our detectors and occasionally were misidentified as electrons. Any spin dependence in these background event rates will corrupt our measurement directly, and at a minimum will dilute the DIS electron asymmetry. Denoting the event rates, summed over polarization, of DIS electrons by e^-, of electrons from charge symmetric processes by e^+, and of the hadronic and other backgrounds by π^-, we can decompose the total measured asymmetry in event rate, $A_{||}^{\rm raw}(x)$ as :

$$A_{||}^{\rm raw} = A_{||}^{{\rm raw}\ e^-}\left(\frac{e^-}{e^- + e^+ + \pi^-}\right) + A_{||}^{{\rm raw}\ e^+}\left(\frac{e^+}{e^- + e^+ + \pi^-}\right) + A_{||}^{{\rm raw}\ \pi^-}\left(\frac{\pi^-}{e^- + e^+ + \pi^-}\right) \tag{3.6}$$

where we have suppressed the x dependence and $A_{||}^{{\rm raw}i}$ is the asymmetry in event rate from the ith particle type. In order to extract $A_{||}^{{\rm raw}\ e^-}(x)$ from the measured asymmetry, $A_{||}^{\rm raw}(x)$, we require measurements of the other quantities.

3.6.3 Pion Background

The number of π^- misidentified as electrons in our analysis was estimated by examining the E/p spectra of our events. The fraction of events with E/p<0.8 was taken to be the contamination ratio $\pi^-/(e^- + e^+ + \pi^-)$ and used in (3.6). The part of the pion spectrum having E/p>0.8 and the tail of the electron spectrum with E/p<0.8

Beam Energy	x=0.035	x=0.050	x=0.080
22.66 GeV	0.030 ± 15%	0.014 ± 15%	0.007 ± 15%
25.51 GeV	0.031 ± 15%	0.018 ± 15%	0.008 ± 15%

Table 3.4: Fraction of pions $\pi^-/(e^- + e^+ + \pi^-)$ misidentified as electrons in the 4.5° spectrometer.

were roughly equal and canceled. In Table 3.4 we list the contamination ratio for the x bins in the 4.5° spectrometer most affected by the pion background. In the remaining x bins of the 4.5° the contamination was less than 0.5%. The 7.0° spectrometer was affected by pions only in the first x bin used, x=0.08, where the average pion contamination was estimated as 1.5%. In the remaining bins the background was well below 1%.

These background rates were confirmed with a second approach employing stringent cuts on particle identification characteristics to identify a sample of electron and pions, independently of any E/p information. These contamination rates, estimated using particles of which we were quite certain of their identity, deviated from the first by $\leq$15%, which we take as our uncertainty.

Apart from diluting the electron asymmetry, misidentified pions can introduce a new asymmetry into the data, $A^{\pi^-}(x)$. This asymmetry was measured using the Pion Or trigger; fired by a triple coincidence of the two planes of lucite and one plane of hodoscopes. Any charged particle will fire the Pion Or, so to reduce the electron background it was required that the Main Trigger not fire in coincidence. Pions were identified by requiring a track pointing to a cluster having a neural network response <-0.5, which was a good indicator that the particle was a pion. Using the momentum returned from the track to determine Bjorken x, the asymmetry results are shown in Figure 3.22. The average asymmetry of the subset of pions depositing enough energy in the calorimeter to be mistaken for an electron, $E_\pi > 5.5$ GeV, was $\langle A_\parallel^{\pi^-} \rangle = 0.031 \pm 0.032$. This result is consistent with zero, and implies that the small fraction of misidentified pions does not carry a significant bias into our electron asymmetry measurement. While there are no theoretical reasons for the pion asymmetry to be exactly zero (certainly for electroproduced pions the asymmetry will be non-zero), we will use $A_\parallel^{\mathrm{raw}\ \pi^-}(x) = 0$ in (3.6), since it is consistent with the data,

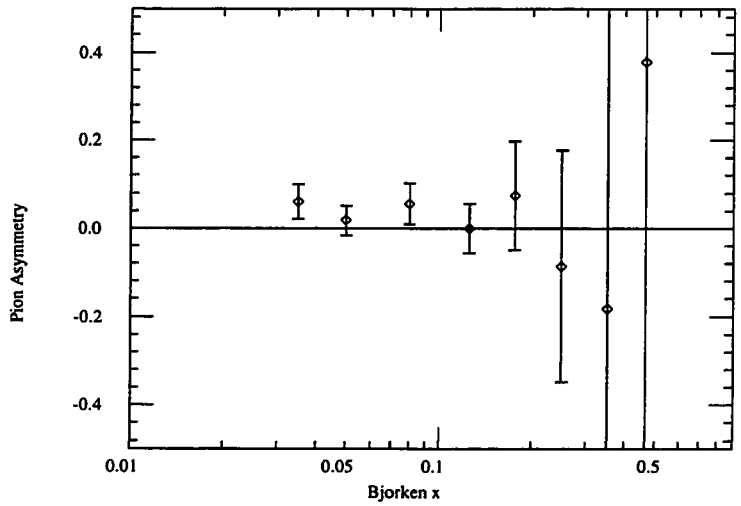

Figure 3.22: A plot of $A_{||}^{\pi^-}(x) = A_{||}^{\text{raw }\pi^-}/(P_b P_t f)$ where $A_{||}^{\text{raw }\pi^-}$ where is the raw counting rate asymmetry of pions, P_b and P_t are the beam and target polarizations, and f is the ^{3}He dilution factor. The asymmetry shown has been corrected for electronic deadtime and is consistent with zero ($\chi 2/df = 0.6$).

and allows us to avoid introducing the statistical fluctuations of the pion asymmetry measurement into our determination of the electron asymmetry. The uncertainty in the pion asymmetry measurement will be taken as a systematic error in our final results.

3.6.4 Charge Symmetric Background

The event rate of electrons coming from charge symmetric processes was determined by reversing the spectrometer magnets' polarities. This allowed the positron component of the background into our detectors at the same rate that electrons would enter under normal magnet polarities.

A total of nine runs was taken, including six using the polarized target, to measure e^+ and $A_{||}^{\text{raw }e^+}(x)$. The ratio $e^+(x)/(e^+(x)+e^-(x))$ extracted, shown in Figure 3.23, was substituted in (3.6). The largest contamination rate is in the $x = 0.035$ bin of our 25.5 GeV data set. Here the rate from charge symmetric processes is 7% of the DIS electron rate. In all other bins used the rate is less than 3.2%.

In Figure 3.24 we show the results of our measurement of $A_{||}^{e^+}$. This was extracted

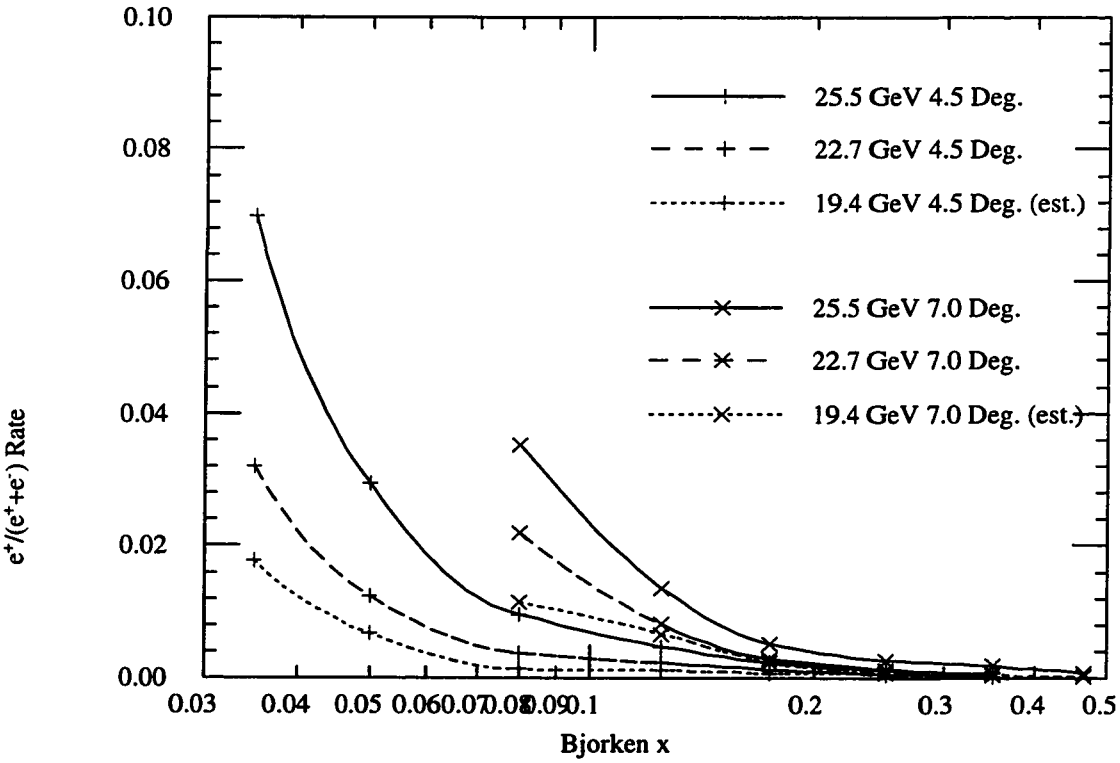

Figure 3.23: The background ratio $e^+(x)/(e^+(x) + e^-(x))$ from charge symmetric processes is shown for the two spectrometers and three beam energies used in E142. No positron data were taken during our short run at 19 GeV, so the background rate was estimated by scaling the data at 22.7 and 25.5 GeV beam energies as 25.5 : 22.7 $\approx$ 22.7 : 19.4. The uncertainty in the ratio ranges from 5% at low x to 25% at high x.

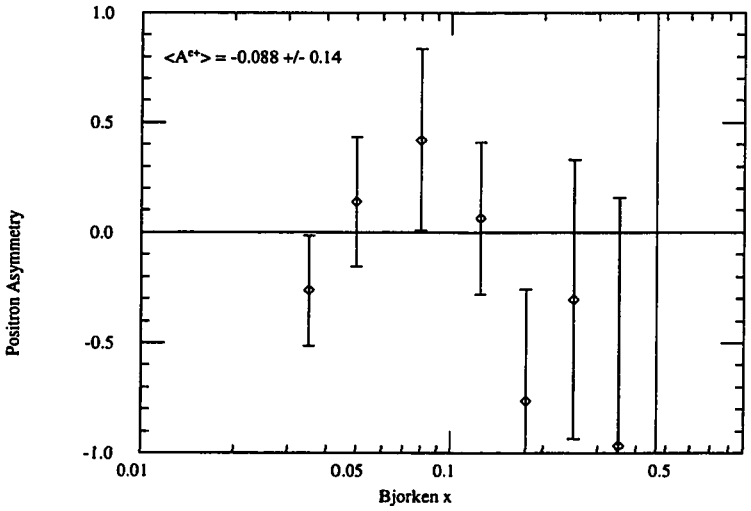

Figure 3.24: The asymmetry in the positron background is shown, where we have defined $A_{||}^{e^+} = A_{||}^{\text{raw } e^+}/(P_b P_t f)$ where $A_{||}^{\text{raw } e^+}$ is the raw positron counting rate asymmetry, P_b and P_t are the beam and target polarizations, and f is the ^{3}He dilution factor. The asymmetry is consistent with zero ($\chi^2 = 5.9$ for 8 degrees of freedom).

using identical event selection as in the electron asymmetry extraction, with the addition of a neural network cut to reduce the potentially large π^+ contamination in our event sample[1]. The average asymmetry, $\langle A_{||}^{e^+} \rangle = -0.088 \pm 0.14$ is consistent with zero so we substitute $A_{||}^{\text{raw } e^+}(x) = 0$ into (3.6). It would be surprising if this asymmetry were much larger than the charged pion asymmetry, so we will assign the same uncertainty, $\delta A_{||}^{e^+} = \delta A_{||}^{\pi^-}$ when calculating systematic errors due to this background.

3.6.5 Deadtime Correction

From the measurements of the backgrounds we can solve (3.6) for $A_{||}^{\text{raw } e^-}(x)$. Still, this is not the "true" counting rate asymmetry for DIS electrons. Two characteristics of the electronics introduce small biases into the measured raw asymmetry. The first, called the ">4 correction", occurs because we were limited to recording a maximum of 4 events/spill/spectrometer. Since the left and right handed electron scattering rates

[1]When running with the magnet polarities reversed, the π^+ and e^+ rates are comparable, so additional cuts are needed to remove the pions.

are different, we lose a larger fraction of events from one polarization state than the other. A second bias is introduced due to deadtime effects in the trigger electronics. An event falling < 32 ns after a previous event will not cause a second trigger to be issued. Since we accept only one event per trigger in our analysis, then we expect the measured asymmetry to be biased because different fractions of events are lost from each helicity configuration. Accepting only one event per trigger makes it easier to correct for deadtime effects in the electronics since this effectively allows us to define the limiting deadtime.

Analytic corrections to the two effects are nearly impossible to achieve due to some complicating factors. Firstly, the electronics deadtime was not strictly 32 ns, but varied according to the timing precision achieved for the particular lead glass blocks hit in the event (so we should properly write 32 ± 5 ns). Secondly, the electron intensity incident on the target was not uniform within the spill but exhibited a finite risetime and falltime, as well as 10% variations in intensity within the nominally flat part of the spill. A final complicating factor occurs because not only was the charge intensity not constant within a spill, but it varied from spill to spill. Periods with high incident charge are more affected by deadtime effects than low charge periods. These effects are highly specific to this experiment and cannot be treated easily in full generality. Analytic calculations thus are of limited utility, instead serving as benchmarks for detailed modeling.

Before calculating the deadtime correction we note that since we could register the times of up to 16 Main Or triggers per spill, the trigger distribution observed in the TDCs is unaffected by the >4 correction, and is only affected by the electronic deadtime. Ultimately, however, we are interested in the loss of events, which is affected by both the deadtime and the >4 correction. Our approach then is to first determine the loss in triggers due to deadtime and from this calculate the loss in events.

To formulate a correction to the asymmetry one should be able to start with a Poisson distribution of triggers per spill, simulate the losses due to deadtime and replicate the observed distribution of triggers. Since the probability of having zero triggers in a spill is independent of electronic losses, it can be used to estimate the true rate. Taking into account the spill to spill variation of the charge within a run,

we can write the probability of zero triggers per spill as

$$P(0) = \int_{Q_{min}}^{Q_{max}} F(Q) e^{-\alpha Q} dQ \tag{3.7}$$

where F(Q) is the normalized fraction of spills within the run having charge Q incident on the target, $P(n)$ is the observed fraction of spills having n events, and α is the proportionality constant we seek relating incident charge to numbers of triggers. Using the charge distribution accepted during a run and solving for α, we can then estimate the ratio of true to observed event rates, R, as

$$\begin{aligned} R &= \text{True Rate / Observed Rate} && (3.8)\\ &= \sum_{n=0}^{\infty} \int_{Q_{min}}^{Q_{max}} nF(Q) e^{-\alpha Q} (\alpha Q)^n dQ/n! \Big/ \sum_{n=0}^{4} nP(n) && (3.9)\\ &= \int_{Q_{min}}^{Q_{max}} F(Q) \alpha Q dQ \Big/ \sum_{n=0}^{4} nP(n); \quad \text{where} \quad \sum_{n=0}^{4} P(n) = 1. && (3.10) \end{aligned}$$

The precision of this result is limited by the statistical uncertainty of $P(0)$ which was typically $\approx \pm$ 0.1%. To take advantage of the full statistics of the run, we then examined small variations of the parameter α. Starting from a Poisson distribution of triggers whose mean is determined by our choice of α, we simulated the effects of the electronics on twenty million spills to predict an observed distribution of triggers per spill, for every run. The triggers were chosen in a manner consistent with the distribution of charge/spill incident during the run and with the temporal variations of beam intensity observed within single spills. This prediction for the trigger distribution was then compared with the observed distribution, and α was optimized to minimize this difference. In all cases, the final value for α derived from the Monte Carlo differed by less than 1% from the original estimate using only $P(0)$. The results of the simulation for a single run are show in Figure 3.25. With knowledge of the mechanisms by which events are lost, and their rate dependence, we can calculate the ratio of true to observed event rates, R, for every run. R will be slightly different for $\sigma_{1/2}$ and $\sigma_{3/2}$ since the event rates are slightly different. Extracting $R_{1/2}$ and $R_{3/2}$ using the data and Monte Carlo for each run, and using these values in a deadtime correction suffers because the statistical errors on the $P(n)$ from each beam helicity are comparable in magnitude to the asymmetry, and so are inadequate for determining a correction to the asymmetry. Instead we consider the average unpolarized event

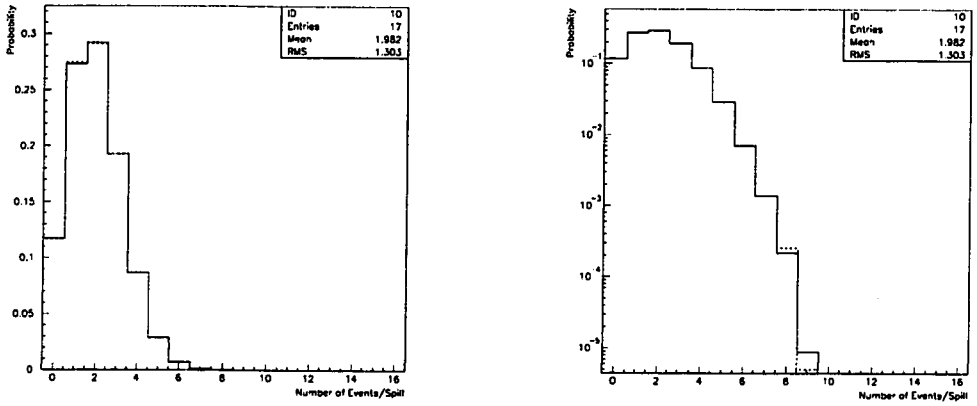

Figure 3.25: The solid histogram on the left shows the distribution of triggers/spill observed in the 4.5° spectrometer during a run. The dotted line is the prediction of the Monte Carlo which starts from a Poisson distribution of Main Or triggers using one free parameter and then simulates the losses in the electronics to yield an observed trigger distribution. The two histograms are consistent within statistical errors. The right hand plot shows the same distributions on a logarithmic scale.

rates. Barring pathologies, we can always write

$$\langle \text{ Observed Rate } \rangle = \sum_{n=1}^{\infty} \beta_n \langle \text{ True Rate } \rangle^n \tag{3.11}$$

where we denote the observed average unpolarized event rate by $\langle$ Observed Rate $\rangle$. The coefficients, β_n, are the same for each helicity configuration, and depend only on the spill structure during the run and characteristics of the electronics. In the case that $\beta_1 = 1$ and $\beta_{n>2} \approx 0$, then it is straightforward to show that the true and observed raw event rate asymmetries are related by

$$A_{\text{True}} = A_{\text{Observed}} \times \frac{\langle \text{ True Event Rate } \rangle}{\langle \text{ Observed Event Rate } \rangle} = A_{\text{Observed}} \times \langle R \rangle. \tag{3.12}$$

The conditions on β_n are satisfied for our experiment, as shown in Figure 3.26, so we can use (3.12) to estimate the effects of electronic losses on the asymmetry. In the 4.5° spectrometer a typical value for $\langle R \rangle$ is 1.10, meaning that 10% of both the events and asymmetry are lost in the electronics. In the 7.0° spectrometer this

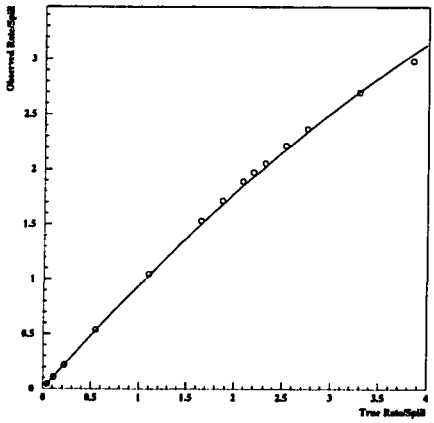

Figure 3.26: The open circles indicate the relationship between observed and true event rates, as determined by the Monte Carlo. The solid line, which is an approximation of the form Observed Rate=True Rate$\times$[1-$\beta_2\times$True Rate], is a reasonable model of the deadtime losses.

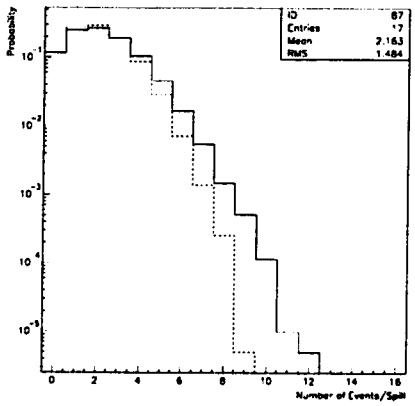

Figure 3.27: Here we show the distribution of triggers (solid line) before losses in the electronics are considered, and the distribution after electronic deadtime losses (dotted line). In this run roughly 9% of the triggers and 12% of the events were lost.

number is about 2.5%. For later convenience we rewrite the deadtime correction to the raw asymmetry, which is calculated separately for each run and spectrometer, as an additive quantity, Δ_{dt} :

$$A_{\text{True}} \equiv A_{\text{Observed}} + \Delta_{dt} \quad \text{where} \quad \Delta_{dt} = A_{\text{Observed}}(\langle R \rangle - 1). \tag{3.13}$$

The truncation of events beyond 4/spill reduces the statistical fluctuations observed of the overall asymmetry from that expected from Poisson statistics, but the effect is reasonably small and is ignored in this analysis. The values of Δ_{dt} averaged over the whole experiment were -3.7×10^{-5}±0.7×10^{-5} in the 4.5°, and -1.9×10^{-5}±0.4×10^{-5} in the 7.0°. To estimate our error we have used bounds on Δ_{dt} calculated using $R_{1/2}$ and $R_{3/2}$ determined strictly from the data, and also from a simple analytic computation. These deadtime corrections modify the raw counting rate asymmetries, which were roughly -3.7×10^{-4} in the 4.5° spectrometer, and -7.1×10^{-4} in the 7.0° spectrometer, by about 10% and 2.5% respectively.

One other factor must be computed before we can extract the electron asymmetry from ^{3}He :

$$A_{||}^{^3\text{He}}(x) = \frac{(A_{||}^{\text{rawe}^-} + \Delta_{dt})}{P_b P_t f}. \tag{3.14}$$

Here P_b is the beam polarization, and P_t is the target polarization. The dilution factor, f, is the subject of the next section.

3.6.6 Dilution Factor

Dilution Factor Theoretical Results

To extract g_1^n from the data we are required to know the fraction of all events which have originated from scattering off of polarized ^{3}He. Since the target polarization changes it is more useful to calculate for each target the constant fraction, $f_{^3\text{He}}(x, Q^2)$, of all events coming from *polarizable* ^{3}He. This number is $\approx 1/3$, where the remainder of the events have their origin in the glass endcaps, and from N_2 which comprises about 0.8% of the molecules in the target cell. Using the subscript H to signify ^{3}He, g for glass, and N for N_2, our dilution factor then takes the form :

$$f_H(x, Q^2) = \frac{n_H \sigma_H(x, Q^2)}{n_H \sigma_H(x, Q^2) + n_g \sigma_g(x, Q^2) + n_N \sigma_N(x, Q^2)} \tag{3.15}$$

where n_i is the total number of nucleons found in species i and σ_i is the average experimental cross section per nucleon :

$$\sigma_i(x,Q^2) = \frac{\mathrm{EMC}_i(x)}{A_i}\Big[Z_i\sigma_p(x,Q^2) + (A_i - Z_i)\sigma_n(x,Q^2)\Big] \tag{3.16}$$

where we have included the EMC effect using the parameterization given in [104]. Given that to within 1% the number of protons and neutrons is the same in the Corning 1720 glass of the target (which has the approximate composition 57% SiO_2, 20.5% Al_2O_3, 12% MgO, 5.5% CaO, 4% B_2O_3, 1% Na_2) we can rewrite the dilution factor as :

$$f_H(x,Q^2) = \frac{1}{1 + \frac{3(1+F_2^n/F_2^p)}{2(2+F_2^n/F_2^p)}\left[\frac{\mathrm{EMC}_q}{\mathrm{EMC}_H}\frac{RC_q}{RC_H}\frac{n_q}{n_H} + \frac{\mathrm{EMC}_N}{\mathrm{EMC}_H}\frac{RC_N}{RC_H}\frac{n_N}{n_H}\right]}. \tag{3.17}$$

where we have used the experimental result that the ratio of longitudinal to transverse cross sections, $R = \sigma_L/\sigma_T$ is the same for protons and neutrons, $R_p = R_n$ [105], so we can replace σ with F_2 provided we include radiative corrections to the cross section in the factor RC. The ratio F_2^n/F_2^p depends only weakly on Q^2 (the dependence is roughly $F_2^n/F_2^p \propto -0.0146\log(Q^2)$ [106]) so the only reason for the dilution factor to be different for the two spectrometers is that the radiative corrections are different. More details on F_2 and R are included in the next section.

The important parameters of the polarized targets used to calculate the dilution factor are given in Table 3.5.. The window thicknesses given in the table were measured with a dial-head indicator before the cells were assembled. As a consistency check, several windows from our reference cells were also measured using a coordinate measuring machine in the precision measurements shop at SLAC, verifying the accuracy of the indicator to 7.5%.

The dilution factor calculation for the three target cells is estimated to be accurate to 8%. Significant contributions to the uncertainty derive from a 7% uncertainty from the window thicknesses, 2% from uncertainty in the number density of the gases in the target, and 3% from the radiative corrections. Other contributions to the error from the EMC effect, and F_2 are negligible in comparison.

Parameter	Minnehaha	Hiawatha	Gore
Runs Used	1000-1117,1320-1771	1118-1181	1182-1319
Length (mm)	295±2	297±2	303±2
Front Window (μm)	110±7.5%	110±7.5%	110±7.5%
Rear Window (μm)	124±7.5%	107±7.5%	110±7.5%
Glass Density(g/cm^3)	2.52±1%	2.52±1%	2.52±1%
^{3}He Density(amagats)	8.63±2.5%	8.90±2.0%	8.74±2.0%
N_2 Density(amagats)	0.070±1.7%	0.069±1.8%	0.082±1.8%
^{3}He Density (cm^{-3})	2.32×10^{20}±2.5%	2.39×10^{20}±2.0%	2.35×10^{20}±2.0%
N_2 Density (cm^{-3})	1.88×10^{18}±1.7%	1.85×10^{18}±1.8%	2.20×10^{18}±1.8%

Table 3.5: Polarized target parameters used in calculating the dilution factor. (An amagat is the density of 1 mole of gas at 0°C and 1 atmosphere pressure.)

Dilution Factor Experimental Results

A nice feature of the experiment was the ability to determine the dilution factor experimentally. Empty glass reference cells of similar length, L, and thickness to the target cells were moved into the beam, and known densities of ^{3}He were introduced. By measuring the event rate versus ^{3}He pressure, P, we could extract the dilution factor. At zero pressure the events are due solely to the glass endcaps, and the additional events resulting when the cell was filled were due to ^{3}He :

$$\frac{\text{Event Rate}(x,Q^2)}{\text{Incident Charge}} = N\left[n_g\sigma_g(x,Q^2) + \frac{3N_{AV}LP}{RT}\sigma_H(x,Q^2)\right] \qquad (3.18)$$

where N is a proportionality constant, and R is the gas constant. When we set $P = P_{\text{Target Cell}}$ then $3N_{AV}LP/RT = n_H$ as in (3.15). If we plot event rate for events falling into a selected x bin versus reference cell pressure, as in Figure 3.28, then we observe a straight line. The slope, a, can be interpreted as $Nn_H\sigma_H(x,Q^2)/P_{\text{Target Cell}}$, and intercept, b, as $Nn_g\sigma_g(x,Q^2)$. Then we extract :

$$F_{^3\text{He}}(x,Q^2) = \frac{aP_{\text{TargetCell}}}{(aP_{\text{Target Cell}} + b)}. \qquad (3.19)$$

In practice the result had to be scaled to take into account the fact that the reference cell windows were thicker than the target cells, and that N_2 was absent from the

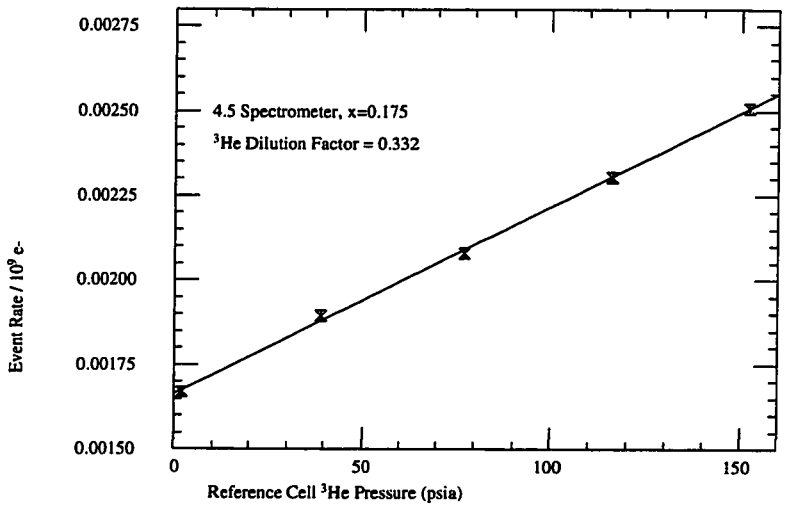

Figure 3.28: This data comes from a sequence of reference cell runs. The dependence of event rate on pressure is used to extract the dilution factor.

reference cells. The main experimental difficulty of the technique was to properly account for the rate dependence efficiencies of our event selection, knowledge of which is important for the asymmetry analysis.

Final Dilution Factor Results

In Figure 3.29 we show the results of a theoretical calculation of the dilution factor of one of the reference cells with the experimental observations. The two approaches yield similar answers for the dilution factor, which differed at most by 7%. The 9% uncertainty in the theoretical dilution factor of the reference cells is larger than that for the real target cells because the density of gas in the reference cells was not known with the same precision. Given the good agreement between the measurement and the theory for the reference cells, we use the theoretical calculation from (3.17) to determine the ^{3}He dilution factor for the target cells, and quote an uncertainty of 8%. A plot of the dilution factor for one of the target cells used in the asymmetry analysis is shown in Figure 3.30.

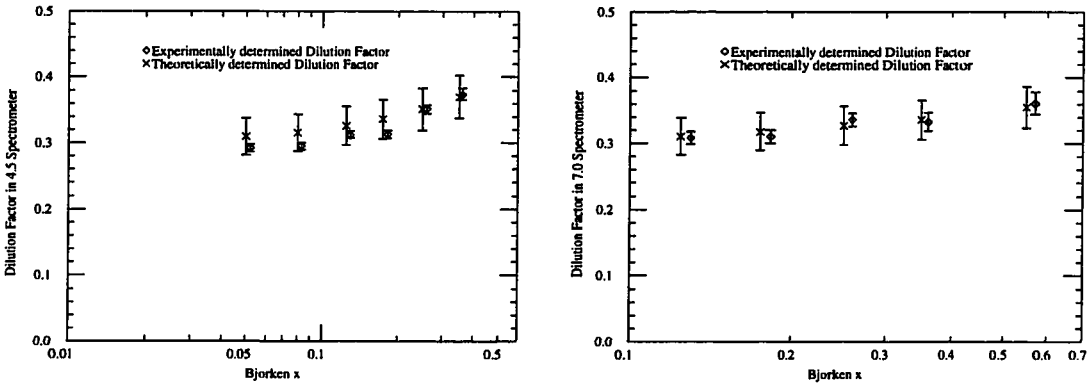

Figure 3.29: The theoretical and experimental results of the dilution factor of a reference cell are shown, using a ^{3}He pressure of 147 psia. The maximum difference between the two results is 7%.

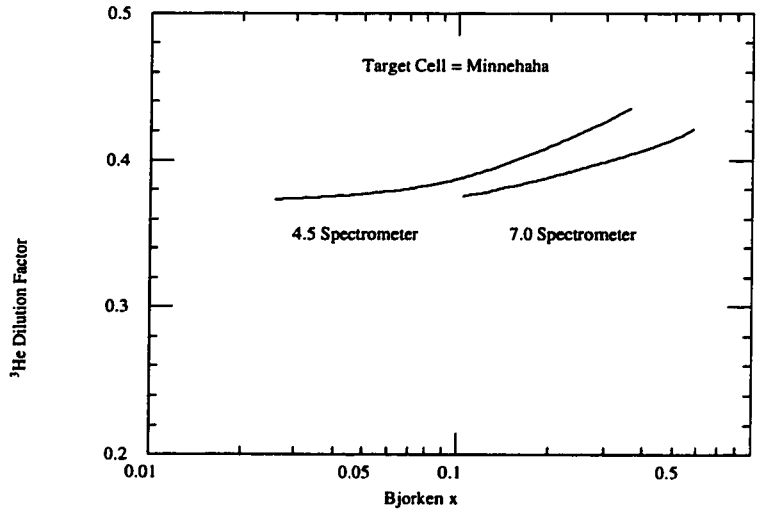

Figure 3.30: This plot shows the results of a theoretical calculation of the dilution factor. These results are used in the asymmetry analysis, with an estimated uncertainty of 8%.

3.6.7 $F_2(x, Q^2)$ and $R(x, Q^2)$

Calculating the dilution factor and extracting A_1^n and g_1^n requires knowledge of the unpolarized structure functions F_2^n, $F_2^{^3He}$, as well as the ratio of longitudinal to transverse virtual photon cross sections, $R^p(x, Q^2) = \sigma_L^p(x, Q^2)/\sigma_T^p(x, Q^2)$ and $R^n = \sigma_L^n/\sigma_T^n$. The New Muon Collaboration, amongst others, found that experimentally R^p and R^D are the same [105], so we will not distinguish between R^p and R^n. The central values and errors on $R(x, Q^2)$ in the analysis are taken from Whitlow's fit [106].

Since there are no free neutron targets, F_2^n is derived from DIS cross section data on proton and deuterium targets [107, 108, 109, 110, 111]. The measured F_2^p is smeared using a model of the deuteron wavefunction and subtracted from the measured F_2^D. The smeared F_2^n resulting is then input into the deuteron model and iterated until a stable, unsmeared F_2^n can be extracted. In the region $x \leq 0.45$ of this experiment, the ratio of Fermi smeared to unsmeared structure functions for both the proton and neutron deviate from 1 by less than 0.5% [112, 110]. Then for our purposes it will be sufficient to take $F_2^n = 2 \times F_2^D - F_2^p$ where the proton and deuteron structure functions, per nucleon, are taken from the NMC fits [111] to the SLAC [109], BCDMS [107] and NMC data. Since no errors are included in the NMC fit, we will use the errors from Whitlow's fit [110] to the SLAC data since these dominate our region of interest in the NMC fit. We include a normalization uncertainty from the SLAC data of 2.1% for F_2^p and 1.7% for F_2^D. Further, we include a 2% uncertainty for the proton and 0.6% on the deuteron arising from the maximum deviation of the SLAC and NMC fits in the range $0.08 < x < 0.6$. For $x < 0.08$ there is very little data from SLAC, so a 4.5% error is placed on the NMC structure functions in this range, coming from the maximum deviation of the NMC data from the NMC fit.

The systematic errors returned by Whitlow's fit, as well as the normalization uncertainties are assumed to be completely correlated between the proton and deuteron, reflecting the manner in which the structure functions were measured. For $x < 0.08$, 50% of the error is assumed to be correlated.

The ^{3}He structure function is then calculated as :

$$F_2^{^3He}(x, Q^2) = \mathrm{EMC}(x)[2 \times F_2^D(x, Q^2) + F_2^p(x, Q^2)]/3 \qquad (3.20)$$

where EMC(x) is an estimate of the EMC effect in ^{3}He from [104], and differs from

unity by less than 2% in our kinematic range. The nuclear effects are expected to be small because of the small nuclear removal energy in ^{3}He [113]. We will assign an additional 1% uncertainty on $F_2^{^3He}$ apart from that coming from F_2^p and F_2^D due to the EMC effect.

3.6.8 Radiative Corrections

Another correction that must be made to the measured asymmetry in equation (3.4) comes from radiative effects. These are traditionally divided into two categories, 'internal' and 'external'. The internal effects are those occurring at the nucleus where the inelastic scattering occurs. The external effects are those which modify the energy of the electron by bremsstrahlung and ionization losses from interactions with other atoms before or after the DIS event.

Internal Radiative Corrections

The structure function $g_1^n(x)$ and asymmetry $A_1^n(x)$ are defined in the limiting case of a single virtual photon exchange. However, experimentally observed lepton-nucleon scattering includes contributions from virtual processes, elastic, quasielastic and inelastic tails, in addition to the Born level process in which we are interested. Since the contributions from these tails are not identical for the two orientations of lepton-nucleon spin, the measured asymmetry is different from the Born asymmetry and must be corrected. The formalism for calculating the radiative corrections (RC) to spin dependent deep inelastic scattering (DIS) has been well developed by Kukhto, Shumeiko and Akushevich [114, 115] and implemented in their Fortran code POLRAD 1.4 [115].

The measured DIS cross section can be decomposed into components (with spin indices suppressed) :

$$\sigma_m(x,y) = \sigma_0(x,y)\frac{\alpha}{\pi}(\delta_R^{IR} + \delta_{vert} + \delta_{vac}^l + \delta_{vac}^h) + \sigma_{in}^F(x,y) + \sigma_{qel}(x,y) + \sigma_{el}(x,y) \quad (3.21)$$

where σ_m is the measured differential cross section $d^2\sigma/dxdy$, σ_0 is the Born level cross section of interest, δ_R^{IR} is the correction due to soft photon emission, δ_{vert} is the lepton vertex correction, δ_{vac}^l is the lepton vacuum polarization, δ_{vac}^h is the hadronic

vacuum polarization, σ_{in}^{F} is the infrared divergence-free part of the inelastic radiative tail, and σ_{qel} and σ_{el} are the quasielastic and elastic tail contributions respectively. Since the soft photon and virtual corrections to the cross section are insensitive to the spin of the interaction, these contributions factorize and the RC to the measured asymmetry come from the elastic, quasielastic and inelastic tails. In the case of E142, the latter two dominate as we now discuss.

With the emission of a hard photon by the incident electron before scattering, the E and Q^2 of the event are lowered. Since the electric and magnetic form factors of the constituent protons and neutron in ^{3}He (loosely speaking) rise as $\sim 1/Q^4$, the probability of scattering quasielastically is enhanced. Again speaking loosely, since the nucleons are polarized within polarized ^{3}He, there will be a spin dependent asymmetry in this scattering, expressible in term proportional to $G_E G_M$ and G_M^2 [116, 117, 118]. Radiative effects thus mix in this asymmetry with the DIS asymmetry in which we are interested. The magnitude of this contribution increases as we move to lower x and Q^2. Nuclear structure details of ^{3}He are important here for predicting the polarizations of the nucleons, and the modification of the electric and magnetic form factors of the constituent nucleons in the nuclear environment. Predictions for the D and S' percentages of the ^{3}He wavefunction are used to determine the small quasielastic asymmetry contribution from the protons in ^{3}He, which is otherwise due solely to the neutron. The quasielastically scattered electrons constitute as much as 8% of the events measured in the $x = 0.035$ bin of the 4.5° spectrometer, and less in all other bins. Electrons which have scattered elastically from ^{3}He are less likely, and compose fewer than 1% of the events we detect.

The inelastic tail contribution arises in a similar manner. Electrons entering our spectrometers having undergone hard photon emission before (after) scattering will have their E (E') over(under)estimated, and in both cases will be assigned a lower value of Bjorken x than the true x of the event. In this way, DIS asymmetries from higher x are mixed into the asymmetry measured at lower x.

For E142, the internal radiative corrections were determined using the POLRAD code. Specifically, a smooth fit to $A_1^{^3\mathrm{He}}(x)$ was made from the data, from which a model for $g_1^{^3\mathrm{He}}(x)$ was constructed. Radiative corrections were calculated to $A_1^{^3\mathrm{He}}$

using POLRAD :

$$A_1^{\text{Born}}(x) = A_1^{\text{measured}}(x) - \Delta A_1(x) \tag{3.22}$$

where $\Delta A_1(x)$ is the radiative correction to the asymmetry [115]. From this, a new model of $g_1^{^3\text{He}}$ was constructed

$$g_1^{(n)} = \frac{F_2(x,Q^2)}{2x\,(1+R(x,Q^2))}(A_1^{\text{measured}} - \Delta A_1(g_1^{(n-1)})) \tag{3.23}$$

where the index, n, reflects the number of iterations performed. Convergence occurs after about three iterations.

While there are theoretical and experimental uncertainties in the models used to calculate the elastic and inelastic tails, these contributions are independent of the shape of the input continuuum spectrum, which is determined by F_2, R, and $A_1^{^3\text{He}}$. However, a further model dependency arises from the comparatively low beam energy available to E142. At high x, with the emission of a hard photon before scattering, the small Q^2 of the event entails that the missing mass squared, $W^2 = M^2+Q^2(1/x-1)$, is low and the resonance structure of the nucleon is being probed. The spin dependence of the structure functions in the resonance region have not yet been measured, so a theoretical model of Lu and Burkert (unpublished) was inserted into POLRAD.

The final results are presented after a discussion of the external radiative corrections.

External Radiative Corrections

In addition to the 'internal' radiative effects occurring during DIS, the electrons will lose a small amount of energy by ionization, and potentially a much larger amount by bremsstrahlung interactions with other target nucleii before and after the DIS event. Like the 'internal' effects, these 'external' effects make the uncorrected measured asymmetry a convolution of asymmetries from a large kinematic space, and are an important consideration in electron scattering since the bremsstrahlung cross section is so large. To unravel the effects of finite target thickness on the measured asymmetry we use the procedures outlined by Mo and Tsai [119, 120].

Electrons entering the target first pass through the front glass endcap, which is only 0.001 radiation lengths long and has a small effect on the final cross section.

Spectrometer	Fraction of Events	Radiation Lengths (t_{out})
4.5°	36.50%	0.001
	54.55%	0.085
	6.85%	0.169
	2.10%	0.291
7.0°	23.39%	0.001
	48.36%	0.055
	18.75%	0.269
	9.50%	0.399

Table 3.6: Radiation lengths, t_{out}, seen by electrons exiting the target.

Radiative losses in the 0.0005 radiation length ^{3}He gas part of the target are even more negligible. The main effect occurs as the DIS electrons exit the target and pass at shallow angles through various thicknesses of glass, and sometimes parts of the target's NMR pickup coils (composed of teflon and copper). Table 3.6 shows the the radiation lengths seen in exiting the target by electrons scattered at different points within the target. We will neglect ionization losses. The measured polarized cross sections, $\sigma^m_{\rm pol\pm}$ can be expressed in terms of the internally radiated polarized cross sections (uncorrected cross sections measured if the target had no thickness, calculated by POLRAD), $\sigma^{IR}_{\rm pol\pm}$ as :

$$\sigma^m_{\rm pol\pm}(E_s,E_p) = \int_{E_s^{\rm min}(E_p)}^{E_s} dE'_s \int_{E_p}^{E_p^{\rm max}(E'_s)} dE'_p I(E_s,E'_s,t_{in})\sigma^{IR}_{\rm pol\pm}(E'_s,E'_p)I(E'_p,E_p,t_{out}) \tag{3.24}$$

where E_s, E_p are the assumed initial and final electron energies, and $I(E_{in},E_{out},t)$ is the probability that an electron of energy E_{in} will have an energy E_{out} after having passed through t radiation lengths of material. The function I is a solution of the diffusion equation for electron energy straggling. The limits of integration are determined from elastic scattering conditions, so that $E_s^{\rm min}(E_p) = E_p/(1-E_p(1-\cos\theta)/M)$ is the minimum incident energy required to produce a scattered electron with E_p. $E_p^{\rm max}(E'_s)$ is the maximum scattered energy if the incident energy is E'_s. The parameter t_{in} is the thickness in radiation lengths traversed by an average electron before scattering. For our target t_{in} is 0.00125, which is the thickness of the target entrance

window plus half of the ^{3}He radiation length. The electrons exit the target through four discrete sections, so that (3.24) is actually the sum over the four values of $t_{\rm out}$ in Table 3.6. The function $I(E_{in}, E_{out}, t)$ is sharply peaked when $E_{in} \approx E_{out}$, and singular for $E_{in} = E_{out}$:

$$\begin{aligned} I(E_{in}, E_{out}, t) &= I(E_{in}, E_{in} - \omega, t) \\ &= \frac{1}{\Gamma(1+bt)}\Big(\frac{\omega}{E_{in}}\Big)^{bt}\frac{bt}{\omega}\phi\Big(\frac{\omega}{E_{in}}\Big), \end{aligned} \tag{3.25}$$

where the bremsstrahlung spectrum is given by

$$\frac{1}{\omega}\phi\Big(\frac{\omega}{E_{in}}\Big) \approx \frac{1}{\omega}\Big[1 - \Big(\frac{\omega}{E_{in}}\Big) + \frac{3}{4}\Big(\frac{\omega}{E_{in}}\Big)^2\Big],$$

and

$$b = \frac{4}{3}\Big[1 + \frac{1}{12}\Big[\frac{Z+1}{Z+\eta}\Big]\Big(\log 184.15Z^{-1/3}\Big)^{-1}\Big], \quad \eta = \log 1194Z^{-2/3}/\log 184.15Z^{-1/3}.$$

Here Z is the average Z of the target material. The peaked behavior of I allows us to separate the double integral (3.24) into parts (introducing a few percent error). To handle the singularity of the integrand we will introduce a cutoff at $\Delta = 15$ MeV, and then integrate analytically, using the reasonable assumption that the cross section is constant over the cutoff range :

$$\begin{aligned} \int_{E_s^{\min}(E_p)}^{E_s} I(E_s, E_s', t_{in})\sigma^{IR}_{\rm pol\pm}(E_s', E_p)dE_s' \approx \Big(\frac{\Delta}{E_s}\Big)^{bt_{in}}\sigma^{IR}_{\rm pol\pm}(E_s, E_p) + \\ \int_{E_s^{\min}(E_p)}^{E_s-\Delta} I(E_s, E_s', t_{in})\sigma^{IR}_{\rm pol\pm}(E_s', E_p)dE_s' \end{aligned} \tag{3.26}$$

With these approximations, the expression for calculating the effects of external bremsstrahlung in the target becomes :

$$\begin{aligned} \sigma^{m}_{\rm pol\pm}(E_s, E_p) &= \Big(\frac{\Delta}{E_s}\Big)^{bt_{in}}\Big(\frac{\Delta}{E_p}\Big)^{bt_{out}}\sigma^{IR}_{\rm pol\pm}(E_s, E_p) + \\ &\Big(\frac{\Delta}{E_s}\Big)^{bt_{in}}\int_{E_p+\Delta}^{E_p^{\max}(E_s')}\sigma^{IR}_{\rm pol\pm}(E_s, E_p')I(E_p', E_p, t_{out})dE_p' + \\ &\Big(\frac{\Delta}{E_p}\Big)^{bt_{out}}\int_{E_s^{\min}(E_p)}^{E_s-\Delta} I(E_s, E_s', t_{in})\sigma^{IR}_{\rm pol\pm}(E_s', E_p)dE_s'. \end{aligned} \tag{3.27}$$

By solving this equation for each polarization we can form an asymmetry from the measured polarized cross sections, $\sigma^m_{\rm pol\pm}$, which we compare with the asymmetry formed from the internally radiated, zero target length polarized cross sections $\sigma^{IR}_{\rm pol\pm}$. The difference is then the additive correction we make to $A_1^{^3\rm He}$, denoted $\Delta^{\rm ext}_{RC}$:

$$\begin{aligned} A_1^{^3\rm He} &= \frac{1}{D(1+\eta\zeta)}\left[\frac{\sigma^{IR}_{\rm pol+}-\sigma^{IR}_{\rm pol-}}{\sigma^{IR}_{\rm pol+}+\sigma^{IR}_{\rm pol-}}\right] \\ &\equiv \frac{1}{D(1+\eta\zeta)}\left[\frac{\sigma^{m}_{\rm pol+}-\sigma^{m}_{\rm pol-}}{\sigma^{m}_{\rm pol+}+\sigma^{m}_{\rm pol-}}\right] + \Delta^{\rm ext}_{RC}. \end{aligned} \tag{3.28}$$

Statistical Errors and Radiative Corrections

Radiative corrections complicate our calculation of the statistical uncertainty of our measurement. To see this, first consider the problem of the internal radiative corrections to a zero radiation length target in the peaking approximation [119]. Then we can relate the measured cross section $\sigma^m = d^2\sigma^m/d\Omega dE_p$ to the Born cross section with virtual corrections, σ^{BV} by :

$$\begin{aligned} \sigma^{BV}(E_s,E_p) &= \sigma^m(E_s,E_p) \\ &\quad - \int_{E_s^{\rm min}(E_p)}^{E_s-\Delta} dE'_s \psi_{\rm in}(E_p,E'_s/E_s)\sigma^{BV}(E'_s,E_p) \\ &\quad - \int_{E_p+\Delta}^{E_p^{\rm max}(E_s)} dE'_p \psi_{\rm out}(E_s,E_p/E'_p)\sigma^{BV}(E_s,E'_p) \end{aligned} \tag{3.29}$$

(Paraphrasing Tsai's equation (IV.2) [119]) where E_s, E_p are the assumed initial and final electron energies, and Δ is a small energy cutoff. The functions ψ, which are positive, parameterize the probability of internal bremsstrahlung before and after the scattering event, mixing the cross sections $\sigma(E_s,E'_p)$ and $\sigma(E'_s,E_p)$ with the measured cross section $\sigma^m(E_s,E_p)$. It is this mixing which we wish to undo. To 0th order we can solve (3.29) by replacing $\sigma^{BV}(E_i,E_j)$ by $\sigma^m(E_i,E_j)$:

$$\begin{aligned} \sigma^{BV}(E_s,E_p) &\approx \sigma^m(E_s,E_p) \\ &\quad - \int_{E_s^{\rm min}(E_p)}^{E_s-\Delta} dE'_s \psi_{\rm in}(E_p,E'_s/E_s)\sigma^{m}(E'_s,E_p) \\ &\quad - \int_{E_p+\Delta}^{E_p^{\rm max}(E_s)} dE'_p \psi_{\rm out}(E_s,E_p/E'_p)\sigma^{m}(E_s,E'_p). \end{aligned} \tag{3.30}$$

In this form we see explicitly that σ^{BV} depends on knowledge of the cross section in a large region of (E'_s, E'_p) space. In addition, we see that the proper calculation of the statistical uncertainty of the Born cross section depends on the uncertainty of the measured cross section over the same (E'_s, E'_p) space, introducing complicated correlations.

Fortunately, for our asymmetry measurement the situation is less complicated because the unpolarized cross sections are considered to be known. If we write the spin dependent DIS electron cross sections in terms of the unpolarized cross section and the ^{3}He asymmetry, $\sigma^{BV}_{\rm pol\pm} = \sigma^{BV}_{\rm unpol}(1 \pm DA_1^{^3{\rm He}})$, then we can rewrite (3.29) as :

$$\begin{aligned}
\sigma^{BV}_{\rm pol\pm}(E_s, E_p) &= \sigma^{m}_{\rm pol\pm}(E_s, E_p) \\
&\quad - \int_{E_s^{\rm min}(E_p)}^{E_s-\Delta} dE'_s \psi_{\rm in}(E_p, E'_s/E_s)\sigma^{BV}_{\rm unpol}(1 \pm DA_1^{^3{\rm He}})(E'_s, E_p) \\
&\quad - \int_{E_p+\Delta}^{E_p^{\rm max}(E_s)} dE'_p \psi_{\rm out}(E_s, E_p/E'_p)\sigma^{BV}_{\rm unpol}(1 \pm DA_1^{^3{\rm He}})(E_s, E'_p) \\
&\equiv \sigma^{m}_{\rm pol\pm}(E_s, E_p) - \sigma^{\rm tail}_{\rm unpol}(E_s, E_p) - \sigma^{\rm tail}_{\rm pol\pm}(E_s, E_p) \qquad (3.31)
\end{aligned}$$

where $\sigma^{\rm tail}_{\rm unpol}$ comes from the first part of each integral, and $\sigma^{\rm tail}_{\rm pol\pm}$ from the second. Since $\sigma^{\rm tail}_{\rm unpol}$ comes entirely from known unpolarized data, it is completely uncorrelated with the measured cross section, and can be treated as a pure background subtraction in (3.31). However, the polarized tail component will introduce correlations between $\sigma^{m}_{\rm pol\pm}$ and the asymmetry from other kinematic regions when extracting $\sigma^{BV}_{\rm pol\pm}$ in (3.31). The statistical error will then be expressed as :

$$\left(\delta\sigma^{BV}_{\rm pol\pm}\right)^2 = \left(\delta\sigma^{m}_{\rm pol\pm}\right)^2 + \left(\delta\sigma^{\rm tail}_{\rm unpol}\right)^2 + \left(\delta\sigma^{\rm tail}_{\rm pol\pm}\right)^2 - 2{\rm covar}\langle\delta\sigma^{m}_{\rm pol\pm}, \delta\sigma^{\rm tail}_{\rm pol\pm}\rangle. \qquad (3.32)$$

Two observations are necessary to proceed, first since $A_1(E'_s, E'_p)$ is predominantly of one sign for the regions of integration, then $\delta\sigma^{\rm tail}_{\rm pol\pm} \approx \sqrt{|\sigma^{\rm tail}_{\rm pol\pm}|}$. Second, the data and models indicate roughly that $\sigma^{\rm tail}_{\rm pol\pm} < 0.2 \times \sigma^{\rm tail}_{\rm unpol}$, and $\sigma^{\rm tail}_{\rm unpol} < 0.25 \times \sigma^{m}_{\rm pol\pm}$, so that the covariance term in the statistical error is less than 5% of the total error and can reasonably be ignored. The same argument applies to the external radiative corrections so we can express the total effect of radiative corrections on the statistical error by :

$$\delta\sigma^{BV}(E_s, E_p) = \delta\sigma^{m}(E_s, E_p)\sqrt{1 + f_{\rm el} + f_{\rm quel} + f_{\rm inel} + f_{\rm ext}} \qquad (3.33)$$

where the fs are the absolute values of the fractions of the total measured cross section coming from elastic, quasielastic and inelastic tails, and the background fraction leaking in due to external radiative corrections (polarization indices have been suppressed). The more detailed radiative correction procedure actually employed will not disturb our conclusion that we can treat the radiative tails as a background subtraction for the purposes of calculating statistical errors.

Radiative Corrections Systematic Errors

The radiative corrections are sensitive to the cross section shapes. As an estimate of the sensitivity, we input a flat asymmetry into POLRAD as a model for $A_1^{^3He}$, and then a quadratic fit to the data with weak constraints at low and high x. From the variation of the results, we estimate a 25% uncertainty in the internal and external radiative corrections to the 7.0° spectrometer data, and 25% uncertainty in the internal correction of the 4.5°. This also reflects uncertainties arising from the cross section models used within POLRAD, and in particular our uncertainty in the resonance region. The external corrections to the 4.5° were particularly sensitive to the cross section shape at high x, which decreases very rapidly. This correction is assigned a 35% uncertainty.

Radiative Corrections Final Results

In Table 3.7 and Figure 3.34 we present the additive internal radiative corrections, Δ_{RC}^{int}, and the external corrections, Δ_{RC}^{ext}, to be made to the asymmetry, $A_1^{^3He}$. The fs in the table are the fractions of events coming from elastic, quasielastic, and inelastic tails, as well as the fraction of events leaking in due to external radiative effects.

3.6.9 $A_2^{^3He}(x, Q^2)$

At this point the last remaining correction to $A_1^{^3He}(x, Q^2)$ in equation (3.4) is that coming from the transverse asymmetry, $A_\perp$. Having only limited beam time, a high statistics measurement of $A_\perp$ could not be performed. Instead the intent of the 9 transverse asymmetry runs taken was to place a better bound on A_2^n than $\sqrt{R}$ (see

x	Δ_{RC}^{int}	Δ_{RC}^{ext}	f_{elas}	f_{quel}	f_{inel}	f_{ext}
0.035	-0.0025	-0.0002	0.003	0.079	0.148	0.100
0.050	-0.0031	-0.0007	0.001	0.042	0.128	0.082
0.080	-0.0035	-0.0017	0.000	0.017	0.099	0.077
0.125	-0.0038	-0.0026	0.000	0.007	0.067	0.077
0.175	-0.0040	-0.0030	0.000	0.004	0.040	0.050
0.250	-0.0039	-0.0033	0.000	0.003	0.008	0.038
0.350	-0.0032	-0.0024	0.000	0.002	-0.019	0.017
0.080	-0.0042	-0.0012	0.001	0.038	0.112	0.089
0.125	-0.0039	-0.0024	0.000	0.013	0.069	0.094
0.175	-0.0040	-0.0032	0.000	0.006	0.036	0.061
0.250	-0.0039	-0.0030	0.000	0.002	0.003	0.045
0.350	-0.0032	-0.0020	0.000	0.001	-0.033	0.016
0.466	-0.0015	-0.0001	0.000	0.000	-0.063	0.005

Table 3.7: The radiative corrections to $A_1^{^3\text{He}}(x)$ are tabulated here, with the corrections to the 4.5° spectrometer given first, then those of the 7.0°. The Δs are the additive corrections to be made to the asymmetry, and the fs are the fractions of events in a particular bin coming from elastic, quasielastic, and inelastic tails, as well as from external radiative effects.

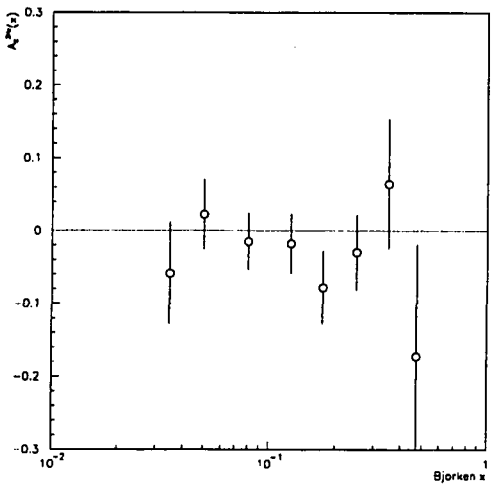

Figure 3.31: The asymmetry $A_2^{^3\mathrm{He}}$ is plotted. The results are consistent with zero ($\chi^2/df = 0.6$).

Chapter 1). As a first step, we examine the asymmetry $A_2^{^3\mathrm{He}}$:

$$A_2^{^3\mathrm{He}} = \frac{1}{(1+\eta\zeta)}\left[\frac{A_\perp^{\mathrm{rawe}^-}}{dP_bP_tf} + \frac{\zeta}{D}\frac{A_\parallel^{\mathrm{rawe}^-}}{P_bP_tf}\right] \tag{3.34}$$

where we have omitted deadtime and radiative corrections since they were not calculated. The experimental results on this asymmetry are shown in Figure 3.31. The results are consistent with zero ($\chi^2/df = 0.6$) so in the rest of the analysis we will set $A_2^{^3\mathrm{He}} = 0$. Note that from equation (3.34) this determines $A_\perp$ in terms of $A_\parallel$. The uncertainty on $A_\perp$, which enters into our determination of $A_1^{^3\mathrm{He}}$, will be taken as either the statistical uncertainty on $A_\perp$ coming from the nine transverse runs, or from the bound $A_2^n < \sqrt{R}$, whichever is smaller. No algorithms for extracting A_2^n from $A_2^{^3\mathrm{He}}$ have been published, so we will use the simple ansatz that $A_2^{^3\mathrm{He}} = F_2^n A_2^n / F_2^{^3\mathrm{He}} p_n$ where p_n is the polarization of the neutron within ^{3}He. The result of these considerations is that the uncertainty on our measurement of $A_\perp$ is a better bound than $\sqrt{R}$ except for in the last two x bins, x=0.35 and x=0.47.

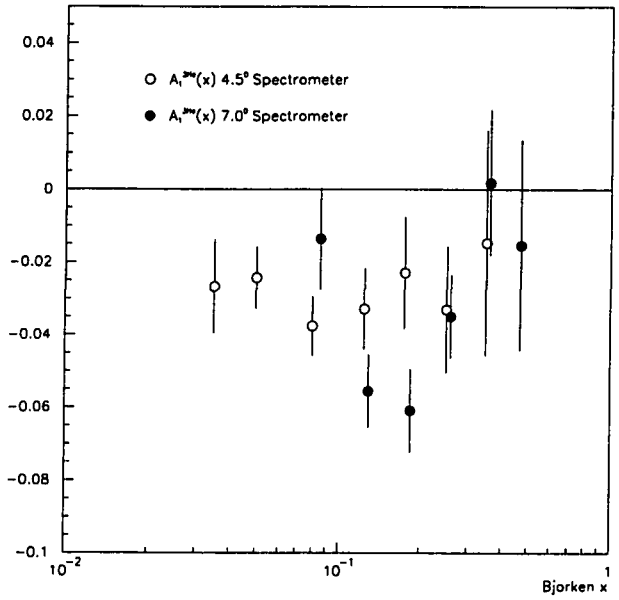

Figure 3.32: The results for $A_1^{^3He}(x)$ from both spectrometers are plotted. In the five x bins that they overlap the results are reasonably consistent. The errors shown are statistical.

3.6.10 Final Results

Results on $A_1^{^3He}$

The values for $A_1^{^3He}$ of both spectrometers from the $\sim$ 270 parallel asymmetry runs were averaged together, assuming that $A_1^{^3He}$ is independent of Q^2, and having determined $A_\perp$ under the assumption that $A_2^{^3He} = 0$. The results from the two spectrometers individually are seen in Figure 3.32. In order to compare the spectrometers we define the difference

$$\Delta(x) = \frac{A_1^7(x) - A_1^{4.5}(x)}{\sqrt{\delta^2 A_1^7(x) + \delta^2 A_1^{4.5}(x)}} \tag{3.35}$$

where A_1^i is the asymmetry in spectrometer i and δA_1^i is the statistical error. Making the assumption that the spectrometers should agree with each other, we would expect

that in the region where the spectrometers overlap the differences observed should be normally distributed in a Gaussian with a mean of 0 and width of 1. With this hypothesis, the probability of observing by chance the mean difference seen in Figure 3.32 is a little more than 50%. Testing the hypothesis that the width of the distribution of differences is 1, we find that the probability of observing our results by chance is 13%. This may be considered as a lower bound on the level of agreement because some of the systematic errors in each spectrometer, such as the deadtime correction, are calculated separately and probably should be added in quadrature before comparing the spectrometers. It appears on these grounds that we can consider the 4.5° and 7.0° spectrometers to be reasonably consistent with each other. Averaging the two spectrometers together we have the final result for $A_1^{^3\mathrm{He}}(x)$ in Figure 3.33. The asymmetry is seen to be small and negative.

Results on A_1^n

To extract A_1^n from $A_1^{^3\mathrm{He}}$ we use the expression :

$$A_1^{^3\mathrm{He}} = A_1^n \frac{F_2^n p_n}{F_2^{^3\mathrm{He}}} + A_1^p \frac{2F_2^p p_p}{F_2^{^3\mathrm{He}}} \tag{3.36}$$

where $p_p = -0.027 \pm 0.004$ is the polarization of the protons in ^{3}He, and the asymmetry A_1^p is taken from the recent measurement of E143 [128]. The results for A_1^n are shown in Figure 3.35.

False Asymmetry

One of the strengths of this experiment was that the frequent beam and target spin flips enabled us to average over false asymmetries. If the properties of the beam were slightly different for the two helicities, or if there were slow changes in the spectrometer acceptance, the effects should average out over the entire data set. As a test of the magnitude of possible false asymmetries we can subtract the asymmetry determined from data taken with the target spin pointed one direction from the asymmetry measured when the target was pointed in the opposite direction. Ideally, the result will be consistent with zero. In Figure 3.36 we plot the false asymmetry, and find an average value of 0.019 ± 0.027. The probability of observing this distribution

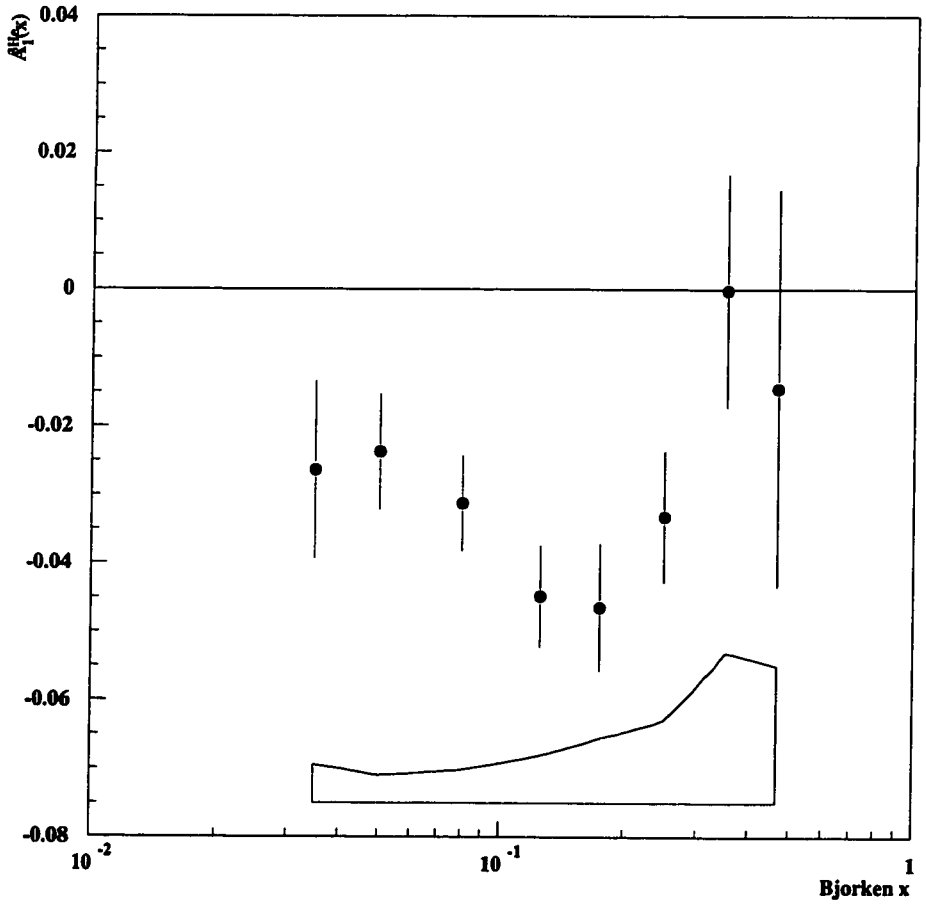

Figure 3.33: The asymmetry $A_1^{^3He}(x)$ averaged over both spectrometers is plotted. The error bars are statistical, with the enclosed region at the bottom indicating the systematic errors.

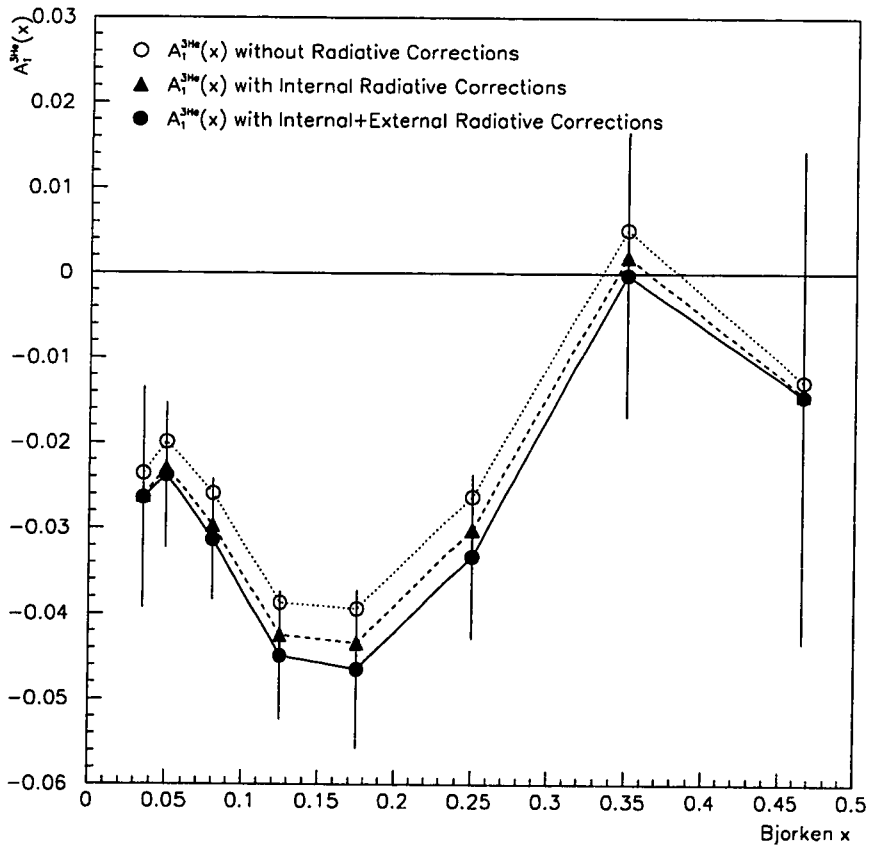

Figure 3.34: Here we show the evolution of the asymmetry A_1^{He} as the internal and then internal+external radiative corrections are added. The statistical error is shown for comparison.

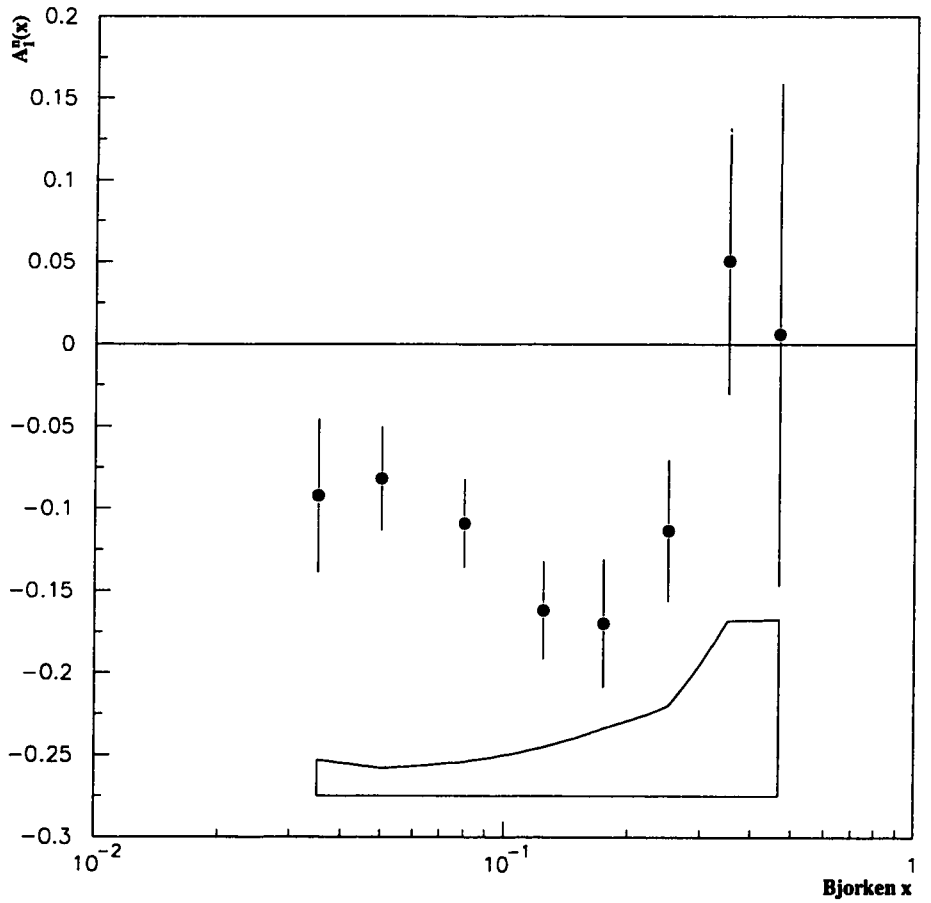

Figure 3.35: The asymmetry A_1^n is seen to be small and negative. The error bars are statistical, with the systematic errors indicated by the enclosed region at the bottom of the plot.

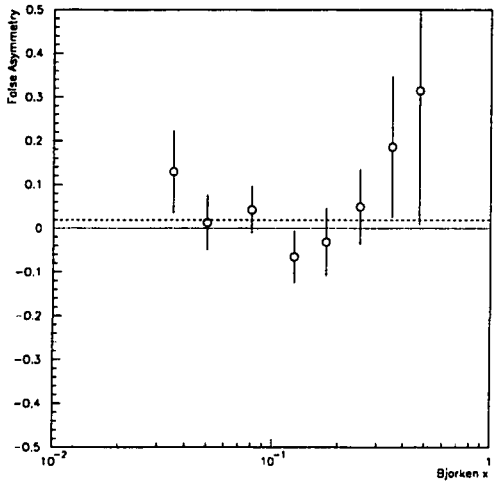

Figure 3.36: The asymmetry determined with the target pointed in one direction is subtracted from the asymmetry found when the target spin is in the opposite direction. The difference is consistent with zero.

assuming that there are no false asymmetries, is 20%. This may be taken to mean that there were no large false asymmetries.

Results on A_1^n versus Q^2

If we extract A_1^n separately from the two spectrometers and three beam energies used by E142, we obtain A_1^n at six different values of Q^2. Over this modest range of Q^2 and within the statistical errors, we find that A_1^n is consistent with being independent of Q^2, as seen in Figure 3.37.

Results on $g_1^{^3He}$ and g_1^n

We can extract $g_1^{^3He}$ from $A_1^{^3He}$ by :

$$g_1^{^3He}(x,Q_0^2) = \frac{F_2^{^3He}(x,Q_0^2)}{2x\,[1+R(x,Q_0^2)]}\left[A_1^{^3He}(x,Q_{exp}^2) + \frac{\sqrt{Q_0^2}}{\nu}A_2^{^3He}(x,Q_{exp}^2)\right] \qquad (3.37)$$

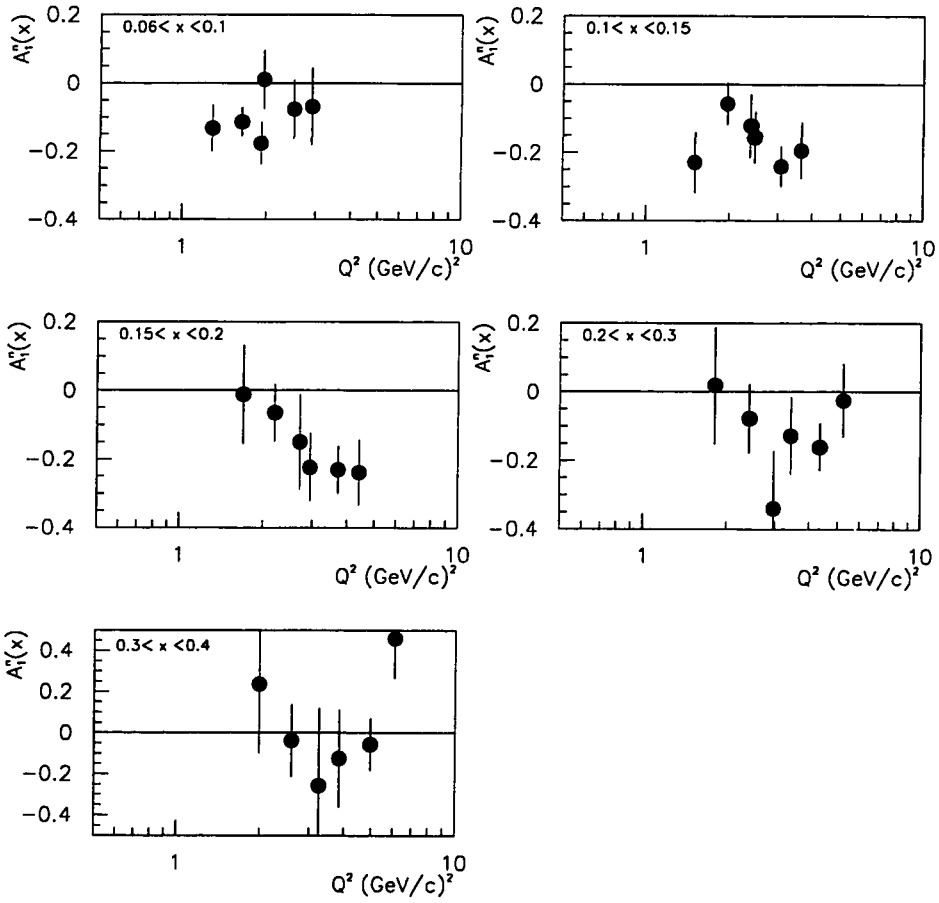

Figure 3.37: The asymmetry A_1^n for five values of Bjorken x is plotted versus Q^2. The results are consistent with A_1^n being independent of Q^2.

where Q^2_{exp} is the Q^2 at which the data point was taken. We will use $A_2 = 0$, and evaluate F_2 and R at the average Q^2 of E142, $Q^2_0 \equiv \langle Q^2 \rangle = 2$ (GeV/c)^2. The result is shown in Figure 3.38. Finally, we can extract g_1^n using :

$$g_1^n(x, Q_0^2) = \frac{1}{p_n}\left[g_1^{^3\mathrm{He}}(x, Q_0^2) - 2p_p g_1^p(x, Q_0^2)\right] \tag{3.38}$$

where p_p is the proton polarization in ^{3}He, and g_1^p is taken from the measurement of E143 [128]. The result is calculated at a fixed $Q^2 = 2$ (GeV/c)^2 and plotted in Figure 3.39. Table of the results are given below.

3.6.11 Systematic Errors

The systematic uncertainties affecting the primary quantities, A_1^n and g_1^n extracted from this experiment have been discussed in the previous sections. For convenience we will summarize the results in Table 3.8.

The resulting uncertainties on our measurement of A_1^n coming from each of the systematic errors listed above, are shown in Table 3.9. The systematic errors on g_1^n are given in Table 3.10.

The final results for $A_1^{^3\mathrm{He}}(x)$ and $g_1^{^3\mathrm{He}}(x, Q^2)$ evaluated at $Q^2 = 2$ (GeV/c) are given in Table 3.11. Also shown are the range of each x bin and the average x and Q^2 of the data within the bin. The results for $A_1^n(x)$ and $g_1^n(x, Q^2)$ evaluated at $Q^2 = 2$ (GeV/c) are found in Table 3.12.

3.6.12 Integral of $g_1^n(x, Q^2)$

The integral of the neutron spin structure function, $\int_0^1 g_1^n(x, Q^2)dx$, is of fundamental interest since it appears in tests of the Bjorken and Ellis-Jaffe sum rules. We will evaluate the integral at a fixed $Q_0^2 = 2$ (GeV/c)^2 which is the g_1^n weighted average Q^2 of the experiment. We find the integral in the measured region by

$$\int_{0.03}^{0.6} g_1^n(x, Q_0^2)dx = \sum_{i=1}^{8} g_1^n(x_i, Q_0^2)\Delta x_i \tag{3.39}$$

where the sum is over the eight data points, and the Δx_i are the bin widths. The quantities $g_1^n(x_i, Q_0^2)$ are calculated from equation (3.38). The statistical errors are

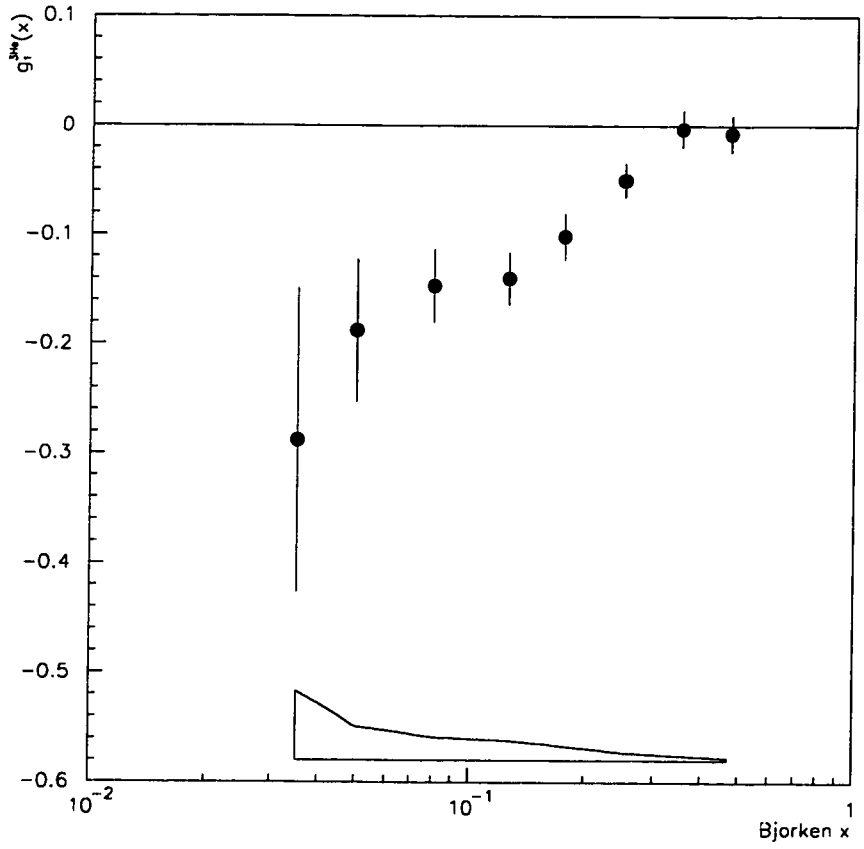

Figure 3.38: The spin dependent structure function, $g_1^{^3He}$, is shown evaluated at a fixed $Q_0^2 = 2$ (GeV/c)^2. The error bars show the statistical uncertainty, while the systematic errors are shown at the bottom of the plot.

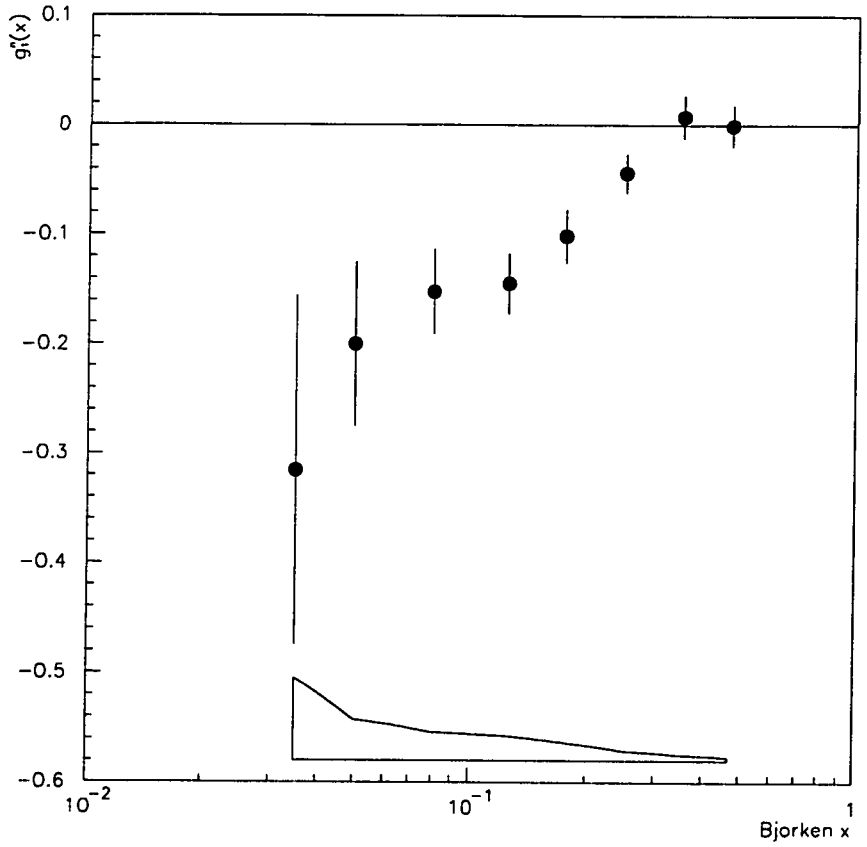

Figure 3.39: The spin dependent structure function of the neutron, g_1^n, is shown evaluated at a fixed $Q^2 = 2$ (GeV/c)^2. The error bars show the statistical uncertainty, while the systematic errors are shown at the bottom of the plot.

Parameter	Systematic Uncertainty
Beam Polarization P_b	4.1%
Target Polarization P_t	7.1%
^{3}He Dilution Factor f	8.0%
4.5° Deadtime Correction Δ_{dt}	$\Delta_{dt} \sim -3.7 \times 10^{-5} \pm 0.7 \times 10^{-5}$
7.0° Deadtime Correction Δ_{dt}	$\Delta_{dt} \sim -1.9 \times 10^{-5} \pm 0.4 \times 10^{-5}$
4.5° Radiative Corrections Δ_{RC}	25% on internal, 35% on external
7.0° Radiative Corrections Δ_{RC}	25% on internal, 25% on external
R(x,Q^2)	$\sim$ 30%
F_2(x,Q^2)	$\sim$ 4%
Neutron Polarization in ^{3}He p_n	$p_n = 0.87 \pm 0.02$
Proton Asymmetry Subtraction A_1^p	Errors from E143 [128]
Proton Polarization in ^{3}He p_p	$p_p = -0.027 \pm 0.004$
$A_\perp$	Measured uncertainty or bound from $\sqrt{R}$
A^{π^-}	Measured uncertainty from Figure 3.22
A^{e^+}	Same uncertainty as A^{π^-}
Nuclear Structure Effects	5% of A_1^n or g_1^n

Table 3.8: The uncertainties in some of the parameters used in extracting A_1^n and g_1^n are listed in this table.

Parameter	x=.035	x=.05	x=.08	x=.125	x=.175	x=.25	x=.35	x=.47
P_b	.0036	.0031	.0042	.0063	.0067	.0048	.0010	.0030
P_t	.0063	.0054	.0072	.0110	.0117	.0083	.0018	.0052
f	.0071	.0061	.0081	.0124	.0131	.0093	.0020	.0059
Δ_{dt}	.0010	.0011	.0012	.0012	.0013	.0015	.0019	.0013
Δ_{RC}	.0026	.0039	.0055	.0068	.0079	.0082	.0068	.0022
R	.0038	.0034	.0038	.0051	.0055	.0035	.0006	.0021
F_2	.0061	.0054	.0070	.0063	.0072	.0051	.0073	.0090
p_n	.0021	.0019	.0025	.0037	.0039	.0026	.0012	.0001
A_1^p	.0021	.0018	.0017	.0019	.0024	.0035	.0058	.0116
p_p	.0010	.0013	.0019	.0027	.0036	.0051	.0076	.0131
$A_\perp$	.0082	.0093	.0122	.0189	.0334	.0518	.1062	.1053
A^{π^-}	.0079	.0037	.0024	.0000	.0000	.0000	.0000	.0000
A^{e^+}	.0123	.0044	.0030	.0033	.0000	.0000	.0000	.0000
Nucl.Eff.	.0046	.0041	.0054	.0081	.0085	.0057	.0025	.0003
Total	.0218	.0166	.0209	.0298	.0415	.0552	.1072	.1075

Table 3.9: Table of systematic uncertainties on each point of A_1^n

Parameter	x=.035	x=.05	x=.08	x=.125	x=.175	x=.25	x=.35	x=.47
P_b	.0120	.0072	.0057	.0056	.0040	.0018	.0002	.0003
P_t	.0207	.0125	.0099	.0097	.0069	.0031	.0003	.0005
f	.0233	.0141	.0112	.0109	.0077	.0035	.0003	.0006
Δ_{dt}	.0034	.0027	.0017	.0011	.0008	.0006	.0004	.0002
Δ_{RC}	.0089	.0093	.0078	.0061	.0047	.0031	.0014	.0002
R	.0200	.0130	.0102	.0077	.0054	.0024	.0014	.0009
F_2	.0131	.0085	.0047	.0039	.0028	.0013	.0000	.0002
p_n	.0071	.0045	.0035	.0033	.0023	.0010	.0002	.0000
A_1^p	.0061	.0039	.0024	.0018	.0015	.0014	.0012	.0011
p_p	.0028	.0028	.0026	.0025	.0022	.0020	.0016	.0012
$A_\perp$	.0310	.0165	.0096	.0074	.0068	.0050	.0047	.0023
A^{π^-}	.0268	.0087	.0035	.0000	.0000	.0000	.0000	.0000
A^{e^+}	.0413	.0104	.0045	.0029	.0000	.0000	.0000	.0000
Nucl.Eff.	.0155	.0098	.0076	.0072	.0050	.0021	.0005	.0000
Total	.0742	.0366	.0255	.0222	.0163	.0089	.0055	.0031

Table 3.10: Table of systematic uncertainties on each point of g_1^n

x range	$\langle x \rangle$	$\langle Q^2 \rangle$ $(\mathrm{GeV/c})^2$	$A_1^{^3\mathrm{He}} \pm \delta(\mathrm{stat}) \pm \delta(\mathrm{sys})$	$g_1^{^3\mathrm{He}} \pm \delta(\mathrm{stat}) \pm \delta(\mathrm{sys})$
0.03-0.04	0.035	1.08	$-0.026 \pm .013 \pm .006$	$-0.284 \pm .140 \pm .062$
0.04-0.06	0.050	1.25	$-0.024 \pm .009 \pm .004$	$-0.184 \pm .065 \pm .030$
0.06-0.10	0.081	1.75	$-0.031 \pm .007 \pm .005$	$-0.146 \pm .034 \pm .021$
0.10-0.15	0.124	2.28	$-0.045 \pm .007 \pm .007$	$-0.138 \pm .024 \pm .018$
0.15-0.20	0.174	2.74	$-0.046 \pm .009 \pm .009$	$-0.100 \pm .021 \pm .013$
0.20-0.30	0.245	3.15	$-0.033 \pm .010 \pm .012$	$-0.048 \pm .016 \pm .007$
0.30-0.40	0.341	3.57	$-0.000 \pm .017 \pm .022$	$-0.000 \pm .017 \pm .004$
0.40-0.60	0.466	5.45	$-0.014 \pm .029 \pm .020$	$-0.007 \pm .016 \pm .002$

Table 3.11: The final results on $A_1^{^3\mathrm{He}}$ and $g_1^{^3\mathrm{He}}$ are presented, where $g_1^{^3\mathrm{He}}$ has been evaluated at $Q^2 = 2$ $(\mathrm{GeV/c})^2$.

x range	$\langle x \rangle$	$\langle Q^2 \rangle$ (GeV/c)^2	$A_1^n \pm \delta(\text{stat}) \pm \delta(\text{sys})$	$g_1^n \pm \delta(\text{stat}) \pm \delta(\text{sys})$
0.03-0.04	0.035	1.08	$-0.092 \pm .047 \pm .022$	$-0.311 \pm .160 \pm .074$
0.04-0.06	0.050	1.25	$-0.082 \pm .031 \pm .017$	$-0.195 \pm .075 \pm .037$
0.06-0.10	0.081	1.75	$-0.109 \pm .027 \pm .021$	$-0.151 \pm .039 \pm .026$
0.10-0.15	0.124	2.28	$-0.162 \pm .030 \pm .030$	$-0.143 \pm .028 \pm .022$
0.15-0.20	0.174	2.74	$-0.170 \pm .039 \pm .042$	$-0.099 \pm .025 \pm .016$
0.20-0.30	0.245	3.15	$-0.113 \pm .043 \pm .055$	$-0.042 \pm .018 \pm .009$
0.30-0.40	0.341	3.57	$+0.050 \pm .081 \pm .107$	$+0.010 \pm .020 \pm .006$
0.40-0.60	0.466	5.45	$+0.006 \pm .153 \pm .108$	$+0.000 \pm .019 \pm .003$

Table 3.12: The final results on A_1^n and g_1^n are presented, where g_1^n has been evaluated at $Q^2 = 2$ (GeV/c)^2.

added in quadrature since they are uncorrelated from one x bin to the next. This allows us to write

$$\delta(\text{stat}) = \sqrt{\sum_{i=1}^{8} (\delta_i(\text{stat})\Delta x_i)^2} \tag{3.40}$$

where δ_i(stat) is the statistical error on g_1^n in the ith bin. The total statistical error is given by $\delta(\text{stat}) = 0.056$.

Unlike the statistical errors, each systematic effect is likely to move all of the data points up or down at the same time. The total error on the integral coming from the jth systematic uncertainty, δ^j(sys), can be estimated as

$$\delta^j(\text{sys}) = \sum_{i=1}^{8} \delta_i^j(\text{sys})\Delta x_i \tag{3.41}$$

where δ_i^j(sys) is the systematic error in the ith x bin due to the jth systematic error. The total systematic error then comes by adding the δ^j(sys) in quadrature, since the systematic errors from different source should be uncorrelated. The contributions of the dominant systematic errors to the integral are given in Table 3.13 resulting in a total systematic error on the integral of 0.0060. Finally we have the result for the integral of g_1^n in the measured region :

$$\int_{0.03}^{0.6} g_1^n(x, Q_0^2)dx = -0.0284 \pm 0.0056 \text{ (stat)} \pm 0.0060 \text{ (sys)}. \tag{3.42}$$

P_b	P_t	f	Δ_{RC}	R	F_2	A_1^p	p_p	$A_\perp$	Nucl.Eff
.0012	.0021	.0024	.0016	.0021	.0010	.0009	.0010	.0032	.0015

Table 3.13: The contributions of the dominant systematic errors to the integral are listed above. The total error on the integral coming from systematic uncertainties is 0.0060.

Low x Extrapolation

We will estimate the integral in the unmeasured region, $0 < x < 0.03$, by assuming the Regge-inspired form $g_1(x \to 0) = x^{-\alpha_{a_1}}$, using the leading intercept value $\alpha_{a_1} = 0$ [122, 123]. Unfortunately, the data suffer from large statistical uncertainties at low x, so rather than base the extrapolation solely on the value of g_1^n in our lowest x bin, we will take a weighted average of g_1^n in our first two bins to reduce the statistical uncertainties. This yields the result

$$\begin{aligned} \int_0^{0.03} g_1^n(x, Q_0^2)dx &= 0.03 \times -0.216 \\ &= -0.0065 \pm 0.006. \end{aligned} \tag{3.43}$$

The error on the extrapolation is given by the variation in the result under different assumptions. Specifically, using the alternative form $g_1^n \sim a \log(1/x)$ [124] and performing the extrapolation using the first data point only, yields a low x contribution of -0.012. The assigned error of 0.006 encompasses this result, statistical errors on the low x points, and the result if we use a range in Regge intercept $\alpha_{a_1} \in (-0.5, 0)$.

High x Extrapolation

To determine the integral at high x>0.6, we fit our results for A_1^n with the constraint that $A_1^n \to 1$ as $x \to 1$. A reasonable fit to the data is given by

$$A_1^n(x) = 3.72x^{1.50}(1 - x) + x(3.81x - 2.81). \tag{3.44}$$

The high x contribution to g_1^n is then determined from

$$\int_{0.6}^1 g_1^n(x)dx = \int_{0.6}^1 A_1^n(x) \frac{F_2^n(x, Q_0^2)}{2x\,[1 + R(x, Q_0^2)]} dx. \tag{3.45}$$

The NMC structure functions are not valid for this range of x and Q^2, which falls into the resonance region. Instead we will use the F_2^n results from Whitlow [106] in the high x integral. The result is

$$\int_{0.6}^{1} g_1^n(x, Q_0^2)dx = +0.003 \pm 0.003. \tag{3.46}$$

Total Integral of $g_1^n(x, Q^2)$

Combining all of the previous results, we find

$$\Gamma_1^n(Q_0^2) = \int_0^1 g_1^n(x, Q_0^2)dx = -0.032 \ \pm \ 0.006 \text{ (stat)} \ \pm \ 0.009 \text{ (sys)}. \tag{3.47}$$

where the average Q_0^2=2.0 (GeV/c)^2.

Chapter 4

Results and Discussion

The major finding of this work is that the spin structure function of the neutron, $g_1^n(x, Q^2)$, is small and predominantly negative [125]. Most solid theoretical predictions deal with the first moment of the spin structure function, so in this section we will determine the impact of our findings on various QCD sum rules and other predictions.

4.1 Testing the Bjorken Sum Rule

The most prominent and rigorous sum rule to be tested is the Bjorken sum rule, which requires knowledge of the proton and neutron first moments, Γ_1^p, and Γ_1^n, evaluated at the same Q^2. The experimental data span a significant range in Q^2 and their evolution to a common value requires that some assumptions be made. In the following we will assume that A_1^n is independent of Q^2 and that A_2^n is consistent with zero, assumptions which are consistent with current experimental results. This allows us to determine g_1^n at fixed Q_0^2 as :

$$g_1^n(x, Q_0^2) = A_1^n(x, Q_{\rm exp}^2) \frac{F_2^n(x, Q_0^2)}{2x\,[1 + R(x, Q_0^2)]} \tag{4.1}$$

where $Q_{\rm exp}^2$ is the Q^2 at which the data were taken. To test the Bjorken sum rule we could use the excellent proton and deuteron data available from the Spin Muon Collaboration taken at CERN [126, 127]. One drawback is that their proton data are at significantly larger Q^2 than E142 (Q^2 range from 1.3 to 58 $(GeV/c)^2$, with an

Sum Rule	Experimental Data	Theoretical Prediction	Difference
Bjorken $\Gamma_1^p - \Gamma_1^n$	0.161 $\pm$ 0.015	0.171 $\pm$ 0.008	0.010 $\pm$ 0.017
Ellis-Jaffe Γ_1^n	-0.034 $\pm$ 0.011	-0.011 $\pm$ 0.005	0.023 $\pm$ 0.012

Table 4.1: Here we summarize the results of our tests of the Bjorken and Ellis-Jaffe sum rules.

average of 10 $(GeV/c)^2$). To reduce the range in Q^2 over which we are required to evolve the experimental data, we will instead use the recent and precise determination of Γ_1^p of the E143 collaboration taken at an average Q^2 of 3.0 $(GeV/c)^2$ [128].

Evaluated at a $Q_0^2 = 3$ $(GeV/c)^2$, the E142 neutron result is $\Gamma_1^n = -0.034 \pm 0.011$, and the E143 proton result is $\Gamma_1^p = 0.127 \pm 0.011$ [128], leading to $\Gamma_1^p - \Gamma_1^n = 0.161 \pm 0.015$. This is to be compared with the Bjorken sum rule prediction, $\Gamma_1^p - \Gamma_1^n = 0.171 \pm 0.008$. Here we have evaluated the QCD corrections to the sum rule to third order in $\alpha_s(Q_0^2)$ (see Chapter 1), using $\alpha_s(Q_0^2 = 3\ (GeV/c)^2) = 0.035 \pm 0.05$ [130]. Failure to include the QCD corrections would lead to a false 3 σ violation of the sum rule, indicating the importance of the perturbative corrections in our region of small average Q^2. Our major result, which has been anticipated for almost 30 years, is that the fundamental Bjorken sum rule is seen to be verified within 10% of its value. The implication is that perturbative QCD provides an excellent description of spin dependent deep inelastic scattering.

4.2 Testing the Ellis-Jaffe Sum Rule

The Ellis-Jaffe prediction for the neutron integral is $\Gamma_1^n(Q_0 = 3\ (GeV/c)^2) = -0.011 \pm 0.005$, which is about 2 σ away from the experimental result. Coupled with the larger violations of the Ellis-Jaffe proton and deuteron predictions [128, 129], the data sugggest that the underlying assumptions of SU(3) flavor symmetry in the baryon octet decays, and $\Delta s = 0$ may be in error.

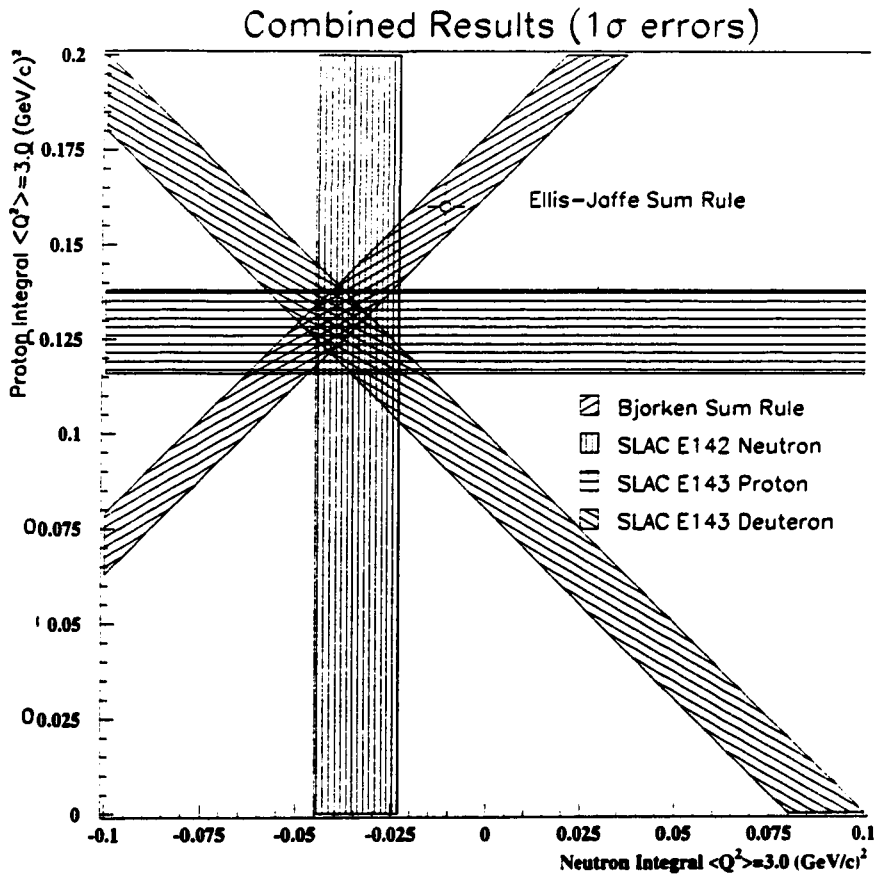

Figure 4.1: This plot illustrates the good agreement between the E142 and E143 data with the Bjorken sum rule. The Ellis-Jaffe sum rule, in contrast, is in clear disagreement with the experimental results.

4.3 Quark Contributions to the Spin

From the system of equations (1.44) of Chapter 1, we can also extract the contributions of the quarks to the spin of the nucleon. We find :

$$\begin{aligned} \Delta u &= +0.84 \pm 0.04 \\ \Delta d &= -0.41 \pm 0.04 \\ \Delta s &= -0.07 \pm 0.04 \\ \Delta\Sigma &\equiv \Delta u + \Delta d + \Delta s = 0.36 \pm 0.10. \end{aligned} \tag{4.2}$$

These last quantities should be compared with the assumption $\Delta s = 0$ of Ellis-Jaffe, and the total spin contribution $\Delta\Sigma = \Delta u + \Delta d = 3F - D = 0.579 \pm 0.032$ if $\Delta s = 0$ and SU(3) flavor symmetry is assumed in the decays of the baryon octet.

Combining these results with those of E143, as in Figure 4.2, we see a consistent picture emerging. The total quark contribution to the spin averages to $\Delta q = 0.31 \pm 0.04$ and the strange sea polarization is small and negative, $\Delta s = -0.09 \pm 0.02$.

4.4 Future Work

In the six weeks that E142 took data, a great deal was learned about the spin structure of the neutron. However, many questions remain unresolved and in need of experimental input. We might ask :

a) What is the low x behavior of g_1? Does it diverge?
b) Does $A_1(x \to 1) \to 1$ as suggested by QCD counting rules and valence quark models?
c) Will the Bjorken sum rule survive more precise tests?
d) What are the gluon and orbital angular momentum contributions to the spin?
e) What is the Q^2 dependence of the asymmetries? Will the proton asymmetry change sign as $Q^2 \to 0$ as suggested by the Drell-Hearn-Gerasimov sum rule?
f) What does g_2 look like?
g) Does the axial U(1) anomaly explain why the quark spin contribution of 30% is so low?
h) What is the magnitude of the higher twist corrections?

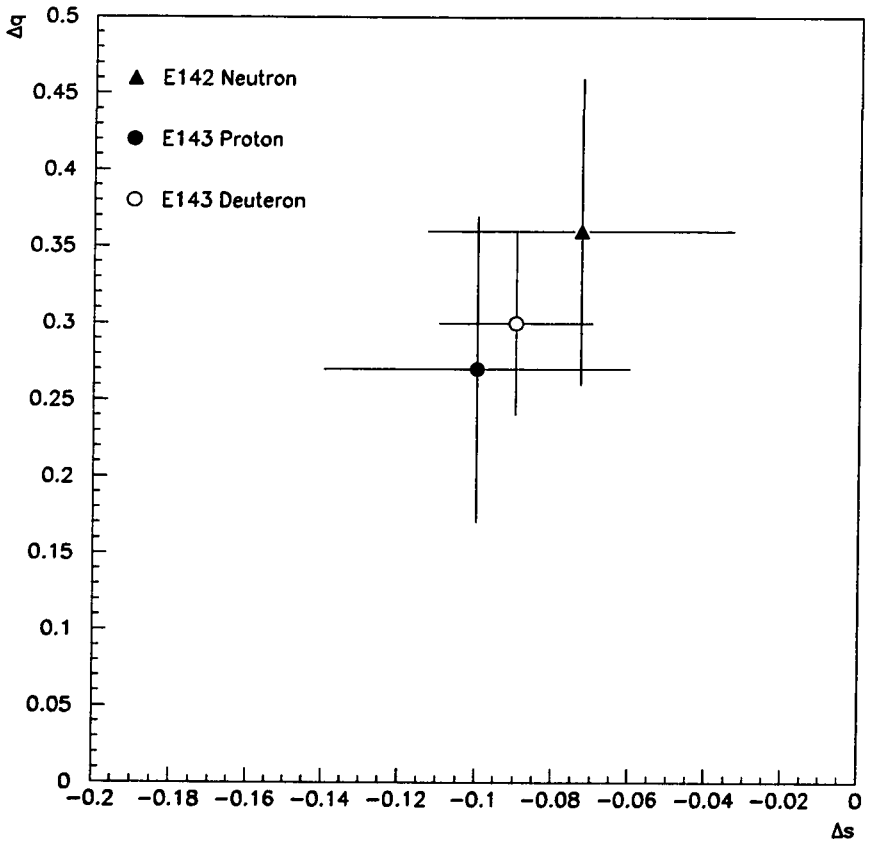

Figure 4.2: The first moments Γ_1^n, Γ_1^p, and Γ_1^d were used to extract the total quark contribution to the spin of the nucleon, Δq, and the strange sea contribution, Δs.

The answers to these questions will have a broad impact in high energy physics. Precision measurements of Γ_1^n, Γ_1^p, and Γ_1^d, assuming the validity of the Bjorken sum rule, can be used to determine the strong coupling constant α_s, and even can be used to set limits on parameters involved in dark matter searches [131].

The ambitious experimental programs of the next few years should shed some light on these issues. The HERMES experiment at DESY will cover a similar kinematic region to the recent SLAC experiments, with the advantage of having pure gas targets with dilution factor close to unity [132]. Measurements of semi-inclusive asymmetries by HERMES may yield additional information on Δg and Δs.

The SLAC program will continue with experiments E154 and E155 which seek to measure the spin structure functions with a 50 GeV/c beam [133, 134]. The increase in precision and kinematic range of the data should be substantial.

The SMC experiment at CERN will continue to collect data in 1995 and 1996, improving in particular the precision of the low x spin structure function data. Some time will also be dedicated to measuring g_2.

At CEBAF, experiments will be underway within the next few years to test the Drell-Hearn-Gerasimov sum rule, and determine the high x behavior of the asymmetry, A_1^n [135, 136].

In the not-too-distant future, DESY may operate with polarized protons, which will extend the kinematic range of the spin structure functions by orders of magnitude. Polarized proton collisions at RHIC hold out the possibility of determining Δg.

The future of spin physics looks very exciting, and will be followed with great interest by the author.

Appendix A

The Bjorken and Ellis-Jaffe Sum Rules

In this appendix we will derive the Bjorken and Ellis-Jaffe sum rules in the framework of the operator product expansion. Most of the elements in the derivation can be found in the literature [137, 138, 139, 140].

The starting point is to consider the expansion of the time-ordered product of two vector current operators. The current operator is given by the sum over flavors i, $J^\mu = \sum Q_i \bar{q}_i \gamma^\mu q_i$. Dropping the flavor index and quark charge, Q_i for convenience, we then use Wick's theorem to expand the time ordered product :

$$\begin{aligned} T\left[J^\mu(x)\, J^\nu(0)\right] \;=\; & -Tr\left[\langle 0|T\left[q(0)\,\bar{q}(x)\right]|0\rangle \gamma^\mu \langle 0|T\left[q(x)\,\bar{q}(0)\right]|0\rangle \gamma^\nu\right] + \\ & :\bar{q}(x)\,\gamma_\mu \langle 0|T\left[q(x)\,\bar{q}(0)\right]|0\rangle \gamma_\nu q(0): + \\ & :\bar{q}(0)\,\gamma_\nu \langle 0|T\left[q(0)\,\bar{q}(x)\right]|0\rangle \gamma_\mu q(x): + \\ & :\bar{q}(x)\,\gamma_\mu q(x)\,\bar{q}(0)\,\gamma_\nu q(0):. \end{aligned} \tag{A.1}$$

Following Shuryak and Vainshtein [140], we use Schwinger's coordinate representation for the propagator. In the limit of massless quarks we can write the Dirac equation in the form $i\not{\partial} q = 0$, so that the free fermion propagator takes the form

$$i\langle 0|T\left[q(x)\,\bar{q}(y)\right]|0\rangle = G(x,y) = \langle x|\frac{1}{\not{p}}|y\rangle. \tag{A.2}$$

which formally satisfies the requirements for a Green's function :

$$i\not{\partial} G(x,y) = \langle x|y\rangle = \delta^4(x-y). \tag{A.3}$$

Using $[P_\mu, e^{iq\cdot x}] = -q_\mu e^{iq\cdot x}$ which implies $e^{iq\cdot x}P_\mu = (P_\mu + q_\mu)\, e^{iq\cdot x}$, and $e^{iq\cdot x}|0\rangle = |0\rangle$, then we can write the momentum space representation of the propagator as

$$\begin{aligned} G(q) &= \int d^4x e^{iq\cdot x}\langle x|\frac{1}{\not P}|0\rangle \\ &= \int d^4x\langle x|\frac{1}{\not P + \not q}|0\rangle \\ &= \int d^4x\langle x|\frac{i\not\partial + \not q}{(i\partial + q)^2}|0\rangle. \end{aligned} \tag{A.4}$$

The leading contributions to the time ordered product in (A.1) come from the second and third terms in the expansion. Using the results above for the propagator, the momentum space expansion of these terms, which constitutes the forward virtual Compton scattering amplitude, takes the form :

$$\begin{aligned} T^{\mu\nu} &= \int d^4x e^{iq\cdot x} T\left[J^\mu(+\tfrac{x}{2})J^\nu(-\tfrac{x}{2})\right] \\ &= \int d^4x e^{iq\cdot x}\Big[\bar q(+\tfrac{x}{2})\gamma_\mu\langle 0|T\left[q(+\tfrac{x}{2})\bar q(-\tfrac{x}{2})\right]|0\rangle\gamma_\nu q(-\tfrac{x}{2}) + \\ &\qquad \bar q(-\tfrac{x}{2})\gamma_\nu\langle 0|T\left[q(-\tfrac{x}{2})\bar q(+\tfrac{x}{2})\right]|0\rangle\gamma_\mu q(+\tfrac{x}{2})\Big] \\ &= \int d^4x\Big[e^{+iq\cdot x}\bar q(+\tfrac{x}{2})\gamma_\mu\langle 0|T\left[q(+\tfrac{x}{2})\bar q(-\tfrac{x}{2})\right]|0\rangle\gamma_\nu q(-\tfrac{x}{2}) + \\ &\qquad e^{-iq\cdot x}\bar q(+\tfrac{x}{2})\gamma_\nu\langle 0|T\left[q(+\tfrac{x}{2})\bar q(-\tfrac{x}{2})\right]|0\rangle\gamma_\mu q(-\tfrac{x}{2})\Big] \\ &= \int d^4x\left[\bar q(+\tfrac{x}{2})\gamma_\mu\langle +\tfrac{x}{2}|\frac{1}{\not P + \not q}|-\tfrac{x}{2}\rangle\gamma_\nu q(-\tfrac{x}{2}) + \bar q(+\tfrac{x}{2})\gamma_\nu\langle +\tfrac{x}{2}|\frac{1}{\not P - \not q}|-\tfrac{x}{2}\rangle\gamma_\mu q(-\tfrac{x}{2})\right] \\ &= \int d^4x\left[\bar q(+\tfrac{x}{2})\gamma^\mu\frac{i\not\partial + \not q}{(i\partial + q)^2}\gamma^\nu q(-\tfrac{x}{2}) + \bar q(+\tfrac{x}{2})\gamma^\nu\frac{i\not\partial - \not q}{(i\partial - q)^2}\gamma^\mu q(-\tfrac{x}{2})\right]\delta^4\left(\tfrac{x}{2} - -\tfrac{x}{2}\right) \\ &= \bar q(0)\gamma^\mu\frac{i\not\partial + \not q}{(i\partial + q)^2}\gamma^\nu q(0) + \bar q(0)\gamma^\nu\frac{i\not\partial - \not q}{(i\partial - q)^2}\gamma^\mu q(0). \end{aligned} \tag{A.5}$$

This last expression corresponds to the two diagrams in Figure A.1. In the limit of large momentum transfer, we can expand the denominator of the propagator as

$$\begin{aligned} \frac{1}{(i\partial \pm q)^2} &= -\frac{1}{Q^2}\sum_{n=0}^{\infty}\left(\frac{\pm 2iq\cdot\partial - \partial^2}{Q^2}\right)^n \\ &\simeq -\frac{1}{Q^2}\sum_{n=0}^{\infty}\left(\frac{\pm 2iq\cdot\partial}{Q^2}\right)^n \end{aligned} \tag{A.6}$$

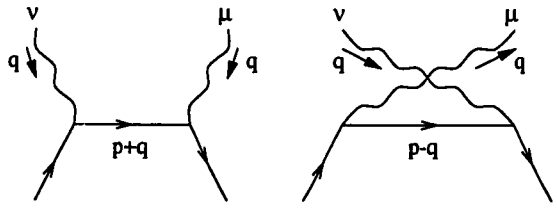

Figure A.1: The two lowest order diagrams in virtual Compton scattering contributing to the current operator product are shown.

so that that the expansion takes the form :

$$T^{\mu\nu} = -\bar{q}\frac{1}{Q^2}\sum_{n=0}^{\infty}\left(\frac{2iq\cdot\partial}{Q^2}\right)^n\left[(i\partial_\alpha + q_\alpha)(\gamma^\mu\gamma^\alpha\gamma^\nu) + (-1)^n(i\partial_\alpha - q_\alpha)(\gamma^\nu\gamma^\alpha\gamma^\mu)\right]q.$$

If we substitute the identity $\gamma^\mu\gamma^\alpha\gamma^\nu = g^{\mu\alpha}\gamma^\nu + g^{\nu\alpha}\gamma^\mu - g^{\mu\nu}\gamma^\alpha + i\epsilon^{\mu\nu\alpha\beta}\gamma_\beta\gamma_5$ then

$$\begin{aligned} T^{\mu\nu} = & -\bar{q}\frac{1}{Q^2}\sum_{n=0}^{\infty}\left(\frac{2iq\cdot\partial}{Q^2}\right)^n \times \\ & \Big[(i\partial^\mu + q^\mu)\gamma^\nu + (i\partial^\nu + q^\nu)\gamma^\mu - g^{\mu\nu}(i\not{\partial} + \not{q}) + i\epsilon^{\mu\nu\alpha\beta}(i\partial_\alpha + q_\alpha)\gamma_\beta\gamma_5 + \\ & \quad (i\partial^\mu - q^\mu)\gamma^\nu + (i\partial^\nu - q^\nu)\gamma^\mu - g^{\mu\nu}(i\not{\partial} - \not{q}) - \\ & \quad i\epsilon^{\mu\nu\alpha\beta}(i\partial_\alpha - q_\alpha)\gamma_\beta\gamma_5\Big]\Big]q. \end{aligned} \tag{A.7}$$

The Dirac equation implies (for massless quarks) that $g^{\mu\nu}i\not{\partial}q = 0$. The terms like $\bar{q}i\epsilon^{\mu\nu\alpha\beta}i\partial_\alpha\gamma_\beta\gamma_5 q$ are proportional to $\epsilon^{\mu\nu\alpha\beta}p_\alpha p_\beta$ and vanish, leaving the simplified expression :

$$\begin{aligned} T^{\mu\nu} = & -\bar{q}\frac{1}{Q^2}\sum_{n=0}^{\infty}\left(\frac{2iq\cdot\partial}{Q^2}\right)^n\Big[[1+(-1)^n]\left[i\partial^\mu\gamma^\nu + i\partial^\nu\gamma^\mu + i\epsilon^{\mu\nu\alpha\beta}q_\alpha\gamma_\beta\gamma_5\right] + \\ & [1-(-1)^n]\left[q^\mu\gamma^\nu + q^\nu\gamma^\mu - g^{\mu\nu}\not{q}\right]\Big]q \end{aligned} \tag{A.8}$$

We now restrict our attention to the antisymmetric part of the expansion. Replacing $i\partial$ by the gauge-invariant iD, and defining the local spin $n+1$ operator

$$\Theta_{A\mu}^{\mu_1\mu_2\cdots\mu_n} = \tfrac{1}{2}\bar{q}(0)\gamma_\mu\gamma_5 iD^{\mu_1}iD^{\mu_2}\cdots iD^{\mu_n}q(0) \tag{A.9}$$

we find

$$
\begin{aligned}
T_A^{\mu\nu} &= \frac{2}{Q^2}\sum_{n=0}^{\infty}\frac{2^n q_{\mu_1}q_{\mu_2}\cdots q_{\mu_n}}{(Q^2)^n}\Big[[1+(-1)^n]\,i\epsilon^{\mu\nu\alpha\beta}q_\alpha\Theta_{A\beta}^{\mu_1\mu_2\cdots\mu_n}\Big] \\
&= \frac{2}{Q^2}\sum_{n=0,2,4,\ldots}^{\infty}2\frac{2^n q_{\mu_1}q_{\mu_2}\cdots q_{\mu_n}}{(Q^2)^n}\Big[i\epsilon^{\mu\nu\alpha\beta}q_\alpha\Theta_{A\beta}^{\mu_1\mu_2\cdots\mu_n}\Big] \\
&= \sum_{n=1,3,5,\ldots}^{\infty}2\frac{2^n q_{\mu_2}q_{\mu_3}\cdots q_{\mu_n}}{(Q^2)^n}\Big[i\epsilon^{\mu\nu\alpha\beta}q_\alpha\Theta_{A\beta}^{\mu_2\mu_3\cdots\mu_n}\Big] \\
&= \sum_{n=1,3,5,\ldots}^{\infty}2\frac{2^n q_{\mu_2}q_{\mu_3}\cdots q_{\mu_n}}{(Q^2)^n}\Big[i\epsilon^{\mu\nu\alpha\beta}q_\alpha C_n^3(Q^2/\mu^2,\alpha_s)\Theta_{A\beta}^{\mu_2\mu_3\cdots\mu_n}\Big].
\end{aligned}
$$

In the last line we have introduced the Wilson coefficients, C_n^3. These terms incorporate the effects of higher order diagrams, and are dependent on the renormalization scale, μ^2, at which the operators are defined. A straightforward dimensional analysis shows that the leading contributions to the scattering amplitude come from the operators of lowest twist, where the twist is given by the dimension-spin of the operator. The matrix elements of the operators, Θ, are not known, but they will at least be functions of the tensors P_α, S_α, g_{α_1,α_2} and the invariants we can make from them. This suggests that placing the operator between nucleon states yields the general form

$$
\begin{aligned}
&\langle P,S|\Theta_{A\beta}^{\mu_2\mu_3\cdots\mu_n}|P,S\rangle = \\
&= \frac{1}{n}A_n\left[S_\beta P^{\mu_2}P^{\mu_3}\ldots P^{\mu_n}+S^{\mu_2}P_\beta P^{\mu_3}\ldots P^{\mu_n}+S^{\mu_2}P^{\mu_3}P_\beta\ldots P^{\mu_n}+\cdots\right]+ \\
&\quad B_n\left[S_\beta g^{\mu_2\mu_3}P^2P^{\mu_4}\ldots P^{\mu_n}+\ldots\right] \\
&\approx A_nS_\beta P^{\mu_2}P^{\mu_3}\ldots P^{\mu_n}-\left(\frac{n-1}{n}\right)A_nS_\beta P^{\mu_2}P^{\mu_3}\ldots P^{\mu_n}+ \\
&\quad \frac{1}{n}\left[S^{\mu_2}P_\beta P^{\mu_3}\ldots P^{\mu_n}+S^{\mu_2}P^{\mu_3}P_\beta\ldots P^{\mu_n}+\cdots\right] \qquad \text{(A.10)}
\end{aligned}
$$

where the expression is symmetric in the μ_i, and the coefficients A and B will be functions of the invariants. In going to the last equation we have neglected the contributions of the trace terms, known as the target mass corrections. This is justifiable since their contribution to the matrix elements is suppressed by terms of order $P^2/Q^2 = M^2/Q^2$ compared to the leading terms. Substituting this matrix element into the expansion for $T_A^{\mu\nu}$ yields :

$$
T_A^{\mu\nu} = \sum_{n=1,3,5,\ldots}^{\infty}2\frac{2^n}{(Q^2)^n}i\epsilon^{\mu\nu\alpha\beta}q_\alpha C_n^3\Big[A_nS_\beta\,(P\cdot q)^{n-1}-\left(\frac{n-1}{n}\right)A_nS_\beta\,(P\cdot q)^{n-1}+
$$

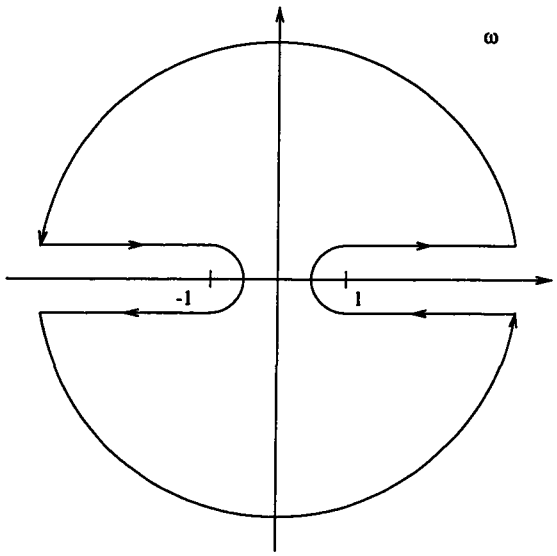

Figure A.2: Contour path integral used in the complex ω plane

$$\left(\frac{n-1}{n}\right) A_n P_\beta S{\cdot}q\,(P{\cdot}q)^{n-2}\Big]$$

$$= \frac{2}{P{\cdot}q} i\epsilon^{\mu\nu\alpha\beta} q_\alpha \sum_{n=1,3,5,\ldots}^{\infty} C_n^3 \left[S_\beta A_n \omega^n - \left[S_\beta - P_\beta \frac{S{\cdot}q}{P{\cdot}q}\right]\left(\frac{n-1}{n}\right) A_n \omega^n\right]$$

$$= \frac{1}{P{\cdot}q} i\epsilon^{\mu\nu\alpha\beta} q_\alpha \left[S_\beta \tilde{g}_1 + \left[S_\beta - P_\beta \frac{S{\cdot}q}{P{\cdot}q}\right] \tilde{g}_2\right]. \qquad \text{(A.11)}$$

where $\omega = 2P{\cdot}q/Q^2$ and we have defined the two structure functions

$$\tilde{g}_1 = \sum_{n=1,3,5,\ldots}^{\infty} 2C_n^3 A_n \omega^n, \qquad \tilde{g}_2 = \sum_{n=1,3,5,\ldots}^{\infty} \left(\frac{1-n}{n}\right) 2C_n^3 A_n \omega^n. \qquad \text{(A.12)}$$

The series converge for $|\omega| < 1$, corresponding to a kinematically unphysical and inaccessible region. To make contact with the physical region we need to use the optical theorem and the analyticity of the virtual Compton amplitude. Consider the contour integral in Figure A.2. Using the crossing relation $T_A^{\mu\nu}(-\omega) = -T_A^{\mu\nu}(\omega)$ we find :

$$\frac{1}{2\pi i}\oint \frac{d\omega}{\omega^m} T_A^{\mu\nu} = \frac{2}{2\pi i}\int_1^\infty \frac{d\omega}{\omega^m}\left[T_A^{\mu\nu}(\omega + i\varepsilon) - T_A^{\mu\nu}(\omega - i\varepsilon)\right]$$

$$= 4\int_1^\infty \frac{d\omega}{\omega^m} W_A^{\mu\nu}. \qquad \text{(A.13)}$$

Here we have used the optical theorem to relate $W^{\mu\nu}$ to the absorptive part of the forward virtual Compton amplitude via

$$W_A^{\mu\nu} = \frac{1}{2\pi}\text{Abs}\ T_A^{\mu\nu} \equiv \frac{1}{2\pi}\frac{1}{2i}\left[T_A^{\mu\nu}(\omega + i\varepsilon) - T_A^{\mu\nu}(\omega - i\varepsilon)\right]. \tag{A.14}$$

Now consider the L.H.S. of equation (A.13) which takes the form :

$$\begin{aligned} &= \frac{1}{2\pi i}\oint \frac{d\omega}{\omega^m}\frac{2}{P\cdot q} i\epsilon^{\mu\nu\alpha\beta} q_\alpha \sum_n \left[S_\beta C_n^3 A_n \omega^n + \left[S_\beta - P_\beta \frac{S\cdot q}{P\cdot q}\right] C_n^3 A_n \omega^n \left(\frac{1-n}{n}\right)\right] \\ &= \frac{2}{P\cdot q} i\epsilon^{\mu\nu\alpha\beta} q_\alpha \sum_n \left[S_\beta C_n^3 A_n \delta_{m,n+1} + \left[S_\beta - P_\beta \frac{S\cdot q}{P\cdot q}\right] C_n^3 A_n \left(\frac{1-n}{n}\right)\delta_{m,n+1}\right] \end{aligned} \tag{A.15}$$

where we have used the result that

$$\frac{1}{2\pi i}\oint \frac{d\omega}{\omega^m}\omega^n = \delta_{m,n+1}. \tag{A.16}$$

Setting $x = 1/\omega$, we can rewrite the R.H.S. of (A.13) as

$$4\int_1^\infty \frac{d\omega}{\omega^m} W_A^{\mu\nu} = 4\int_0^1 dx x^{m-2} W_A^{\mu\nu} \tag{A.17}$$

Setting $m = 2$ in equation (A.15) and using

$$W_A^{\mu\nu} = \frac{1}{P\cdot q} i\epsilon^{\mu\nu\alpha\beta} q_\alpha \left[S_\beta g_1 + \frac{1}{P\cdot q}\left[S_\beta (P\cdot q) - P_\beta (S\cdot q)\right] g_2\right], \tag{A.18}$$

yields the famous result

$$\int_0^1 dx g_1(x, Q^2) = \frac{1}{2} C_1^3(Q^2/\mu^2, \alpha_s) A_1. \tag{A.19}$$

The interpretation of this result is straightforward. Re-inserting the sum over quark flavors, and including the quark charge squared (which we dropped initially) we can write the matrix element for the proton :

$$\begin{aligned} 2S^\mu A_1 &= \langle P,S|\frac{4}{9}\bar{u}\gamma^\mu\gamma^5 u + \frac{1}{9}\bar{d}\gamma^\mu\gamma^5 d + \frac{1}{9}\bar{s}\gamma^\mu\gamma^5 s|P,S\rangle \\ &= \frac{1}{2}\langle P,S|\frac{4}{9}[\bar{u}\gamma^\mu(1+\gamma^5)u - \bar{u}\gamma^\mu(1-\gamma^5)u] + \\ &\qquad \frac{1}{9}[\bar{d}\gamma^\mu(1+\gamma^5)d - \bar{d}\gamma^\mu(1-\gamma^5)d] + \\ &\qquad \frac{1}{9}[\bar{s}\gamma^\mu(1+\gamma^5)s - \bar{s}\gamma^\mu(1-\gamma^5)s]|P,S\rangle \end{aligned}$$

$$
\begin{aligned}
&= \frac{1}{2}\,\langle P,S|\frac{4}{9}[\bar{u}_R\gamma^\mu u_R - \bar{u}_L\gamma^\mu u_L] + \frac{1}{9}[\bar{d}_R\gamma^\mu d_R - \bar{d}_L\gamma^\mu d_L] + \\
&\qquad \frac{1}{9}[\bar{s}_R\gamma^\mu s_R - \bar{s}_L\gamma^\mu s_L]|P,S\rangle \\
&\equiv \frac{1}{2}\,\left[\frac{4}{9}\Delta u + \frac{1}{9}\Delta d + \frac{1}{9}\Delta s\right] \qquad \text{(A.20)}
\end{aligned}
$$

In terms of the parton model, we can write the Δq in terms of parton distributions :

$$
\Delta q = \int_0^1 dx\,[q_+(x) - q_-(x) + \bar{q}_+(x) - \bar{q}_-(x)]\,. \qquad \text{(A.21)}
$$

Now we can turn our attention to the sum rules. The singlet and non-singlet combinations of the Δq can be written in terms of the F and D constants measured in the decays of the baryon octet. The non-singlet combination $\Delta u - \Delta d$ measured in neutron beta decay is given by the axial vector decay constant, g_A:

$$
\Delta u - \Delta d = F + D = g_A \qquad \text{(A.22)}
$$

Isospin symmetry allows us to write :

$$
\begin{aligned}
\int_0^1 \left[g_1^p(x,Q^2) - g_1^n(x,Q^2)\right] dx &= \frac{1}{2}C_1^3(Q^2)[\frac{4}{9}\Delta u + \frac{1}{9}\Delta d + \frac{1}{9}\Delta s - \\
&\qquad \frac{1}{9}\Delta u - \frac{4}{9}\Delta d - \frac{1}{9}\Delta s] \\
&= \frac{1}{2}C_1^3(Q^2)\,[\Delta u - \Delta d] \\
&= \frac{1}{2}|g_A|C_1^3(Q^2) \qquad \text{(A.23)}
\end{aligned}
$$

which is the famous Bjorken sum rule (g_V is traditionally taken as unity). The QCD radiative corrections to the sum rule, C_1^3, are given in Chapter One.

If we make the further assumptions that SU(3) flavor symmetry is upheld in the baryon octet decays, and that the strange sea is unpolarized, $\Delta s = 0$, we can derive the Ellis-Jaffe sum rules for the proton and neutron. Using the definitions for the non-singlet and singlet terms

$$
\begin{aligned}
\Delta u + \Delta d - 2\Delta s &= 3F - D \\
\Delta u + \Delta d + \Delta s &\equiv \Delta\Sigma \qquad \text{(A.24)}
\end{aligned}
$$

yields the sum rules for the proton and neutron

$$\int_0^1 g_1^p(x,Q^2)dx = C_1^3(Q^2)\left[+\frac{1}{12}(F+D)+\frac{1}{36}(3F-D)\right]+\frac{1}{9}C_1^0(Q^2)\Delta\Sigma$$
$$\int_0^1 g_1^n(x,Q^2)dx = C_1^3(Q^2)\left[-\frac{1}{12}(F+D)+\frac{1}{36}(3F-D)\right]+\frac{1}{9}C_1^0(Q^2)\Delta\Sigma \tag{A.25}$$

where the singlet and non-singlet QCD radiative corrections, C_1^0 and C_1^3, are given in Chapter One.

References

[1] V. H. Hughes and J. Kuti, Ann. Rev. Nucl. Sci **33**, 611 (1983).

[2] J. D. Bjorken, Phys. Rev. **148**, 1467, (1966).

[3] P. Roy, *Theory of Lepton-Hadron Processes at High Energies*, Clarendon Press, 1975.

[4] A. J. G. Hey and J. E. Mandula, Phys. Rev. D**5**, 2610 (1972).

[5] C. E. Carlson and Wu-Ki Tung, Phys. Rev. D**5**, 721 (1972).

[6] A. J. G. Hey,*High Energy Leptonic Interactions : Proceedings of 9th Rencontre de Moriond* (Ed. J. Tran Thanh Van), CNRS France, 1974.

[7] R. F. Oppenheim, Ph. D. Thesis, Yale University, 1982.

[8] M. G. Doncel and E. de Rafael, Nuovo Cimento **4A**, 363 (1971).

[9] J. D. Bjorken, in *Proceedings of the 3rd International Symposium on Electron and Photon Interactions*, Stanford, Californina, 1967.

[10] R. P. Feynman, Phys. Rev. Lett. **23**, 1415 (1969).

[11] J. D. Bjorken and E. A. Paschos, Phys. Rev. **185**, 1975 (1969).

[12] R. P. Feynman, *Photon-Hadron Interactions*, W. A. Benjamin, Reading Mass., 1972.

[13] J. D. Bjorken, Phys. Rev. **148**, 1467 (1966), J. D. Bjorken, Phys. Rev. **D1**, 1376 (1970).

[14] J. Kodaira *et al.*, Nucl. Phys. **B159**, 99 (1979).

[15] S. A. Larin and J. A. M. Vermaseren, Phys. Lett. **B259**, 345 (1991).

[16] S. A. Larin, Phys. Lett. **B334**, 192 (1994).

[17] J. Ellis and R. L. Jaffe, Phys. Rev. **D9** 1444 (1974), erratum Phys. Rev. **D10** 1669 (1974).

[18] F. E. Close and R. G. Roberts, Phys. Lett. **B316** 165 (1993).

[19] S. Brodsky, M. Burkardt and I. Schmidt, SLAC-PUB-6087, 1994.

[20] G. Altarelli and G. Parisi, Nucl. Phys. B *126*, 298 (1977).

[21] G. Farrar and D. Jackson, Phys. Rev. Lett. **35**, 1416 (1975).

[22] F. E. Close, *An Introduction to Quarks and Partons*, Academic Press, New York, 1979.

[23] S. D. Drell and T. Yan, Phys. Rev. Lett. **24**, 181 (1970).

[24] G. West, Phys. Rev. Lett. **24**, 1206 (1970).

[25] R. L. Heimann, Nucl. Phys. **B64**, 429 (1973).

[26] B. Badelek *et. al.*, Rev. Mod. Phys. **64**, 927 (1992).

[27] F. E. Close and R. G. Roberts, Phys. Lett.*B336*, 257 (1994).

[28] J. Ellis and M. Karliner, Phys. Lett. **B213**, 73 (1988).

[29] H1 Collaboration, I. Abt *et al.*, Nucl. Phys. **B407**, 515 (1993); ZEUS Collaboration, M. Derrick *et al.*, Phys. Lett.*B316*, 412 (1993).

[30] S. D. Bass and P. V. Landshoff, Phys. Lett. **B336**, 537 (1994).

[31] A. Schäfer, Phys. Lett. **B208**, 175 (1988).

[32] J. L. Friar *et al.*, Phys. Rev. C textbf42, 2310 (1990).

[33] I. R. Afnan and N. D. Birrell, Phys. Rev. C **16**, 823 (1977).

[34] G. Derrick and J. M. Blatt, Nucl. Phys. **8**, 310 (1958).

[35] B. Blankleider and R. M. Woloshyn, Phys. Rev. C **29**, 538 (1984).

[36] C. Ciofi degli Atti *et al.*, Phys. Rev. C **48**, R968 (1993).

[37] R. M. Woloshyn, Nucl. Phys. **A496**, 749 (1989).

[38] G. Altarelli and G. G. Ross, Phys. Lett. **B212**, 391 (1988).

[39] B. Ioffe, ITEP-61(1994) preprint.

[40] I. I. Balitsky, V. M. Braun and A. V. Koleschnichenko, Phys. Lett. **B242**, 245 (1990), erratum **B318** 648 (1993).

[41] M. Woods *et al.*, SLAC-PUB-5965, December 1992.

[42] A. D. Yeremian *et al.*, SLAC-PUB-6074, March 1993.

[43] T. Maruyama *et al.*, J. Appl. Phys. **73**, 5189 (1993).

[44] D. T. Pierce and F. Meier, Phys. Rev. B **13**, 5484 (1976).

[45] M. Woods, SLAC-PUB-6694, January 1995.

[46] T. Maruyama *et al.*, Phys. Rev. B **46**, 4261 (1992).

[47] M. Woods, *Generation of Positive or Negative Helicity Laser Light by the Fresnel/Zolotorev Method*, SLD Note 223, October 1992.

[48] H. Band, R. Prepost and M. Woods, *Electron Beam Helicity Experiment*, SLD Note 224, January 1993.

[49] R. B. Neal, *The Stanford Two Mile Accelerator*, Benjamin, New York, 1968.

[50] L. Tao, Ph. D. Thesis, American University, 1994.

[51] P. Cooper *et al.*, Phys. Rev. Lett. **42**, 1386 (1979).

[52] C. Møller, Ann. Phys. **14**, 532 (1932).

[53] H. R. Band, R. Prepost, *Møller Target Design and Foil Polarization Measurements*, SLCPOL Note 22, 1988.

[54] H. R. Band, *Møller Polarimetry at SLAC*, 1994.

[55] R. Prepost, E143 Technical Note # 65, 1994.

[56] L. G. Levchuk, Nucl. Instr. and Meth. **A345**, 496 (1994).

[57] F. D. Colegrove, L. D. Shearer, and G. K. Walters, Phys. Rev. **132**, 2561 (1963).

[58] M. A. Bouchiat, T. R. Carver, and C. M. Varnum, Phys. Rev. Lett. **5**, 373 (1960).

[59] R. L. Gramblin and T. R. Carver, Phys. Rev. **A138**, 946 (1965).

[60] N. D. Bhaskar, W. Happer, and T. McClelland, Phys. Rev. Lett. **49**, 25 (1982).

[61] W. Happer *et al.*, Phys. Rev. **A29**, 3092 (1984).

[62] N. R. Newbury *et al.*, Phys. Rev. Lett. **67**, 3219 (1991).

[63] T. E. Chupp *et al.*, Phys. Rev. **C45**, 915 (1992).

[64] B. Larson *et al.*, Phys. Rev. Lett. **67**, 3356 (1993).

[65] R. G. Milner, R. D. McKeown, and C. E. Woodward, Nucl. Instr. and Meth. **A274**, 56 (1989).

[66] H. L. Middleton, Ph. D. Thesis, Princeton Univerisity, 1994.

[67] M. Wagshul, Ph. D. Thesis, Harvard Universiy, 1991.

[68] R. M. Herman, Phys. Rev. **A137**, 1062 (1965).

[69] T. G. Walker, Phys. Rev. **A40**, 4959 (1989).

[70] K. P. Coulter, Ph. D. Thesis, Princeton University, 1989.

[71] K. D. Bonin, T. G. Walker, and W. Happer, Phys. Rev. **A37**, 3270 (1988).

[72] T. E. Chupp *et al.*, Phys. Rev. **C45**, 915 (1992).

[73] R. M. Sternheimer, M. J. Berger, and S. M. Seltzer, *Atomic Data and Nuclear Data Tables* **30**, 262 (1984).

[74] K. P. Coulter *et al.*, Nucl. Instr. and Meth. **A276**, 29 (1989).

[75] G. G. Petratos *et al.*, SLAC-PUB 5698, 1991.

[76] J. Dunne, Pre-Thesis Project (unpublished), American University, 1994.

[77] K. L. Brown, SLAC Report 75, 1982.

[78] P. Baillon *et al.*, Nucl. Instr. and Meth. **A276**, 492 (1989).

[79] P. Baillon *et al.*, Nucl. Instr. and Meth. **A126**, 13 (1975).

[80] E. L. Garwin, Y. Tomkiewicz and D. Trines, Nucl. Instr. and Meth. **107**, 365 (1973).

[81] Y. Tomkiewicz and E. L. Garwin, SLAC-PUB 1356, 1973.

[82] P. J. Carlson, Nucl. Instr. and Meth. **158**, 403 (1979).

[83] A. M. Gorin *et al.*, Nucl. Instr. and Meth. **A251**, 461 (1986).

[84] *Burle Photomultiplier Handbook*, 1989.

[85] E. R. Hayes *et al.*, Argonne ANL-6916, 1964.

[86] J. Xu, Ph.D. Thesis, Syracuse University, 1994.

[87] P. A. Souder, *Proposal to Build Hodoscopes for E142*, 1990.

[88] G. T. Bartha *et al.*, Nucl. Instr. and Meth. **A375**, 59 (1989).

[89] Y. Roblin, Ph. D Thesis, Université Blaise Pascal, 1995.

[90] M. S. Spengos, A Description of the Trigger Electronics System for E142, Pre-Thesis Project, American Univeristy, 1993.

[91] *Burle Photomultiplier Handbook*, 1989

[92] B. Rossi, *High Energy Particles*, Prentice-Hall, New York, 1952.

[93] E. Longo and I. Sestili, Nucl. Instr. and Meth. **46**, 283 (1975).

[94] Y. S. Tsai, Rev. Mod. Phys **46**, 319 (1965).

[95] T. Ferbel, *Experimental Techniques in High Energy Physics*, Addison-Wesley, Menlo Park, 1987.

[96] K. L. Brown, SLAC Report 75, 1982.

[97] G. G. Petratos *et al.*, SLAC-PUB-5698, 1991.

[98] V. Breton, Y. Roblin and F. Tamin, *A Cellular Automaton for Cluster Recognition in the Shower Counter*, E142 Internal Note, 1993.

[99] V. Breton, private communication.

[100] K. Pinkau, Phys. Rev. **139**, B1548 (1969).

[101] T. Yuda, Nucl. Instr. and Meth. **73**, 301 (1969).

[102] H. Borel *et al., Shower Counters for SLAC experiments E142/E143*, E142/E143 Internal Note, 1994.

[103] V. Breton and Philippe Grenier, *Use of Neural Networks for Particle Identification*, E142 Internal Note, 1993.

[104] J. Gomez *et al.*, Phys. Rev. **D49**, 4348 (1994).

[105] P. Amaudruz *et al.*, Phys. Lett. **B294**, 120 (1992).

[106] L. Whitlow, SLAC Report 357, 1990.

[107] A. C. Venuti *et al.*, Phys. Lett. **B223**, 485 (1989), Phys. Lett. **B237**, 592 (1990).

[108] J. J. Aubert *et al.*, Nucl. Phys. **B259**, 189 (1985), Nucl. Phys. **B293**, 740 (1987).

[109] A. Bodek *et al.*, Phys. Rev. **D21**, 1471 (1979).

[110] L. Whitlow *et al.*, Phys. Lett. **B282**, 475 (1992).

[111] P. Amaudruz *et al.*, Phys. Lett. **B295**, 159 (1992).

[112] L. L. Frankfurt and M. I. Strikman, Phys. Rep. **160**, 235 (1988).

[113] C. Ciofi degli Atti and S. Liuti, Phys. Rev. **C41**, 1100 (1990).

[114] T. V. Kuchto and N. M. Shumeiko, Nucl. Phys. **B219**, 412 (1982).

[115] I. V. Akushevich and N. M. Shumeiko, J. Phys. G: Nucl. Part. Phys **20**, 513 (1994).

[116] N. Dombey, Rev. Mod. Phys. **41**, 236 (1969).

[117] M. J. Alguard *et al.*, Phys. Rev. Lett. **37**, 1258 (1976).

[118] B. Blankleider and R. M. Woloshyn, Phys. Rev. **C29**, 538 (1984).

[119] L. W. Mo and Y. S. Tsai, Rev. Mod. Phys **41**, 205 (1969).

[120] Y. S. Tsai, SLAC-PUB-848, 1971.

[121] E143 Collaboration : K. Abe *et al.*, Phys. Rev. Lett. **74**, 346 (1995).

[122] R. L. Heimann, Nucl. Phys. **B64**, 429 (1973).

[123] J. Ellis and M. Karliner, Phys. Lett. **B213**, 73 (1988).

[124] F. E. Close and R. G. Roberts, Phys. Lett. **B336**, 257 (1994).

[125] E142 Collaboration : P. L. Anthony *et al.*, Phys. Rev. Lett. **71**, 959 (1993).

[126] Spin Muon Collaboration : D. Adams *et al.*, Phys. Lett. **B329**, 399 (1994).

[127] Spin Muon Collaboration : D. Adams *et al.*, CERN-PPE-95-097, June 1995.

[128] E143 Collaboration : K. Abe *et al.*, Phys. Rev. Lett. **74**, 346 (1995).

[129] E143 Collaboration : K. Abe *et al.*, Phys. Rev. Lett. **75**, 25 (1995).

[130] M. Schmelling and R. St. Denis, Phys. Lett. **B329**, 393 (1994); S. Narison, CERN-TH-7188/94, (1994).

[131] J. Ellis and M. Karliner, Phys. Lett. **B341**, 397 (1995).

[132] HERMES Proposal, K. Coulter *et al.*, DESY/PRC 90/1 (1990).

[133] E. W. Hughes *et al.*, SLAC Proposal E154, October 1993.

[134] R. G. Arnold and J. McCarthy *et al.*, SLAC Proposal E155, October 1993.

[135] S. Kuhn *et al.*, CEBAF Proposal (1993).

[136] Z.-E. Meziani *et al.*, CEBAF Proposal (1994).

[137] A. Manohar, An Introduction to Spin Dependent Deep Inelastic Scattering, Lectures given at Lake Louise Winter Institute, Lake Louise, Canada, Feb. 1992.

[138] T. Muta, *Foundations of Quantum Chromodynamics*, World Scientific, New Jersey, 1987.

[139] M. E. Peskin and D. Shroeder, *An Introduction to Quantum Field Theory* (to be published).

[140] E. V. Shuryak and V. I. Vainshtein, Nucl. Phys. **B199**, 451 (1982), Nucl. Phys. **B201**, 141 (1982).